

UNIVERSIDADE DE SÃO PAULO

INSTITUTO DE GEOCIÊNCIAS

Cenozoic exhumation patterns in the eastern Sierra Nevada de Santa Marta, northern
Colombia: A detrital thermochronometry study.

Ana Maria Patiño Acevedo

Dissertação apresentada ao Programa de Pós-
Graduação em Geoquímica e Geotectônica do
Instituto de Geociências da Universidade de São
Paulo como requisito parcial para a obtenção do
título de Mestre em Ciências.

Área de Concentração: Geotectônica

Orientador: Prof. Dr. Mauricio Parra Amezquita

São Paulo

2018

Autorizo a reprodução e divulgação total ou parcial deste trabalho, por qualquer meio convencional ou eletrônico, para fins de estudo e pesquisa, desde que citada a fonte.

Serviço de Biblioteca e Documentação do IGc/USP

Ficha catalográfica gerada automaticamente com dados fornecidos pelo(a) autor(a)
via programa desenvolvido pela Seção Técnica de Informática do ICMC/USP

Bibliotecários responsáveis pela estrutura de catalogação da publicação:
Sonia Regina Yole Guerra - CRB-8/4208 | Anderson de Santana - CRB-8/6658

Patiño Acevedo, Ana María
Cenozoic exhumation patterns in the eastern
Sierra Nevada de Santa Marta, northern Colombia: A
detrital thermochronometry study. / Ana María
Patiño Acevedo; orientador Mauricio Parra
Amezquita. -- São Paulo, 2018.
70+appendix p. p.

Tese (Doutorado - Programa de Pós-Graduação em
Geoquímica e Geotectônica) -- Instituto de
Geociências, Universidade de São Paulo, 2018.

1. Caribbean Plate. 2. Asymmetry exhumation. 3.
Thermokinematic modeling. 4. Cooling age peaks. I.
Parra Amezquita, Mauricio, orient. II. Título.

Acknowledgements

This research was financially supported by the Fundação de Amparo à Pesquisa do Estado de São Paulo-FAPESP, Youth Researcher Grant 2013-03265-5, “Surface processes during active orogenesis-Uplift and erosion of the Sierra Nevada de Santa Marta (Colombia) at multiples time scales”, to M. Parra

I thank to my Professor advisor Mauricio Parra for his continuous support throughout all the development of the research process, for his research incentives, and his contribution to my academic growth.

Sebastian Echeverri is kindly acknowledged for the suggestions, team work and help during sample preparation and discussion of results.

I would like to thank to Santiago León for his assistance and teaching of the laboratory procedures at LabTer.

I kindly appreciate the assistance of Juan Carlos Ramirez during the modeling of data.

I thank to Professor Edward Sobel and Bodo Bookhagen of the University of Potsdam for receiving me in their laboratories and for assistance in the obtaining the helium data. I also want to thank to Professor Agustín Cardona from the Universidad Nacional de Colombia -Medellin, for his suggestions and research incentives and to German Bayona from Corporación Geológica ARES for providing me with samples from the Perijá range that were include in this work. I thank to Red Nacional de Laboratorios de Geociencias (RNLG) at the University of Eafit –Medellín for allowing me to advance in work.

Alexandre Alves and Ana Beatriz de Barros from LabTer-IEE are kindly acknowledged for their assistance during sample preparation. Prof. Andre Sawakuchi kindly offered the facilities of his Luminescence Laboratory (LEGAL) at IGc for final steps of sample preparation. I also thank Thays Desiree for his assistance at LEGAL.

I would like to thank all my collages and friends at IGc and IEE- USP for discussions and support.

Finally, I thank to Fundação CAPES for my scholarship

Abstract

By capturing the regional signature of source rock exhumation, detrital thermochronology of modern sediments has proven successful in revealing the rates and styles of orogenesis. We applied this technique to a small, high relief mountain range in the Caribbean realm in northern Colombia, the Sierra Nevada de Santa Marta, where the patterns of Cenozoic mountain building remain unclear.

The Santa Marta range is the highest coastal mountain on Earth, with summit elevation in excess of 5.8 km, only 40 km inland to the Caribbean Sea. The age and controlling factors for the formation of such abrupt topography remain loosely understood

New AFT and U-Th/He data from river sand samples of eight catchments draining the eastern flank of the range together with a compilation of published ages, allow us to three exhumation pulses spanning the Cenozoic: An early pulse during the Paleocene-Eocene (60-45 Ma) associated to eastward tilting of the formerly continuous Cordillera Central-Santa Marta range triggered by collision of an oceanic crust along western Colombia; a late Oligocene-Miocene (25-20 Ma) episode of tectonic exhumation associated to opening of the Lower Magdalena Valley, and a late pulse at the middle Miocene (16-10Ma) related to eastward migration of the deformation towards the Cesar Rancheria basins and the Perijá Range, and possibly related to contractional reactivation of the Santa Marta-Bucaramanga fault.

Whilst the Paleocene-Eocene exhumation signature is mainly preserved in the northeastern catchments and the middle Miocene in the southwestern ones, the Oligocene- Miocene is ubiquitous to all them. Three-dimensional thermokinematic modeling calibrated, with available bedrock and our new detrital thermochronometric data document asymmetric exhumation in the Cenozoic with integrated rates of 0.26 km/my in the western margin and below 0.14 km /my to the east. Exhumation rates derived from modeling suggest a post-Miocene acceleration of exhumation.

Keywords: Caribbean Plate, asymmetry exhumation, thermokinematic modeling, cooling age peaks.

Resumo

Ao capturar a assinatura regional da exumação de uma área fonte, a termocronologia de sedimentos detriticos modernos tem se provada bem sucedida para revelar as taxas e estilos da orogênese. Nós aplicamos essa técnica a uma serra pequena de alto relevo na região do Caribe, no norte da Colômbia, denominada Sierra Nevada de Santa Marta, onde os padrões da orogênese no Cenozoico permanecem obscuros.

A serra de Santa Marta é a montanha costeira mais alta da Terra, com elevações superiores a 5,8 km, apenas a 40 km do Mar do Caribe. A idade e os fatores controladores da formação dessa topografia abrupta são vagamente compreendidos.

Novos dados de TFA e U-Th/He obtidas de areia fluvial de oito bacias hidrográficas que drenam o flanco oriental da serra, juntamente com uma compilação das idades publicadas, nos permitem determinar três pulsos de exumação abrangendo o Cenozoico: um pulso precoce durante o Paleoceno-Eoceno (60-45 Ma), associado ao cimento para leste da Cordilheira Central-Serra de Santa Marta, área antigamente adjacente, e que foi desencadeada por colisão de crosta oceânica ao longo do oeste da Colômbia; um episódio tardio no Oligoceno-Mioceno (25-20 Ma) de exumação tectônica associada à abertura do Vale do Baixo Magdalena, e um pulso tardio no Mioceno médio (16-10 Ma) relacionado à migração para leste da deformação em direção às bacias de Cesar Rancheria e a Serra de Perijá, e possivelmente relacionadas à reativação contracional da falha de Santa Marta-Bucaramanga.

Enquanto a assinatura de exumação do Paleoceno-Eoceno é preservada principalmente nas bacias hidrográficas ao nordeste e a assinatura do Mioceno médio no sudoeste, o Oligoceno-Mioceno ocorre de forma generalizada. A modelagem termocinemática tridimensional calibrada com os dados *bedrock* disponíveis e os detriticos obtidos no presente estudo documentam exumação assimétrica com taxas integradas para o Cenozoico de até 0.26 km/My na margem ocidental e menores de 0.14 km/My para o leste. As taxas de exumação derivadas apenas da modelagem de dados sugerem uma aceleração de exumação após o Mioceno.

Palavras-chave: Placa do Caribe, exumação assimétrica, modelagem termocinemática, picos de idade de resfriamento.

Table of contents

Abstract

Resumo

1. Introduction.....	2
2. Regional geological setting.....	8
3. Local geological setting	9
4. Previous thermochronological data.....	14
5. Methods	17
5.1 Apatite fission tracks thermochronology	17
5.2 U-Th/He in apatite.....	18
5.3 Analytical techniques	19
6. Results.....	22
6.1 Thermal conditions.....	25
6.2 Detrital thermochronology	27
6.3 Interpretations	34
6.4 Exhumation rates.....	37
7. Termokinematic modeling	39
8. Discussion.....	50
9. Bibliography	55

List of figures

Figure 1 The present-day tectonic configuration of northern South American plate showing actual convergence rates after Trenkamp et al. (2002). SNSM: Sierra Nevada de Santa Marta, SCDB : South Caribbean deformed belt	2
Figure 2. Main features of the tectonic configuration of the northern Andes (Trenkamp et al.,2002).....	4
Figure 3.Geological map of the Santa Marta massif (Gómez et al.,2015). Black lines denote the limits of river catchments sampled for detrital thermochronometry. B. Main morphotectonic features at the northwestern region of Maracaibo block- SNSM: Sierra Nevada de Santa Marta; SP: Serranía de Perijá.. C: Bouguer Gravity anomaly contours (ANH, 2010).	10
Figure 4. Available thermochronological data in the Santa Marta Massif and the western foothills of the Perijá range.	15
Figure 5. Sampled sites. Delimited areas correspond to the studied catchments.	20
Figure 6. Hypsometric curves for each catchments. High lines are showing the second and third quartile of the accumulated curve....	22
Figure 7. Simplified geological maps (Gomez et al., 2015) of each catchment area and pie charts showing relative proportion of each rock type.....	24
Figure 8. Example of the procedure in the calculation of the structural depth.....	26
Figure 9. Kernel Density Estimator diagrams of detrital AFT age distributions. Solid lines denote peaks with populations >10% and dashed lines with populations <10% .The histograms correspond to uncorrected lengths tracks measurements.	29
Figure 10. Kernel Density Estimator diagram of detrital AHe age distributions. Solid lines denote the age of the main peak of the distribution	31
Figure 11. Radial plots for Dpar measurements vs ages.	32
Figure 12. Thermal history model for selected grains of the Guatapurí catchment in which both, ages and track length measurements are available.....	33
Figure 13. Summary of main ages peaks in geographical arrangement. Shaded areas represent exhumation pulses proposed. Only populations made of >10% of the total spectra are presented.....	36
Figure 14. A: Exhumation rates calculated from the youngest representative age peak of detrital samples. Unfilled rectangles correspond to detrital samples of marginal basins (Palomino and Aracataca, Piraquive et al., 2017). B. detail of exhumation rates calculated considering the respective crustal depth of thermochronometers AFT and AHe.	38
Figure 15. A. Model settings. Gray areas represent catchments with detrital thermochronological ages obtained in this study. B. comparison between bedrock ages of the best models for each group and the measured ones (Villagómez et al., 2011b, Cardona et al., 2011b).C. Detail of the AHe ages comparison. D. Detail of the AFT ages comparison.	42
Figure 16. Relation between fault velocity and misfit (evaluated with the log-likelihood, LLH) for different fault geometries. A: Total LLH using both AFT and AHE data. B:LLH using AHe data only. C:LLH using AFT data only.....	44
Figure 17. Comparison of boxplot diagrams corresponding to measured and modeled detrital cooling ages. Bold black lines represent the central tendency and colored boxes the	

interquartile range and thin black lines the 95% confidence interval of each age distribution	48
Figure 18. Exhumation rates derived from data set of the model B, corresponding to the group 2 of models conformed by a set of four vertical faults	49
Figure 19. Oversimplified paleogeography of emerged blocks in the Cenozoic for northern Colombia. (Modified after Escalona and Mann 2012, Ayala et al., (2012))	50

List of tables

Table 1. Estimations of paleo-depths and corresponding maximum temperatures reached by pre-Cretaceous rocks during Aptian time currently cropping out at the summit and outlet of each catchment. See Figure 5 for further explanation.....	27
Table 2. Age peaks derived from age distributions of each sample with their proportions (%)	30
Table 3. Grains of the Guatapurí sample used to model in Hefty. Each grain has both age and uncorrected length measurements	32
Table 4. Integrated maximum exhumation rates based on the youngest age peak identified in different river catchments from the eastern Santa Marta massif and the Perijá range.	37
Table 5. Geometric, thermal and elastic parameters common to all Pecube models.	40
Table 6. Descriptive statistical parameters associated to boxplot diagrams.	45

1. Introduction

The rise of mountains is controlled by the competing relation between constructive processes driven by tectonic forces and destructive processes as exhumation and erosion (Reiners and Brandon, 2006). In active convergent margins, the thermal response of the crust during orogeny studied through thermochronological techniques allow understanding aspects as timing and rates of exhumation that ultimately help infer the tectonic mechanism that controls it.

Andean Orogeny in northern South America has been occurring since the Late Cretaceous by collision and subsequent subduction resulting from the convergence between the Caribbean (Pindell and Barrett, 1990; Kerr et al., 1996), and the South American plates (Vallejo et al., 2006; Weber et al., 2009; Bayona et al., 2011; Cardona et al., 2011a).

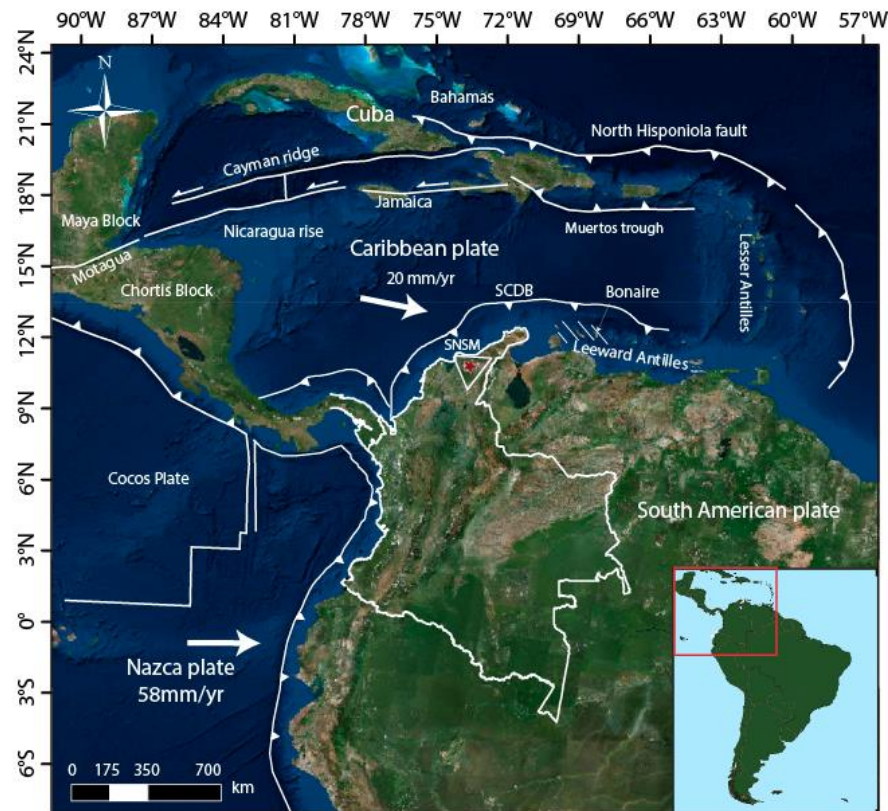


Figure 1 The present-day tectonic configuration of northern South American plate showing actual convergence rates after Trenkamp et al. (2002). SNSM: Sierra Nevada de Santa Marta, SCDB : South Caribbean deformed belt.

The Caribbean Plate is made up of >15 km of oceanic crust (Bowland and Rosencrantz, 1988) and its origin has been proposed as a Galapagos hotspot that sourced an oceanic plateau and gave rise to a Large Igneous Province with its main magmatic pulse at around 90 Ma (Duncan and Hargraves, 1984; Kerr et al., 1996; Mauffret and Leroy, 1997; Sinton et al., 1998; Thompson et al., 2004). This plate drifted eastward until its present position (Figure 1) (Duncan and Hargraves, 1984; Burke, 1988; Villamil and Pindell, 1998; Kennan and Pindell, 2009), promoting a significant strike-slip regime along its northern and southern plate boundaries (Pennington, 1981; Kafka and Weidner, 1981; Rosencrantz et al., 1988). The northern margin is defined by a left lateral transform boundary along western Guatemala to Lesser Antilles subduction zone. To the western segment, in the Cayman trough more than 1100km of left lateral motion since the Eocene has been documented (Rosencrantz et al., 1988). The southern margin along northwestern South America is defined by a widespread region of oblique and right-lateral deformation (Kafka and Weidner, 1981; Pennington, 1981; Audemard M, 2001). A dextral transpressional regime supports a disassembly of continental fragments subjected to processes of translation and rotation (Montes, et al., 2005a; Montes et al., 2010; Bayona et al., 2010).

The eastward advance of the Caribbean Plate has caused the accretion of Late Cretaceous igneous complexes along the northwestern margin of South America. These units are found juxtaposed to the continental basement through a series of regional fault systems (Kerr and Tarney, 2005; Spikings et al., 2005; Vallejo et al., 2006; Villagómez, et al., 2011a; Weber et al., 2009). Fragments of an intraoceanic arc built over the oceanic plateau are included in the accreted blocks (Burke, 1988; Kerr and Tarney, 2005; Pindell et al., 2005). However, widespread geochronological evidence supports multiple arc systems formed along the eastern margin of the Caribbean Plate (Weber et al., 2009; Bustamante et al., 2011; Wright and Wyld, 2011; Cardona et al., 2012).

The record of oceanic arc-continent collision in the north of Colombia at ca. 70Ma (Cardona et al., 2011a and references therein) include synorogenic sedimentation enhanced by eastward tilting of the continental margin. The provenance signals are interpreted as input of both, Caribbean related and continental uplift blocks that came into being source areas of surrounding foreland basins (Cardona, et al., 2011a; Bayona et al., 2011; Ayala et al., 2012). In addition, a metamorphic event underwent by arc-related lithologies constrained to 65 Ma and a contemporaneous magmatic

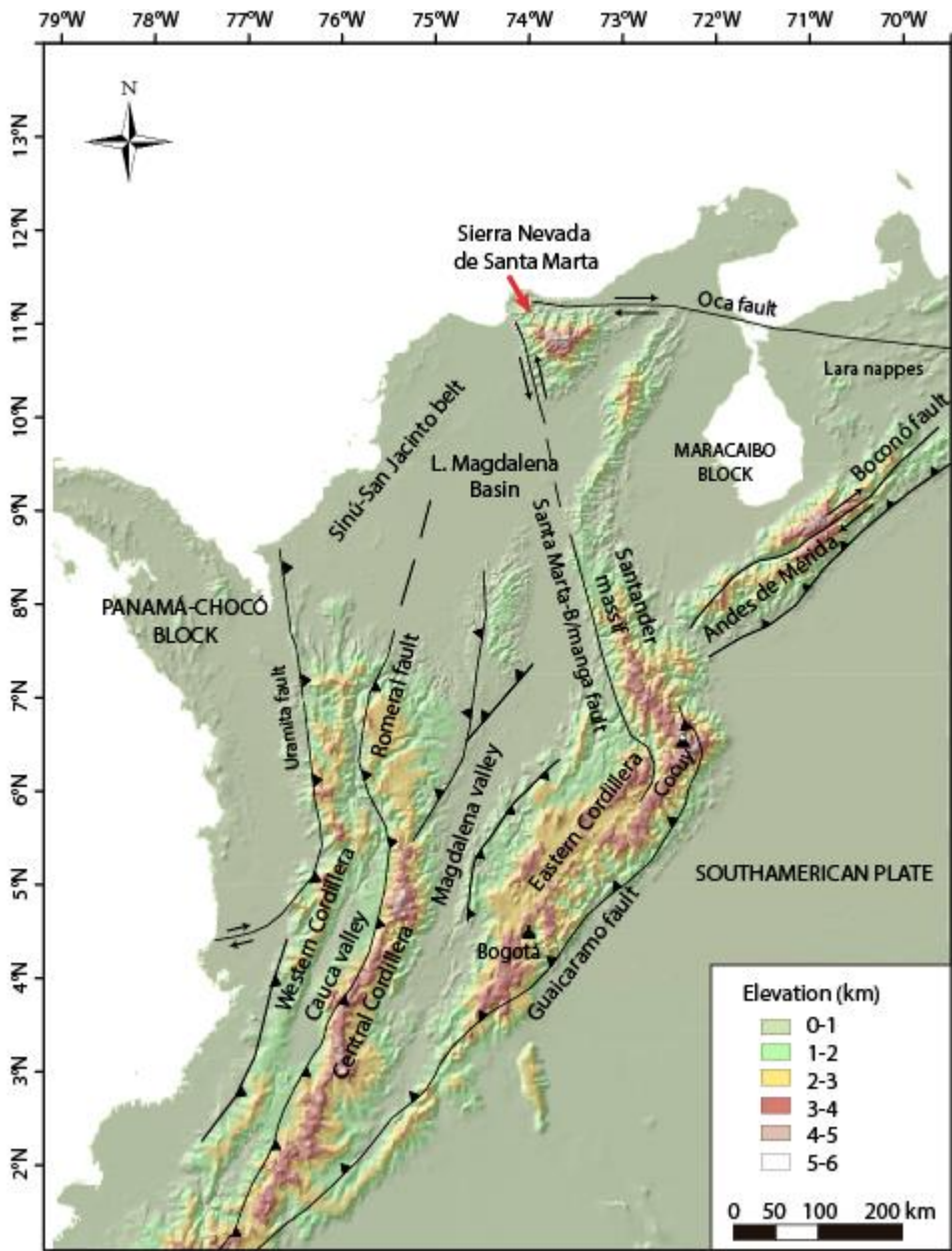


Figure 2. Main features of the tectonic configuration of the northern Andes (Trenkamp et al., 2002).

peak are associated to this collisional episode (Bustamante et al., 2009; Cardona, et al., 2010a; Weber et al., 2010; Bayona et al., 2012). Subsequent magmatic activity in the continental margin at ca. 54-60 Ma has been related to the subduction of the Caribbean Plate beneath South America (Duque, 2009; Cardona et al., 2011a; Bayona et al., 2012; Salazar et al., 2016).

Evidence for the onset of orogeny includes shortening and early uplift of the Central Cordillera and the development of a foreland basin system, involving the present day Magdalena Valley and the Eastern Cordillera regions (Gómez et al., 2003), documented through rapid cooling episodes in the Central Cordillera (Villagómez and Spikings, 2013; Caballero et al., 2013) and through provenance signals that point out to source of sediment from that range since Maastrichtian (Gómez et al., 2005; Nie et al., 2012; Silva et al., 2013; Horton et al., 2015). Tectonic load exerted by the Central Cordillera influenced the foreland basin modifying the locus of depozones in the sedimentary system. Thermochronological and sedimentary provenance evidence support an eastward migration of deformation during Eocene-early Oligocene whereby contractional deformation was accommodated along inherited Mesozoic extensional structures (Parra et al., 2009; Mora et al., 2010; Parra et al., 2012; Saylor et al., 2012). Such basement anisotropies constitute the main structures through which the Eastern Cordillera uplifted as an inverted bivergent orogen (Mora et al., 2006).

The advance of deformation in the northern Andes has been explained as depicting a non-systematic pattern toward the eastern foreland. This is reflected in a pulse of exhumation at 60-50 Ma found in along the boundary between the Magdalena Valley and the Eastern Cordillera, where Paleogene deposition took place in a wedge top depozone associated to doubly vergent reverse faults (Parra et al., 2012).

The physiography of the Andes in northern of Colombia is characterized by a break in continuity north of $\sim 7.5^{\circ}$ N and the presence of isolated fault-bounded blocks, including the prominent Sierra Nevada de Santa Marta. This block is located in the northwestern corner of the major Maracaibo block, which itself is limited to the southeast by the right lateral Boconó fault system, to the west by the left lateral Santa Marta Bucaramanga fault system , and to the north by the right lateral Oca-Ancón fault system (Figure 2) (Taboada and Rivera, 2000; Audemard et al., 2005). The Sierra Nevada de Santa Marta has been interpreted as a crustal block that was attached to the Central Cordillera until pre-late Eocene times (Montes et al., 2010) . A connection between them is supported by geochronologic data that allows establishing a correlation among Permo-Triassic rocks found in the basement of the Lower Magdalena basin (Montes et al., 2010; Mora-Bohórquez et al., 2017) and the Santa Marta massif (Cardona et al., 2010b), with the Permo-Triassic basement domain of the Central Cordillera (Vinasco et al., 2006, Villagomez et al., 2011a). Duque-Caro

(1979) and Montes et al. (2010) suggest that this former Permo-Triassic belt was later dislocated to its current northern position by clock-wise rotation.

The disruption of the Santa Marta massif and Central Cordillera has also been explained as a consequence of ~110 km Neogene left-lateral displacement along the Santa Marta – Bucaramanga fault (Campbell, 1965). Recent estimation of low values (3-7Km) of regional shortening in the adjacent Cesar –Rancheria basin based on structural restorations is in agreement with an offset of the Santa Marta massif due activity in the Santa Marta Bucaramanga fault (Sanchez and Mann, 2015). Unlike, higher values (>50Km) are required in the clockwise rotational model that is established considering paleomagnetic data (Montes et al., 2010).

Displacement of crustal blocks results from the oblique convergence and right lateral shearing of the Caribbean and South American plates (Kennan and Pindell, 2009). For instance, right lateral displacement of at least 200 km is proposed for the Island of Bonaire, Leeward Antilles (Figure 1), located to the northeast in the Caribbean plate realm (Zapata et al., 2014). There, Jurassic, Permo-Triassic and Greenville detrital zircon U-Pb age populations in the middle to upper Eocene strata are interpreted as derived from South American massifs and allowed establishing a connection of the island with the northern South American continental margin until the late Eocene (Zapata et al., 2014).

Gravity studies (Case and MacDonald, 1973; Ceron-Abril, 2008; Sanchez and Mann, 2015; Bernal-Olaza et al., 2015; Mora-Bohórquez et al.,2017) detect a positive Bouguer anomaly of above +175 mgal beneath the Sierra Nevada de Santa Marta (Figure 2B). This major anomaly has been associated either with an oceanic crust underthrusting the continent (Ceron-Abril, 2008), or with removal of lower crust leading to recent uplift through northwest vergent overthrusting (Case and MacDonald, 1973).

Such positive anomaly incites a particular interest for the understanding of uplift processes involving the Sierra Nevada de Santa Marta, in the sense of a recent pulse of surface uplift. Other regions with lower but significant topographic elevations show, as is expected, negative gravity anomalies in response to a mass deficit related to the presence of a crustal root reflecting isostatic compensation. For instance, the Bogota high plain (2600 m) , the Cocuy massif (4800) and the

Merida Andes in Venezuela (4200m), correspond to values between -158 to -80mGal (Ceron-Abril, 2008)

Available low thermochronological data from the Santa Marta massif have suggested an asymmetric pattern of uplift (Villagómez et al., 2011b; Piraquive et al., 2017) with an early pulse of exhumation at 60-58 Ma preserved only in the northeastern region of the range and a younger episode of faster exhumation, between 35 and 15 Ma, preserved in the northwestern corner (Villagómez et al., 2011b; Cardona et al., 2011b). Despite contributions of these works, it remains unclear why cooling ages are not so young as it would be expected in a humid region with abrupt topography (60-16 Ma for AFT, 24.6-5.5 Ma for AHe and 26.8 - 18.7 for ZFT ; Villagómez et al., 2011b; Cardona et al., 2011b). For instance, high topography in the Eastern Himalayan syntaxis occurs in an area with high Pliocene exhumation rates > 5km/my, in response to a high erosional regime (Lang et al., 2016). Possibly, younger ages in the Santa Marta Massif could remain undiscovered either by insufficient sampling representation or by a still unexposed fossil partial annealing/retention zone, as it is suggested by Villagómez et al. (2011b)

The goal of this study is to document spatial and temporal variations in exhumation rates in the southeastern flank of the Santa Marta Massif and to establish correlations with tectonic episodes involving the Perijá range and the Cesar Rancheria Basin. We employed detrital thermochronology, including apatite fission track (AFT) and (U-Th)/He in apatite (AHe), in modern river sand, in order to take advantage of the wider spectrum of elevations sampled by catchment erosion, and thus, to identify cooling age populations that can be associated to recent exhumation and that allow identifying the controlling factors of such exhumation.

2. Regional geological setting

According to GPS velocity vectors, the present-day convergence rates of the Nazca and Caribbean Plates against a fixed South American plate are 58 ± 2 mm/yr in an almost E direction, and 20 mm/yr in an ESE direction, respectively (Figure 1; Trenkamp et al., 2002). These studies also support an NE-directed tectonic escape of the north Andes at a rate of 6 mm/yr (Freymueller et al., 1993; Trenkamp et al., 2002).

Recent plate kinematics in northwestern of South America is dominated by the interaction of the Panamá-Chocó block and the Nazca and Caribbean Plates (Figure 1) .The Panamá block is considered as an indentor block undergoing collision with the continental margin of northwestern Colombia at rate of 30 mm/yr (Freymueller et al., 1993; Kellogg et al., 1995; Trenkamp et al., 2002). The subduction of the Nazca Plate beneath the South American Plate at 5.5° N Lat occurs at a dip angle of 35° (Pennington, 1981), bearing an active volcanic arc along the present-day Central Cordillera. Unlike these southern regions of the northern Andes, subduction of Caribbean Plate has a less clear expression due essentially to the lack of well-defined seismic zones and regional earthquakes (Van der Hilst and Mann, 1994; Bernal-Olaza et al., 2015, Mora-Bohórquez et al., 2017).

Active volcanism related to the Nazca Plate subduction is present until 5.5° N; farther to the north, the record is scarce and has been explained as result of the shallow subduction of the Caribbean Plate beneath northwestern Colombia, for instance, (Lara et al., 2013) documented volcanism at 13 Ma in the Sinu belt, and Mantilla-Pimiento et al., (2009) in the Santander Massif at 10Ma. However, Wagner et al. (2017) based on a wide compilation of volcanic ages that postdate the collision of the Panamá-Chocó block (14 Ma, Montes et al., 2015), found a continuous volcanic arc as far to the north as 7° N. Such volcanic activity involving subduction of the Nazca Plate gradually extinguished in response to the development of flat slab subduction between 7 and 2 Ma. Finally, the slab steepened again south of 5.5° N and caused the establishment of the actual volcanic arc.

Geophysical surveys in northern Colombia have been used to suggest a low angle subduction ($\sim 10^{\circ}$, Bernal-Olaza et al., 2015) of the Caribbean Plate beneath South America, which steepens

to $\sim 35^\circ$ at ~ 450 km in a southeast direction from the frontal thrust. Furthermore, according to gravity data, the thickness of the Caribbean slab change from 13-16 km in an offshore region to 7 km in the steeper-dipping part (Bernal-Olaza et al., 2015; Sanchez and Mann, 2015).

3. Local geological setting

The Sierra Nevada de Santa Marta, is a fault-bounded basement uplift with prominent topography, up to 5.7 km at the summits, and a relatively small area of ~ 15.600 km², located above the subducted Caribbean Plate in northern Colombia (Bernal-Olaza et al., 2015). Surrounding the range, to the north of the right-lateral Oca fault lies the Baja Guajira basin and to the southwest of the left lateral Santa Marta Bucaramanga fault the Lower Magdalena basin (Figure 2).

A large vertical component along both faults is inferred by the correspondence between the basement exposure in the Sierra Nevada de Santa Marta and the substrate of surrounding basins (Montes et al., 2010), covered by 8 km of Cenozoic strata in Lower Magdalena (Duque-Caro, 1979) and by 3km of Meso-Cenozoic strata in Baja Guajira (Rincón et al., 2007).

On the contrary, the range's southeastern boundary against the Cesar-Rancheria basin is in structural continuity with the flank of the range in the form of a monocline dipping to southeastern (Tschantz et la., 1969), with a Aptian to recent sedimentary cover of >2 km (Bayona et al., 2007; Ayala-Calvo et al., 2009).

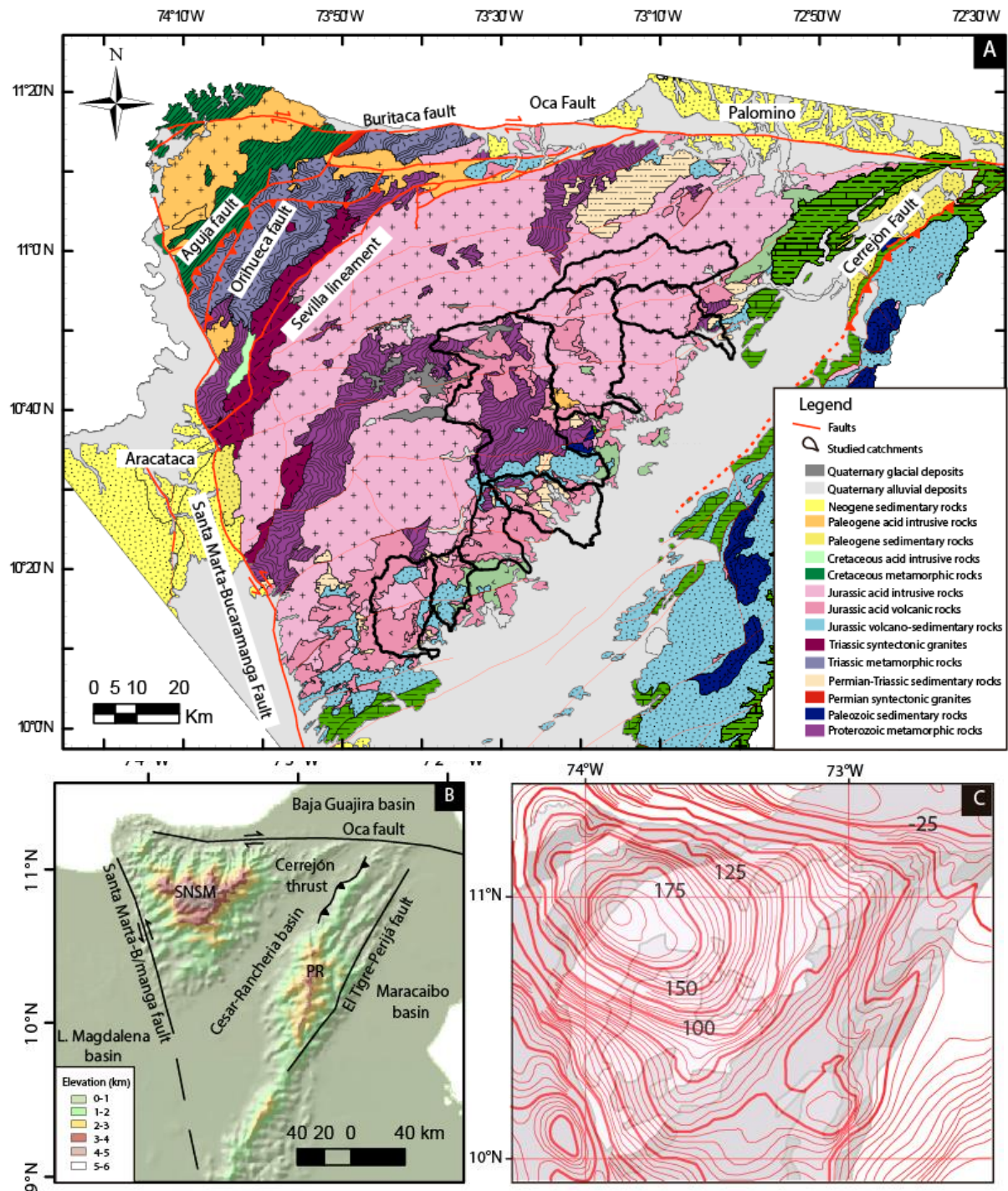


Figure 3. Geological map of the Santa Marta massif (Gómez et al., 2015). Black lines denote the limits of river catchments sampled for detrital thermochronometry. B. Main morphotectonic features at the northwestern region of Maracaibo block- SNSM: Sierra Nevada de Santa Marta; SP: Serranía de Perijá.. C: Bouguer Gravity anomaly contours (ANH, 2010).

Three major provinces with particular metamorphic basement constitute the Santa Marta massif: (1) the northwest Upper Cretaceous –Paleocene belt of low to middle grade metamorphic rocks; (2) a central province with Paleozoic middle grade metamorphic rocks (3) and a southeastern province conformed by Proterozoic high-grade metamorphic rocks (Tschanz et al., 1974).

The northwest belt is composed mainly by pelitic and psammitic schist and metabasites of greenschist to amphibolite facies formed during late Cretaceous-Paleocene (Tschanz et al., 1974; Cardona et al., 2010a; Zuluaga and Stowell, 2012), and it is intruded by Paleocene –Eocene rocks with tonalite, quartzdiorite and granodiorite compositions (Duque 2010; Cardona et al., 2011a, Salazar et al., 2016). The central Paleozoic belt, bounded to the east by the Sevilla lineament and to the west by the Aguja fault, comprises mostly amphibolites, paragneisses and mica schists formed in amphibolite facies (Tschanz et al., 1974; Cardona et al., 2006, Cardona et al., 2010b). This region further to presents Paleocene-Eocene intrusions include Permo-Triassic syntectonic intrusive rocks (Cardona et al., 2010b). To the southeast, the oldest belt correspond to a Meso-Proterozoic metamorphic basement composed of pelitic, quartz-feldspathic, and mafic gneisses of amphibolite-granulite facies rocks (Tschanz et al., 1974, Cordani et al., 2005; Cardona-Molina et al., 2006).. This province presents undeformed Jurassic intrusive rocks including granodiorites, quartzmonzonites granites and Jurassic-early Cretaceous volcanic felsic rocks (Tschanz et al., 1974). Minor occurrences of Paleozoic and Mesozoic sedimentary and volcano-sedimentary rocks are restricted to this region (Tschanz et al., 1974).

Whereas lithologies of Santa Marta massif are mainly igneous and metamorphic, the Perijá range located to the east and separating the intermontane Cesar-Rancheria basin from the Maracaibo basin to the east (Figure 3B) is constituted mainly by sedimentary sequences with minor exposures of a basement of Precambrian metamorphic rocks (Miller, 1962; Kellogg, 1984).

Stratigraphic correlations of the Perijá range include a Precambrian metamorphic basement overlain by Cambrian-Ordovician, Devonian-Pennsylvanian, Permian and Mesozoic sedimentary sequences with successive unconformable contacts (Tschanz et al., 1974; Miller, 1962). Pre-Cretaceous sequences, lower Cretaceous limestones and an upper interval of Upper Cretaceous and Cenozoic coarse-grained clastic rocks, reach thicknesses about 1000m, 1000m and 5500m, respectively (Duerto et al., 2006). The main tectonic pre-Cenozoic events involving the Perijá range

were a Silurian-Early Devonian orogeny causing weak metamorphism in Cambrian-Ordovician sedimentary rocks, and Jurassic-early Cretaceous rifting and volcanism (Kellogg, 1984).

The Cerrejón southeast dipping thrust marks the eastward boundary of the monocline that defines the structural continuity of the Santa Marta massif and Cesar-Rancheria basin, and the western boundary of the Perijá range (Kellogg, 1984). Its detachment level, as common to several thrusts in the Cesar-Rancheria basin, occurs along incompetent Paleogene strata, (Montes et al., 2010). The Tigre fault along the eastern margin of the Perijá Range has been interpreted either as dextral strike-slip fault (Duerto et al., 2006) or as a north-verging thrust (Kellogg, 1984).

In the Eocene, the Perijá range became a barrier separating the Rancheria basin from the northwestern Maracaibo basin via reactivation of high angle former Mesozoic structures (Ayala et al., 2012). Angular unconformities at 53Ma, 45Ma, and 25Ma along the Perijá range's eastern flank have been interpreted as the consequence of contractional deformation and concurrent uplift of the range. (Kellogg, 1984).

Sedimentation in the Cesar-Rancheria basin since Aptian took place in carbonate platforms above a substratum made of Triassic-Jurassic volcano-clastic and intrusive basement rocks in a passive margin setting controlled by transgressive events (Tschanz et al., 1974; Caceres et al., 1980). Two episodes of eustatic sea-level highs have been recognized, for the Early Aptian and the Cenomanian-Turonian (Martinez and Hernandez, 1992). Depositional environments alternate between inner, middle and outer shelf (Caceres et al., 1980). On the other hand, Cenozoic sedimentation took place simultaneously with contractional tectonic deformation, conforming a synorogenic record (Bayona et al., 2011; Ayala et al., 2012; Cardona et al., 2011a).

Late Paleocene eastward tilting of the crust along a horizontal axis, as proposed by (Montes et al., 2005b), explain coeval uplift of the Sierra Nevada de Santa Marta to the west and concomitant creation of accommodation space to the east, allowing deposition in the Cesar-Rancheria Basin, resulting in an increase of the tectonic subsidence rates, from 48 m/my in early Paleocene to 87m/my in the Late Paleocene.

Provenance signatures such as sandstone composition and detrital zircon U-Pb age document changes in sources of sediments deposited during the Paleogene. Lower to middle Paleocene strata are siliciclastic to the south and carbonate to the north and exhibit predominance of quartz and

sedimentary lithic fragments with a predominance of U-Pb age populations of 0.9 to 2.5 Ga to the north and 1.5 to 2.5 Ga to the south. Such a pattern has been interpreted as the result of the reworking of a Cretaceous covert from sediment sources located to the south , transported along a regional drainage (Ayala et al., 2012).

Coal-rich upper Paleocene strata present an increase of lithic and feldspar components. Their detrital zircon age populations reveal the contribution of Jurassic and Permo-Triassic rocks, and rocks with ages ranging from 65 to 360 Ma, which was interpreted as deposited by a modified drainage system fed by small transversal rivers (Bayona et al., 2011; Ayala et al., 2012; Cardona et al., 2011a). These provenance signals, the preservation of unstable sandstone components probably supplied by a nearby source (Bayona et al., 2007) , and high subsidence rates (Bayona et al., 2011), have been used as arguments to propose the Sierra Nevada de Santa Marta - Central Cordillera as source areas (Bayona et al., 2007, 2011; Ayala-Calvo et al., 2009; Ayala et al., 2012; Cardona et al., 2011a).

Overlying the Upper Paleocene sequence, commonly disconformably, (Caceres et al., 1980; Montes et al., 2010; Jaramillo et al., 2010; Bayona et al., 2011), Lower Eocene strata were deposited mainly in fluvial environments. They are characterized by significant changes in composition such as an increase of potassic feldspar, quartz, chert and sedimentary lithic fragments, suggesting the Perijá range as a new source of sediments (Bayona et al., 2011, 2007). Zircon age populations are similar to those of upper Paleocene strata, but, in addition, a new age population of ~50-55 Ma (Bayona et al., 2011; Ayala-Calvo et al., 2009; Ayala et al., 2012; Cardona., 2011a) occurs. This Eocene detrital zircon ages have been interpreted as the result of surface exposure of the Eocene granitoids that intrude the northwestern corner of the Santa Marta Massif (Bayona et al., 2011;Cardona et al., 2011a; Ayala et al., 2012). However, such interpretation is in conflict with geobarometric data of this pluton that reveal a paleodepth of around 15-19 km (4.9—6.4 kbar) during pluton emplacement at 58-60Ma (Cardona et al., 2011b). Alternatively, interstratification of a felsic tuff (56 ± 0.03 Ma) reported in lower Eocene strata of northwestern Maracaibo basin (Jaramillo et al., 2010) support coeval volcanism in the area that could source the Eocene zircons.

Post-Eocene sedimentation has been recognized mainly in the subsurface and consists, in the Rancheria sub-basin, to the north, of an Upper Eocene- Oligocene sequence deposited in a tide-influenced platform and unconformably overlain by Upper Miocene fluvial deposits (Caceres et

al., 1980). In the Cesar sub-basin, to the south a continental sequences constituted by sandstones, conglomerates and mudstones likely of a Middle Miocene-Pliocene age have been documented (Geopetrocol, 1998). These sedimentary sequences are characterized by major unconformity contacts at the base and the top.

Sub-surface structural mapping in the Cesar-Rancheria basin reveal the presence of a buried fold and thrust belt made of east-dipping reverse faults, the main of which reaches the surface, contributing with the uplift of the Perijá Range (Sanchez and Mann, 2015). Cross-cutting relationships beneath the Miocene-Pliocene unconformity and the preservation of Paleogene units restricted to the easternmost thrust sheets suggest the earlier activity of western faults within the fold-and-thrust belt and supports and an eastward advance of the deformational front (Sanchez and Mann, 2015).

Marginal basins located along the foothills of the Santa Marta massif, the Palomino basin to north and the Ariguaní Depression to west, are constituted by similar Neogene sedimentary sequences (Tschanz et al., 1969; Hernandez et al., 2003). The Ariguaní Depression comprise a basal sequence of fossiliferous siltstone alternating with marls, sandstone and conglomerates of transitional to shallow marine environments; overlaid by conglomeratic strata of transitional-marine to alluvial environments (Echeverri et al., 2017). To the north, fan delta conglomerates are overlaid by sandstones alternating with siltstones of fluvial and fan delta environments (Echeverri, et al., 2017). Unlike the youngest Paleocene-Eocene detrital zircon U-Pb age populations found in the Paleogene sedimentary units in the Cesar-Rancheria basin, as previously described, the Neogene infill of the Ariguani and Palomino basins do not contain age populations younger than 116 Ma (Piraquive et al., 2017).

4. Previous thermochronological data.

Exhumation events during the Cenozoic in the Sierra Nevada de Santa Marta have been recently identified through low-temperature thermochronology suggesting : (1) faster exhumation rates toward northwestern corner (Villagomez et al., 2011b), (2) events of rapid exhumation at 24 and 15 Ma at the northwest tip of the range (Cardona et al., 2011b), and (3) asymmetrical exhumation for the to the northern and western sides (Parra et al., 2016, Parra et al 2017, Piraquive et al., 2017).

Published bed rock thermochronometric data by Villagómez et al.(2011b) (Figure 4), include 22 apatite fission track (AFT) largely collected along two elevation profiles, one in the Sierra Nevada Province at the range's western margin (Fundación profile; 10 samples) and one at the Santa Marta Province in its northwestern corner (Kennedy Profile; 11 samples). AFT ages range from 23.3 ± 4.4 to 53.8 ± 8.2 Ma in the Fundación profile, and from 16.0 ± 2.5 to 41.0 ± 9.6 Ma in the Kennedy Profile (Figure 3). In both cases, exist a relative good age-elevation correlation.

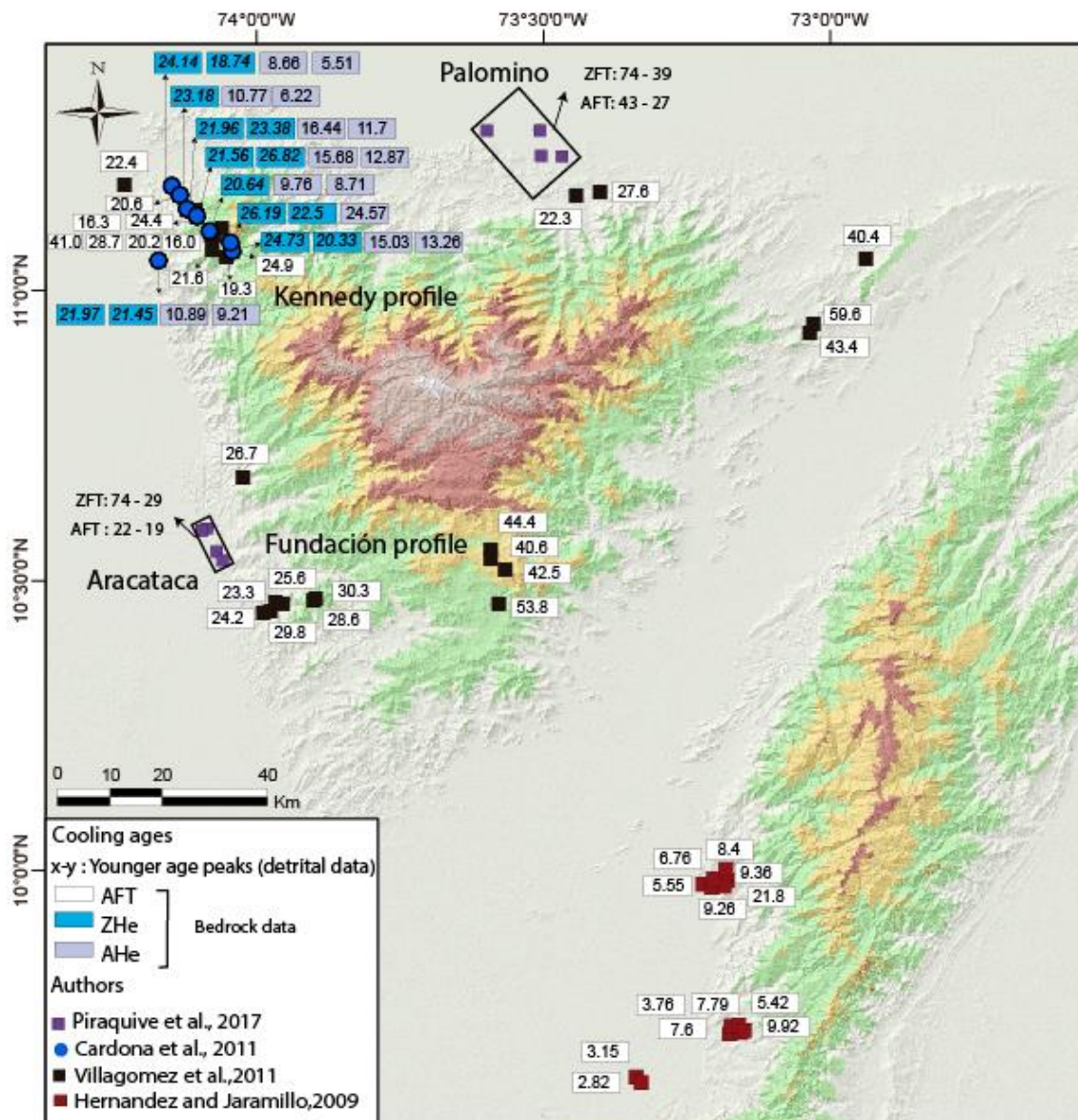


Figure 4. Available thermochronological data in the Santa Marta Massif and the western foothills of the Perijá range.

Additional sampled sites are included: Paleocene granitoids to the northern margin (2 samples; 22.3 ± 3.1 Ma and 27.6 ± 4.6 Ma) and Jurassic granitoids and felsic volcanic rocks at its northeastern margin (3 samples; 40.4 ± 5.7 Ma to 59.6 ± 10.4 Ma).

In addition, 15 apatite and 14 zircon (U-Th)/He (Ahe and Zhe, respectively) single grains have been obtained from 8 samples along the Kennedy profile, with good within-sample reproducibility and a fair to good age elevation relationship (Cardona et al., 2011b) (Figure 3). Weighted average AHe ages range from 7.6 ± 0.8 to 24.5 ± 7.0 Ma and ZHe ages from 20.6 ± 0.6 to 24.3 ± 0.5 Ma.

Recently detrital AFT and ZFT data were published for Cenozoic strata from the Palomino margin to the north, and Aracataca margin to the west, assigned to Oligocene-early Miocene based on regional stratigraphic correlations (Piraquive et al., 2017). In the north, AFT data collected in one sample from the middle to upper Miocene rocks (15 ± 5 Ma) reveal two AFT age populations of ~ 26 Ma and ~ 53 Ma, implying lag-times of $\sim 15 \pm 5$ Ma and 40 ± 6 Ma. ZFT detrital ages in 5 samples from the same strata collected along two stratigraphic sections yield age populations of 33-41 Ma, ~ 55 Ma, 74-90 Ma, 108-132 Ma, and 156-170 Ma and 254 Ma. From them, we interpreted that only the two youngest population may reflect reset ages related to the Cenozoic Andean cycle of exhumation. In the sedimentary sequence of the western margin (Aracataca), recently dated as early Miocene (Echeverri et al., 2016), were dated 2 AFT samples that yielded age peaks of 19-22 Ma, 30 Ma and 42-60 Ma; and 3 ZFT samples with age peaks of 29 Ma, 48-52-74 Ma, 104-108 Ma and 167 Ma. The youngest cooling ages imply a shorter AFT lag-time of ~ 4 -10 Ma.

Farther to the east, in the western foothills of the Perijá range, AFT cooling ages of Jurassic-Cretaceous rocks completely annealed range between ~ 3 -10 Ma (Hernandez and Jaramillo et al., 2009).

5. Methods

5.1 Apatite fission tracks thermochronology

Apatite is a U-bearing common accessory mineral in geological materials and therefore has been widely used as U-Th/He (Farley, 2000) and fission-tracks (Laslett et al., 1987) dating targets. These low-temperature thermochronometers are useful to study the thermal history of upper portions of the crust that result from the exhumation of rocks toward the earth surface, a process promoted either by erosion (climatically or tectonically induced) or by normal faulting (England and Molnar, 1990; Stockli, 2005)

The fission track method exploits the crystalline damage generated by natural fission of the ^{238}U in U-rich minerals. Such damage, called a fission track, is produced by spontaneous nuclear fission of the ^{238}U nuclei into two particles ensuing an energetic displacement in opposite directions that is recorded into the crystal lattice. In this context, ^{238}U constitute the radioactive parental element of the radio-chronometric system and the spontaneous fission tracks constitute its radiogenic daughter product (Price and Walker, 1963; Fleischer and Price, 1964; Fleischer et al., 1975).

Subsequently to the formation of spontaneous tracks, exposure of rocks to high temperatures reduces progressively the track length from the initial $\sim 16\ \mu\text{m}$ for apatites, in a process called annealing. This process is mainly controlled by solid state diffusion and lead to the time and temperature dependent repairing of vacancies in the mineral crystalline lattice. Field observations of naturally annealed apatites from well samples (Gleadow and Duddy, 1981) allowed defining an interval of temperature between $\sim 120\text{--}60^\circ\text{C}$ (Green et al., 1986) where the process of annealing mainly occurs, and which defined the so called apatite fission tracks Partial Annealing Zone (PAZ)

In addition to observations of naturally annealed apatites, laboratory track-annealing experiments under controlled time and temperature conditions (Green et al., 1986, Ketcham et al., 1999, Ketcham et al., 2007), have provided insights into the kinetics of fission track annealing and allow using track-length data to inverse model thermal histories

Besides temperature and time of heating/cooling (heating/cooling rate) (Reiners and Brandon, 2006; Green et al., 1989), empiric observations demonstrate that track annealing is also correlated

with apatite chemical composition and grain solubility. In particular, chlorine content and the solubility of the crystal in the etching solution, expressed as the diameter of the polygon formed by intersection of the fission track and the polished surface of the crystal, called Dpar (Donelick , 1993; Ketcham et al.,1999), have been identified as kinetic parameters and have been incorporated into the kinetic models (e.g., Ketcham et al., 2007). Apatites with larger Dpar and higher Cl content are in general more resistant to the annealing process (Donelick et al., 2005).

As is the case for all radiochronometric systems, fission-track analyses require the quantification of the parent (^{238}U) and daughter (fission-tracks) products. Determination of the relative uranium concentration in apatite grains can be achieved either inducing fission of the ^{235}U by thermal neutron activation (Tagami and O'Sullivan, 2005), or employing laser ablation-Inductively plasma mass spectrometry measurements (Hasebe et al., 2004, Donelick et al., 2005). Fission-track quantification requires exposure of fission-tracks in polished surfaces of apatite grains and a subsequent acid etching of the surface in order to reveal the tracks. Track density estimation is conducted in an optical microscope, usually at 1250X magnification.

For this study, we used the external detector method (EDM, Gleadow, 1981), which required for each sample an assembly of a mount of polished and etched grains coated by a U-free muscovite sheet. This assembly is exposed to a flux of thermal neutrons in controlled conditions to induce fission of the isotope ^{235}U , producing tracks that will be recorded in the mica. Both spontaneous and induced fission track densities are obtained by counting in an optical microscope (Fleischer et al., 1975). The initial content of the parent isotope ^{238}U is calculated employing the constant ratio between $^{238}\text{U}/^{235}\text{U}$ and together with the spontaneous fission tracks constitute the isotopic ratio used to obtain a cooling age.

5.2 U-Th/He in apatite

The U-Th/He method is based on the radioactive decay chain of the isotopes ^{235}U , ^{238}U , ^{232}Th and ^{147}Sm by α -emission, that consist in the ejection from the nucleus of a pair of protons and neutrons that conform a helium nucleus. The accumulation of α -particles occurs in apatite in trace quantities high enough to be reliably measured with modern mass spectroscopy, which enables its use as a low-temperature thermochronometer (Zeitler et al., 1987). For this system, the favorable thermal

conditions of helium accumulation correspond to temperatures below ~40 – 70°C (Farley, 2002; Wolf et al., 1996). Such range of maximum temperatures has been called the Partial Retention Zone. Results of diffusion experiments in heavily radiation damaged apatites, such as those with very large U-content or that have accumulated lot of damage due to long residence at low temperatures, have revealed a higher temperature, in excess of 120°C, for helium retention. (Shuster et al., 2006; Flowers et al., 2009, Gautheron et al., 2009).

Alpha particles (i.e., He nuclei) are ejected from the nucleus of the parental element at a distance of ~20 µm and therefore can be ejected out from the crystal from parental nuclei located in the outer ~20 µm of the apatite crystal. Therefore, it is necessary to apply the alpha-ejection correction, called the Ft factor (Farley, 2002), which refers to the proportion of the crystal which retains He. This correction assumes a negligible external implantation of alpha particles and a uniform distribution of U-Th throughout the grain.

5.3 Analytical techniques

This study is based on the analysis of modern sediment samples collected in sand bars of rivers that drain the eastern side of the Sierra Nevada de Santa Marta. Fine-to-medium grained sand samples were collected in sand bars from the lower reaches of the Rancheria, Cesar, Badillo, Guatapurí, Callao, Mariangola and Diluvio rivers (Figure 5). The target mineral apatite were obtained by sieving, magnetic separation and heavy liquid standard techniques.

For fission tracks analysis, apatites were mounted in epoxy resin and then polished in order to obtain smooth surfaces. In order to reveal spontaneous tracks, apatite grains were etched with 5.5 mol. HNO₃ at 21°C during 20 s. Each sample mount, as well as dosimeter CN1 and CN-5 glasses used to monitor neutron flux, were covered with mica sheets. Three of the samples were irradiated in the Oregon State University research reactor and the rest of them in the Nuclear and Energy Research Institute (IPEN) of the University of São Paulo exposing samples to a neutron fluence of 3E15 n/cm². Following sample irradiation, induced tracks were revealed in micas through etching with 40% HF at 21°C during 45 min. For each sample, additional aliquots of apatites were mounted and irradiated with ²⁵²Cf at the Department of Geosciences of the University of Texas at Austin in

order to increase the chance to find horizontally confined tracks for length measurements (Donelick and Miller, 1991).

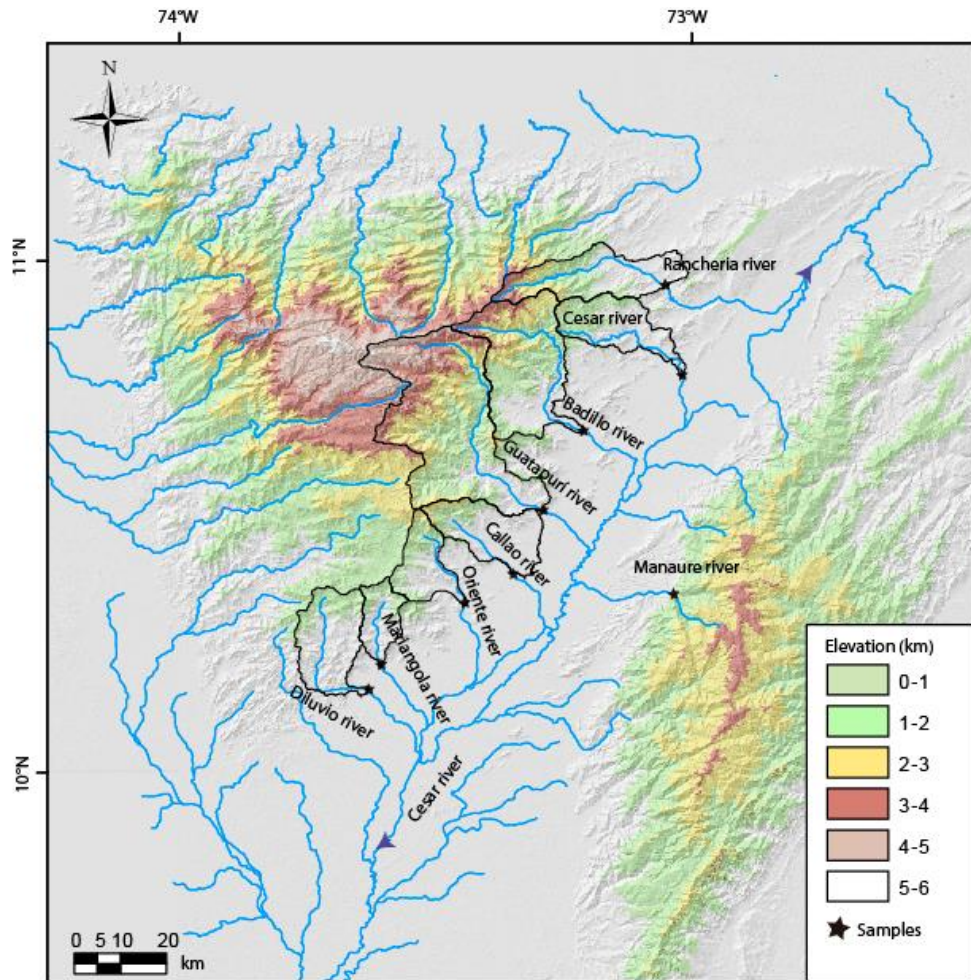


Figure 5. Sampled sites. Delimited areas correspond to the studied catchments.

All samples were analyzed in an Olympus BX51 microscope in the Low-Temperature Thermochronometry Laboratory (LabTer) at the IEE-USP employing a 1250x magnification and dry objective, and with an attached electronic stage, a digitizer tablet and the software FT-Stage (Dumitru, 1993). Age determinations were performed though the zeta calibration method (Hurford and Green, 1983), with zeta values (CN-5 glass) of 335.7 ± 6.6 obtained from Fish-canyon and Durango standar apatites.

For (U-Th)/He dating, hand picking of around 30 inclusion-free and unfractured apatite grains was performed at the LabTer IEE-USP under an Olympus SZX-16 a binocular microscope equipped with a rotating tablet, polarized light and a digital camera. Crystal dimensions necessary to model helium diffusion were recorded and then each grain was packed in a platinum tube. Subsequent analysis were carried out at Potsdam University and in the German research center for geoscience (GFZ). The tubes were heated twice using a diode laser for 5 min, to guaranty total Helium degassing. After helium extraction Pt tubes were dissolved and spiked with ~0.45 ng ^{230}Th and 0.20 ng ^{235}U with approximately 2mL of HNO₃, and U, Th, and Sm analyses were performed on a VG plasma Quad PQ2+inductively coupled plasma–mass spectrometry. Corrections for alpha ejection (Ft) close to the grain borders, were carried out assuming homogenous Ue distributions within the crystals.

6. Results.

River sand samples analyzed in this study mostly correspond to tributaries of the main Cesar River that flows southwestward along the Cesar-Ranchería Valley until reaching the Magdalena River, which in turn flows northwestwards towards the Caribbean Sea. One sample was taken in the Ranchería River, which drains to the north, discharging directly into the Caribbean Sea (Figure 5).

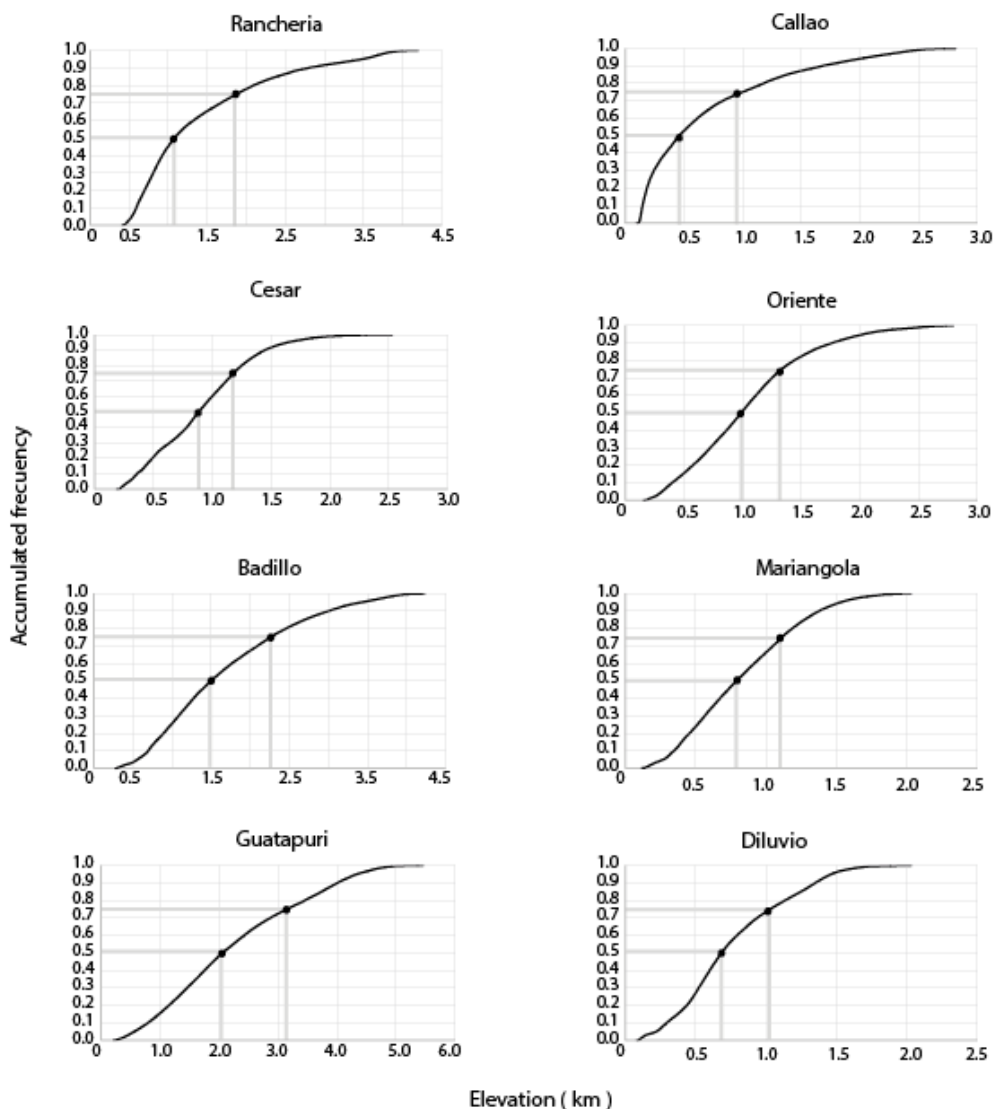


Figure 6. Hypsometric curves for each catchments. High lines are showing the second and third quartile of the accumulated curve....

To begin with the understanding of the age-elevation relationship are considerate the hypsometric curves of each catchment, which show that 75% of their area encompass elevations below 1.8 - 3.0 km for Rancheria, Badillo and Guatapurí catchments and below 1.3 – 1.0 km for Cesar, Callao, Oriente, Mariangola and Diluvio catchments. Based on this, it is expected that those hosting the highest elevations record the oldest cooling ages (figure 6).

In order to establish a correlation between the catchment bedrock geology and the erosional products that are sampled in sand bars, the geological units that crop out in each catchment (Gómez et al., 2015) were grouped according to their composition and represented through pie diagrams (Figure 7). This approach provides an idea about apatite fertility and compositional variability assuming each lithological unit as a possible source of apatite grains

To the northeastern corner, the Guatapurí, Badillo and Rancheria catchments have summits above 4.2 km (Figure 6), and the largest drainage areas, above 300 km². From these, the Guatapurí reach elevations above 5.4 km and an area of 840 km². Nevertheless, the Cesar catchment also located in the northeast has its summit at 2.5 km with a smaller area of 230 km². These northeastern catchments comprise lithological units mostly of acid composition, as Jurassic intrusive and volcanic rocks (Figure 7). The Guatapurí include a high proportion of high-grade metamorphic rocks of Proterozoic ages.

Unlike in the north, the southern catchments are characterized by elevations at their summits below 2.8 km (Figure 6) and comprise drainage areas smaller than 270 km². From these, Mariangola and Diluvio present the lowest summits with elevations at ~2.0 km. The southwestern catchments comprise a wider variety of rock types, including abundant Jurassic volcano-sedimentary rocks, although acid igneous rocks are still more abundant (Figure 7).

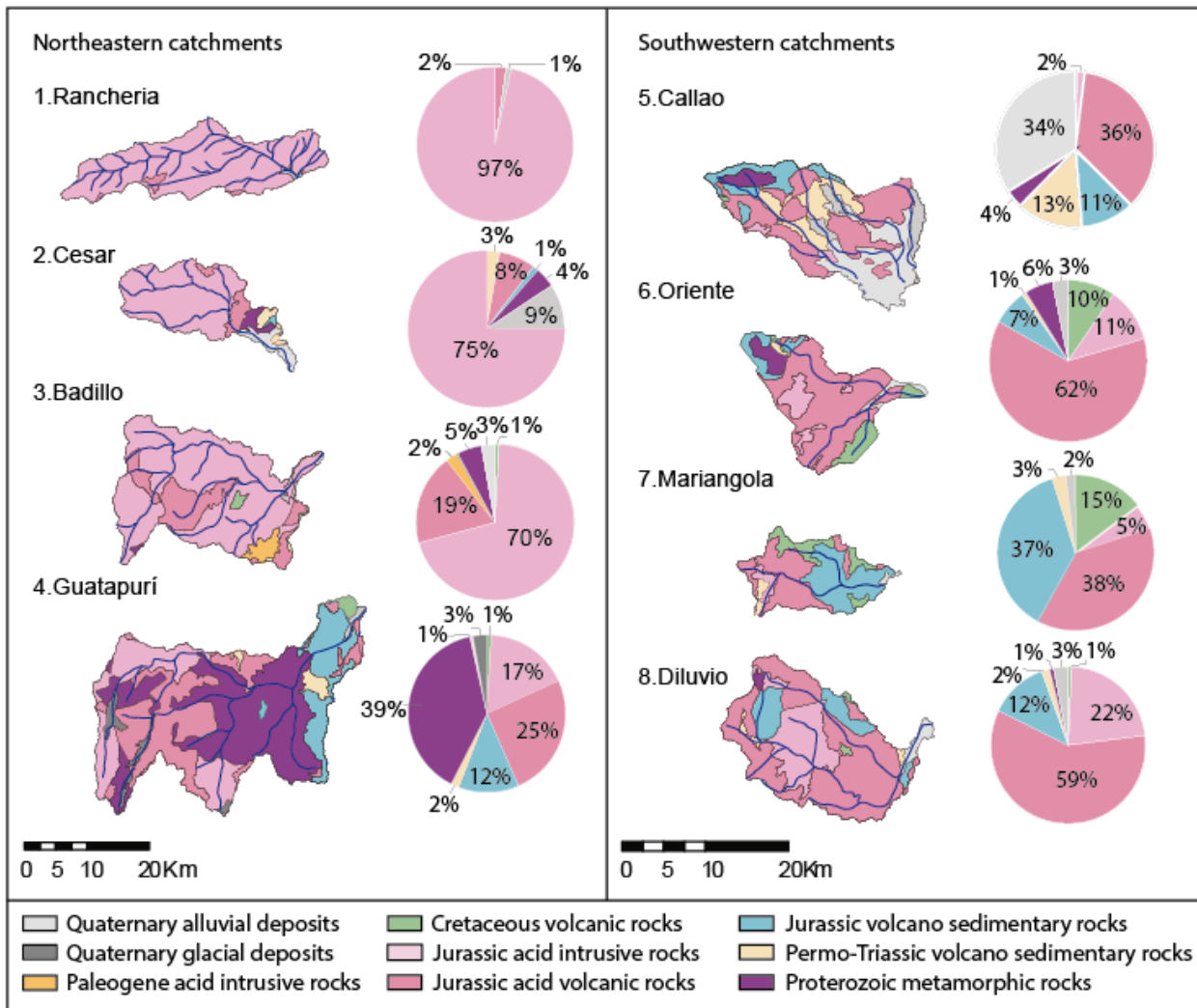


Figure 7. Simplified geological maps (Gomez et al., 2015) of each catchment area and pie charts showing relative proportion of each rock type.

Regional geological mapping (Goméz et al., 2015) demonstrate widespread occurrence of rock types known to contain apatite. Fluorapatite is usually related to granitic rocks and chlorapatite usually occurs in basic igneous rocks (Mange and Maurer, 1992). Thus, it is expected a predominance of fluorapatite, probably derived of the multiple acid intrusive lithologies, over chlorapatite that are restricted to mafic components of Paleo-Mesozoic volcano-sedimentary sequences (Figure 7). In this sense, the age distributions obtained will be controlled probably by an exhumation process rather than by compositional differences.

6.1 Thermal conditions

The multiple deformational events that have been documented in the northern South American margin since the Late Cretaceous (see reviews in Mora et al., 2015) and preserved Cenozoic strata in surrounding basins support a history of non-monotonic cooling. In this regard, stratigraphic cross-cutting relationships from the Cesar-Rancheria basin provide valuable information for thermal history constraints. Here, the Aptian-Maastrichtian (125-66 Ma) sedimentary sequence rests unconformably over Triassic-Jurassic rocks (Caceres et al., 1980). This unconformity crops out in the east-dipping monocline along the northeastern sector of the Santa Marta massif and is useful as reference point for estimations of the structural depth reached by rocks at the summit and outlet of each catchment in Aptian time (125-113 Ma). Such estimation was done by projecting the basal Cretaceous unconformity cropping out in the Cesar-Rancheria basin westwards over the catchment topographic profiles using a range of strata dip angles of 10-15°, based on available information in the geologic maps (Figure 8). The range of temperatures corresponding to the structural depths of the rocks cropping out at the summits and outlets was then calculated for geothermal gradients of 30°C/km and 40°C/km, considering that heat fluxes during Aptian time were higher due to former Neocomian back-arc extension (Sarmiento et al., 2006) (Table 1).

We obtained structural depths between 4.6-0.8 km and 9.0-2.2 km for the summits and of 2.0-0.2 and 3.0-0.9 km for the outlets, considering a dip angle of 10 and 15° for the Cretaceous strata respectively (Table 1). We inferred that Pre-Cretaceous rocks were not completely reset for AFT during pre-Aptian burial and some ages probably captured in the regional distribution correspond to former thermal events different to the Cenozoic orogenesis.

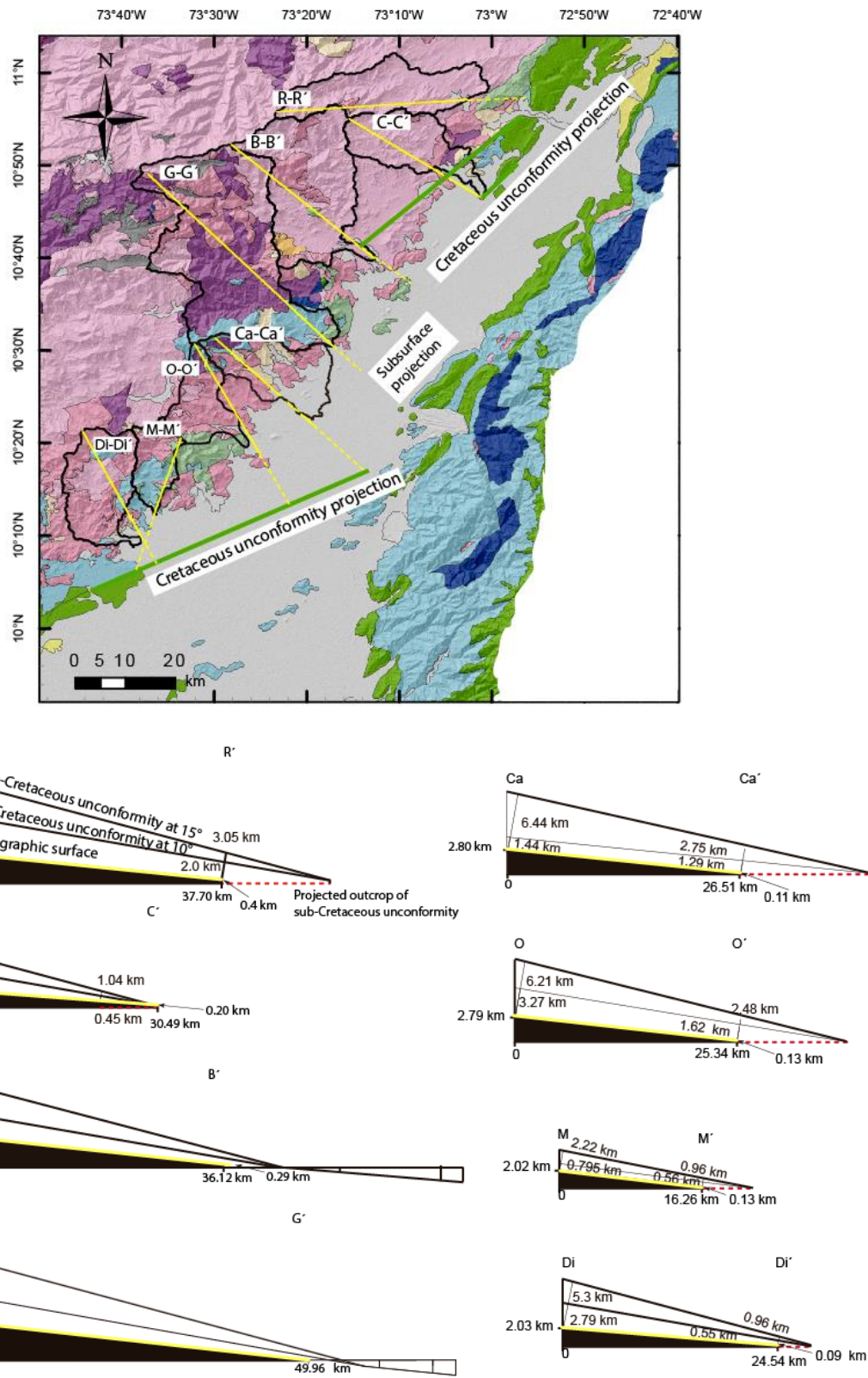


Figure 8. Example of the procedure in the calculation of the structural depth.

Table 1. Estimations of paleo-depths and corresponding maximum temperatures reached by pre-Cretaceous rocks during Aptian time currently cropping out at the summit and outlet of each catchment. See Figure 5 for further explanation

Catchment	Structural depths		Paleo-thermal gradients		
	Summit. km	Outlet. km	40°C/ km	30°C/km	
Dip 10°					
Ranchería	4.6	2.0	206	100	159
Cesar	2.8	0.4	132	38	104
Badillo	3.0	0.6	140	44	110
Guatapurí	3.7	0.2	169	28	131
Callao	1.4	1.3	78	71	63
Oriente	3.37	1.6	151	84	118
Mariangola	0.8	0.6	52	42	43
Diluvio	2.89	0.5	132	42	103
Dip 15°					
Ranchería	9.0	3.0	382	142	291
Cesar	5.5	1.0	240	61	185
Badillo	6.5	1.3	280	72	215
Guatapurí	8.5	0.9	359	56	274
Callao	6.4	2.7	278	130	213
Oriente	6.2	2.5	268	119	206
Mariangola	2.2	0.9	108	58	87
Diluvio	5.3	0.9	232	58	179
					486

6.2 Detrital thermochronology

Only three of the eight river sand samples provided less than 80 apatite grains (around 60) for AFT analysis. We also select samples of three catchments, Rancheria, Badillo and Guatapurí, for AHe dating of around 30 grains. Furthermore, we present AFT data of the Manaure River, located at the western flank of the Perijá range, but apatite content allow analyzing only 30 grains (Appendix I). The results are presented as age peaks found in the Kernel Density distributions of the age populations, using the software Density Plotter (Vermeesch, 2012), which take into account the local density of data in the distribution. Validity of the age peaks was tested analyzing each one as an individual population using the χ^2 statistic and presenting them in radial plots in order to obtain a central age (Galbraith, 1988, 1990, see appendix II). All age populations conforming the peaks

of each distribution have P-values > 0.05 and their central ages are close to the age peaks of the distribution. Those peaks with a proportion less than 10%, considering the lower value of the error interval, (Figure 9, Table2) must be interpreted carefully because they can result from few close ages or over a numerous disperse ages at the tails of the distributions.

We observe a good direct correlation between catchment elevations and the oldest individual AFT ages. The northeastern catchments Ranchería, Badillo and Guatapurí, with their summits at 4.2-5.5km contain a wide age spectrum of individual ages reaching values up to 155 Ma (Figure 9). In contrast, the smaller and lower elevation catchments Cesar, Callao, Oriente, and Mariangola exhibit oldest individual ages of around 83 Ma. An exception to this pattern is the Diluvio catchment, which, with a summit at 2.0 km, contain ages >150 Ma.

The Rancheria and Badillo catchments present the oldest age peaks at 131 Ma and 115 Ma, respectively. On the contrary, similar age peaks are absent in the Guatapurí catchment, where the oldest age peak is 62 Ma. On another hand, the northeastern catchments include a significant age peak at 60-45 Ma. Only a minor signature (<10%) of this interval is found in the Cesar and in the southwestern catchments. An age peak at 78 Ma is solely found in the Diluvio catchment (Figure 9).

Although, magmatism has been documented in the northwestern region of the massif at 50-58 Ma (Cardona et al., 2011a, Salazar et al., 2016), geobarometry data, support an emplacement depth of 16-19 km (Cardona et al, 2011b), where temperature significantly exceeds the closure temperature of the thermochronometric techniques used here (120° for AFT and 70°for AHe). In this sense, the 60-45 Ma age peak can represent cooling ages by exhumation rather than by cooling following crystallization of magmatic bodies that were emplaced in the study region (Figure 3).

A subsequent interval of cooling ages between 25-20 Ma is found in both, AFT and AHe data (Figure 9 and 10). Significant AFT age peaks are present in the Cesar and Guatapurí catchments to the northeast, as well as in all others catchments to the southwest. A minor proportion (<10%) of grains with this age are present in the Rancheria and Badillo catchments. Similarly, AHe data of Guatapurí and Badillo catchments show their main peak at around 20 Ma.

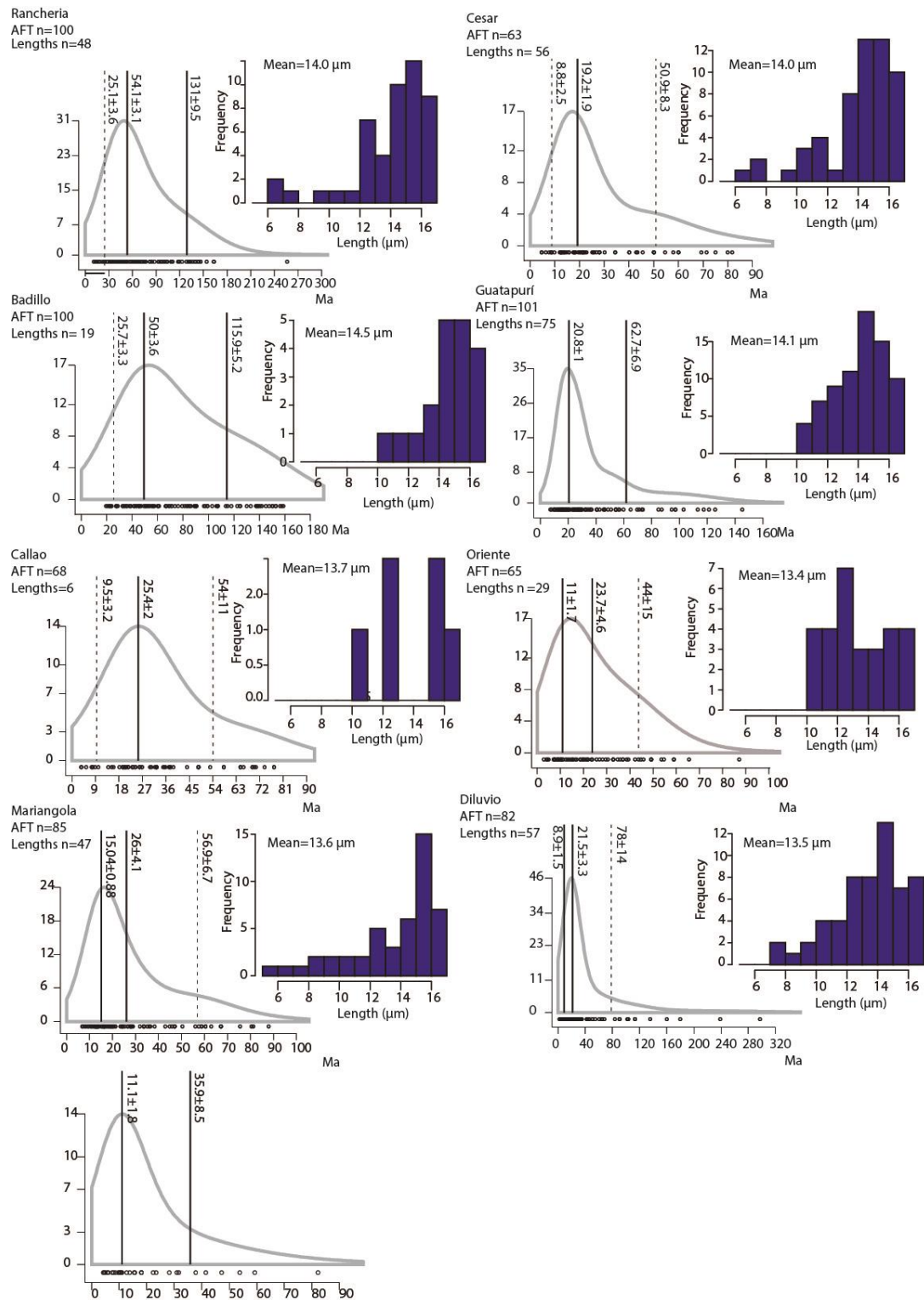


Figure 9. Kernel Density Estimator^{Ma} diagrams of detrital AFT age distributions. Solid lines denote peaks with populations >10% and dashed lines with populations <10%. The histograms correspond to uncorrected lengths tracks measurements.

Table 2. Age peaks derived from age distributions of each sample with their proportions (%)

Sample	n	P1 (Ma)	P2 (Ma)	P3 (Ma)
Ranchería	100	25.1±3.6	54.1±3.1	131±9.5
		11.3±5.3%	60.6±7.3%	28.1±9.1%
Cesar	63	8.8±2.5	19.2±1.9	50.9±8.3
		10±10%	66±11%	24±15%
Badillo	100	25.7±3.3	50±3.6	115.9±5.2
		10.6±5.4%	42.6±7.2%	46.9±9%
Guatapurí	101	20.8±1	62.7±6.9	
		73.6±5.9%	26.4±5.9%	
Callao	68	9.5±3.2	25.4±2	54±11
		8.6±5.6%	70±12%	21±14%
Oriente	65	11±1.7	23.7±4.6	44±15
		38±12%	47±19%	15±23%
Mariangola	85	15.04±0.8	26±4.1	56.9±6.7
		51±9.9%	28±10%	21±14%
Diluvio	82	8.9±1.5	21.5±3.3	78±14
		21±10%	55±11%	24±15%
Manaure	32	11.1±1.8	35.9±8.5	
		72±13%	28±13%	

The youngest AFT age population in the eastern slope of the Santa Marta massif corresponds to 16-10 Ma (Figure 9). Significant populations of this age are concentrated in southwestern catchments, but a minor proportion of this population is also found in the Cesar and Callao catchments. Additionally, AHe data of the Rancheria catchment yield an age peak at 16 Ma (Figure 10).

The Manure sample, from the western flank of the Perijá Range, has two age peaks of 35.9 (28%) and 11.1 (72%) (Figure 9). The older peak could be related to the interval 60-45 Ma considering its error range (Table 2); however, this peak constitute overdispersed data in the tail of the distribution, hampering the correlation with peaks from other locations in the Santa Marta Range. Unlike the youngest peak, of 11 Ma that is significant and can be correlated with the youngest population of the eastern side of the Santa Marta massif.

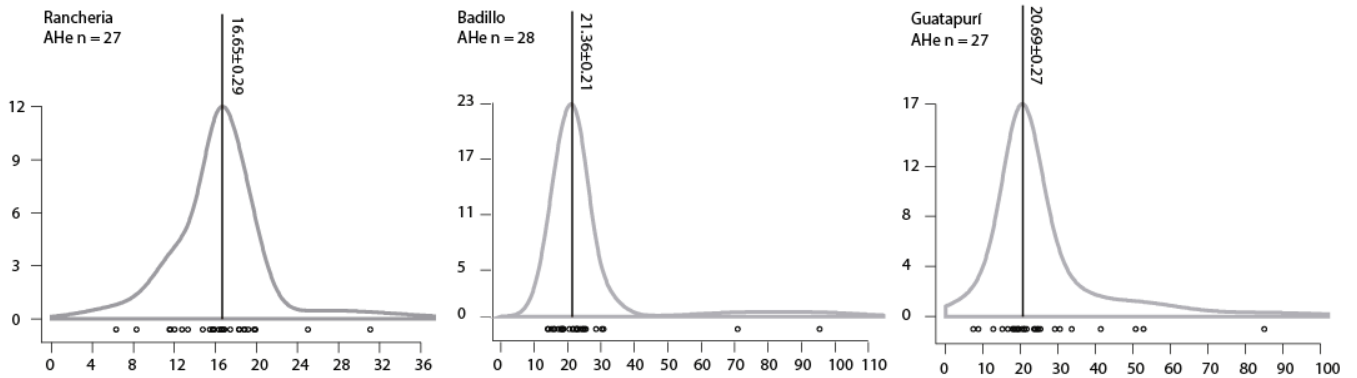


Figure 10. Kernel Density Estimator diagram of detrital AHe age distributions. Solid lines denote the age of the main peak of the distribution

Fission-track length uncorrected measurements show a wide range of values (5.3-16.7 μm) (Figure 9), with predominance of long lengths and mean values of 14 μm , suggesting the presence of grains with low and high degree of partial annealing. The Rancheria and Cesar samples, located to the northeast, and the Mariangola and Diluvio samples to the southwest, present fission track lengths as short as $\sim 6\mu\text{m}$, while the minimum lengths of the other samples are $\sim 10\mu\text{m}$.

Dpar measurements also yield a wide range of values, comprising intervals of 0.8-2.3 μm , 1.3-3.3 μm and 1.12-4.6 μm , for the Rancheria-Badillo-Guatapurí, Callao-Oriente-Mariangola, and Diluvio-Cesar samples, respectively. A random distribution of Dpars (Figure 11), uncorrelated with grain ages, suggest that ages are controlled by the cooling history of the grains rather than by their kinetic characteristics

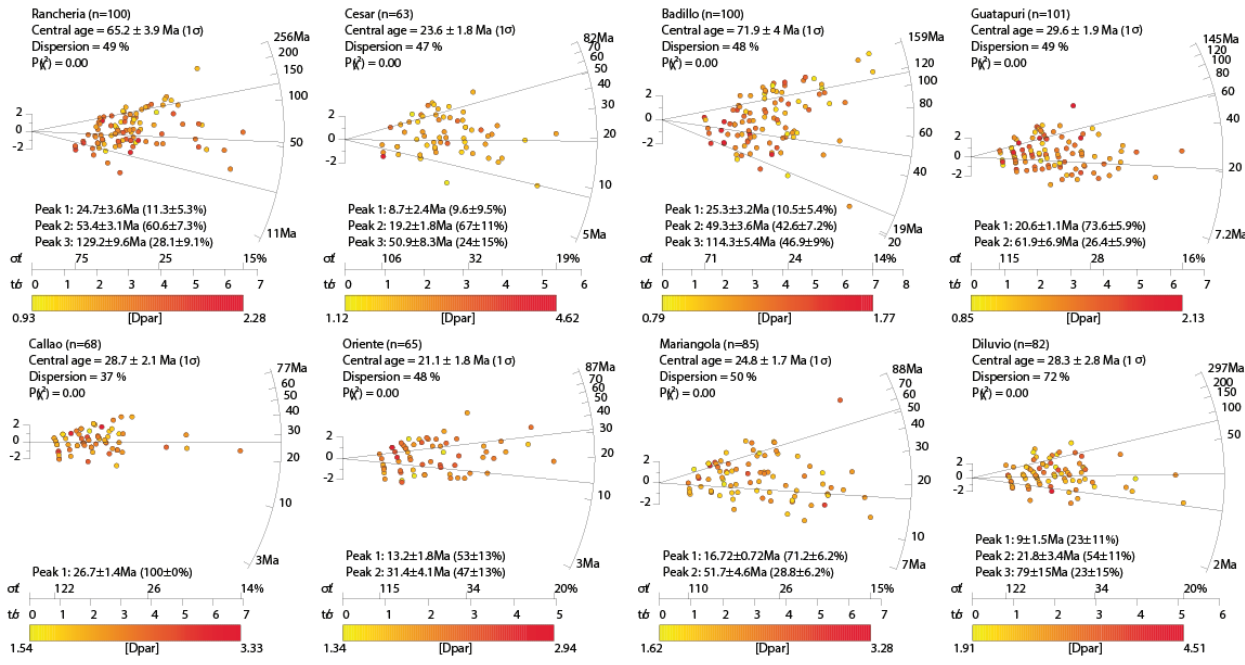


Figure 11. Radial plots for Dpar measurements vs ages.

Some grains of the Guatapurí sample further provide pairs of age - length measurements (Table 3) that allow knowing the particular thermal history of this population of grains. These data are used to model the thermal history using the software Hefty (Ketcham, 2005).

Table 3. Grains of the Guatapurí sample used to model in Hefty. Each grain has both age and uncorrected length measurements.

Grain	Length (μm)	Ages (Ma)
1	16.83	15.55
2	16.54	20.34
3	15.80	18.40
4	15.79	16.57
5	15.35	16.57
6	15.08	20.34
7	14.89	15.55
8	14.30	13.50
9	14.26	29.36
10	13.80	27.26

Grain	Length (μm)	Ages (Ma)
11	11.81	9.58
12	10.81	32.51
13	10.67	15.31

Two constrains are imposed to the model, one comprising the onset of Cretaceous (125-113 Ma) sedimentation marked by the unconformity contact between the basement and the basal strata of the sedimentary sequence, and the another one related to recurrent paths took by the software when searching for thermal solutions.

We obtained a thermal history solution with the best-fit model showing cooling during 44 to 14.5 Ma from $>150^\circ\text{C}$ to 100 at a rate of $1.8^\circ\text{C}/\text{My}$, and a subsequent faster cooling until reaching surface temperature (Figure 12).

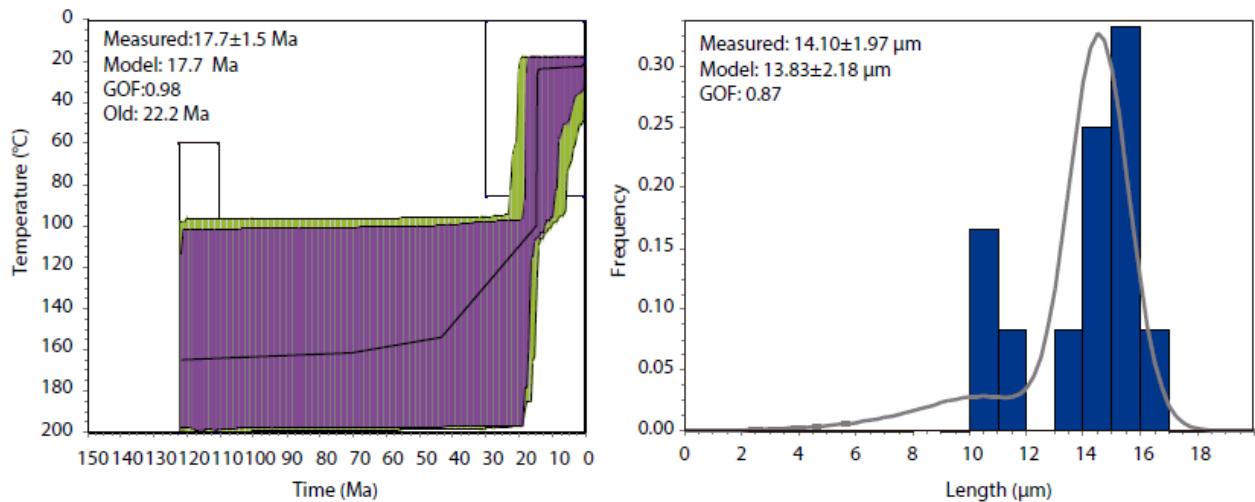


Figure 12. Thermal history model for selected grains of the Guatapurí catchment in which both, ages and track length measurements are available.

6.3 Interpretations

A thermochronological age is the result of the accumulation of the radioactive products inherent to a particular thermochronometer (e.g., AHe, AFT) within the crystalline structure of minerals. Such accumulation reflects the concurrent processes of radioactive production, which is a function of time, and radiogenic loss, which is modulated by temperature. The practical consequence of the simultaneous occurrence of such processes is that thermochronological ages should be interpreted in the broad setting of the thermal history of a region, considering the multiple possible stages in its evolution, rather than a merely punctual event of cooling straightforwardly associated to exhumation. Complementary data as fission tracks lengths provide insights into the thermal histories because they are also time-temperature dependent. In this study, the predominance of long track lengths measured in river sand samples are consistent with an overall rapid cooling of the source areas. Accordingly, the ages peaks found can be used as a proxy of pulses of exhumation involving the eastern side of the Santa Marta massif during the Cenozoic.

The current Andean orogenesis in the northern Andes has been dated as old as 75 Ma (Spikings et al., 2010), triggered by the diachronous collision of Caribbean volcanic arc against the western continental margin (Burke, 1988; Pindell and Kennan, 2005). In this sense, cooling ages peaks older than 75Ma are interpreted here as unreset ages, whilst younger ages are associated to pulses of exhumation of the current Andean orogenesis, as those found in the Central Cordillera (Villagomez and Spikings ., 2013).

We interpret the age peak of 60-45Ma present in the northeastern catchments along the Santa Marta massif (Figure 13) as a preserved signature of the initial Andean exhumation pulses associated with collision of an Caribbean derived oceanic arc against western Colombia (Spikings et al., 2010, Villagomez et al., 2013, León et al., 2018). The significant occurrence (>10%) of age peaks in this time interval restricted to high elevated catchments allow us to speculate that apatite grains with these ages are derived from upper reaches of the catchments. Similar ages, albeit at lower elevations, have been reported in the bedrock data along the Central Cordillera (Gómez, et al., 2005, Restrepo-Moreno et al., 2009, Villagómez et al.,2013) and the San Lucas Range (Caballero et al., 2013).

A subsequent pulse of exhumation at 25-20Ma (Figure 13) is reflected in AFT and AHe age peaks found in both, high and low elevation catchments except in the AFT data of the Ranchería and Badillo, where these are weakly defined (Table 2). Meanwhile, AHe data of Badillo and Guatapurí catchment present an age peak at 21 Ma (Figure 10), reflecting a rapid cooling accounting for the short time required to pass through the closure temperature of the AFT and AHe systems (120°C and 70°C, respectively). This time interval comprise major changes of the plate tectonic setting, namely the breakup of the Farrallón Plate at 25 Ma to give rise to the Nazca and Cocos plates (Pilger , 1984), and the subsequent increase of the rate of convergence from 55mm/yr to >100 mm/yr between Nazca and South American plates (Pardo-Casas and Molnar, 1987). These events are coeval with a differential motion between North and South America that yielded 92 km of convergence (Müller et al., 1999).

A coeval pulse of exhumation is present in the Perijá range and correspond to the initial uplift of this basement block (Shagam et al., 1984). At this time, a major unconformity is recorded in the sedimentary sequence of the Maracaibo Lake (Kellogg 1984). Similarly, mountain building along the eastern margin of the Eastern Cordillera was ongoing at this time interval as consequence of the eastward advance of Andean deformation (Parra et al., 2009).

The ages peak of 10-16 Ma represent the youngest signal of exhumation (Figure 13) and is preferentially found in the southern, low elevated catchments and in the Manaure catchment along the western flank of the Perijá range.

AFT and AHe ages of 10-16Ma have also been reported in the bedrock data of the northwestern Santa Marta Massif (Villagomez et al., 2011b) and the Western Cordillera (Leon et al 2018). Unlike in the Western Cordillera, where such ages have been related to collision of the Panama Arc (Leon et al., 2018), we interpret that these ages in the eastern Santa Marta massif represent eastward migration of the deformation towards the Perijá range. Our interpretation reflects an asymmetric along-strike exhumation pattern whereby young ages are restricted to low elevation reaches of catchments located closer to the Perijá range. The paucity of Miocene stratigraphic record in the Cesar-Rancheria basin (Geopetrocol 1998) suggest that the 10-15 Ma uplift may have been an event ubiquitous from the Santa Marta massif to the Perijá range.

Our data and published ages reveal a broad record of post-Eocene cooling, and differs from previous accounts that have identified this pulse of exhumation only in proximity to the Santa Marta-Bucaramanga fault and north of the Sevilla lineament (Villagomez et al., 2011b).

The dataset obtained in this study demonstrate the utility of detrital thermochronology for retrieving the main exhumation patterns in areas with difficult access by sampling detritus from a wider range of elevations than what is usually achieved with bedrock sampling. Despite the unsuitability of this method for constructing the type of robust thermal histories that individual bedrock samples allow, the fast cooling events interpreted from long tracks lengths and similar AFT and AHe peaks furnish a more direct meaning to the numerical age peaks observed.

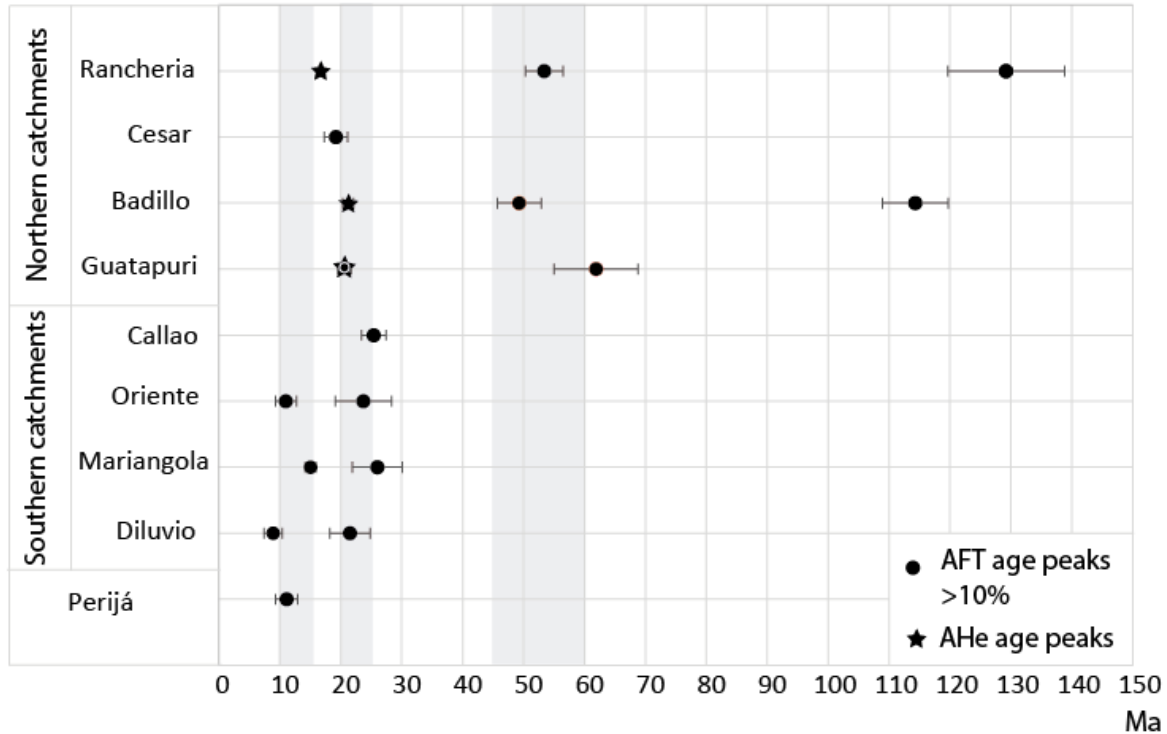


Figure 13. Summary of main ages peaks in geographical arrangement. Shaded areas represent exhumation pulses proposed. Only populations made of >10% of the total spectra are presented

6.4 Exhumation rates

We estimate integrated maximum exhumation rates understood as the velocity of erosional or tectonic dependent displacement of rocks with respect to the Earth surface (England and Molnar, 1990). This was done by taking the youngest AFT and AHe age peaks (Table 2) are assumed as the approximate age of the passage of the rocks through the 120°C and 70°C isotherms, resulting in isotherm depths of 4-5 km and 2-2.5 km, respectively, based on assumed paleogeothermal gradients of 20°C/km and 25°C/km, and a surface temperature of 20°C. Those samples with available pair of AFT and AHe data allow estimating changes in the exhumation rate for each portion of crust involving their closure temperatures (2 and 2.5 km for both intervals 120-70°C and 70-20°C). No thermal perturbations associated to the influence of topography and rapid cooling are considered here for simplicity, although we acknowledge that such assumptions do not reflect the conditions that occur in nature.

Using a similar approach, we further explore the range of ancient exhumation rates provided by published detrital AFT and ZFT data (Piraquive et al., 2017) from the Miocene sedimentary record of marginal basins located to the north (Palomino) and to the west (Aracataca, Figure 3). We assume a closure temperature for the ZFT system of 250°C (Bernet et al., 2009).

Table 4. Integrated maximum exhumation rates based on the youngest age peak identified in different river catchments from the eastern Santa Marta massif and the Perijá range.

Catchment	Youngest age peak (Ma)	1σ	Δtime (tc120°C-tc70°C)	Exhumation rate 20°C/km	Exhumation rate 25°C/Km
Ranchería AFT	25,1	3,6	8,45	0,30	0,24
Ranchería AHe	16,65	0,29		0,15	0,12
Cesar AFT	8,8	2,5		0,57	0,45
Badillo AFT	25,7	3,3	4,34	0,58	0,46
Badillo AHe	21,36	0,21		0,12	0,09
Guatapurí AFT	20,8	1	0,11	22,73	18,18
Guatapurí AHe	20,69	0,27		0,12	0,10
Callao	9,5	3,2		0,53	0,42
Oriente	11	1,7		0,45	0,36
Mariangola	15,04	0,8		0,33	0,27
Diluvio	8,9	1,5		0,56	0,45

Catchment	Youngest age peak (Ma)	1σ	Δt (tc120°C-tc70°C)	Exhumation rate 20°C/km	Exhumation rate 25°C/Km
Manaure	11,1	1,8		0,45	0,36
Sample	Youngest age peak (Ma)	1σ	Δt (tc250°-Tc120°)/Lag time	Exhumation rate 20°C/km	Exhumation rate 25°C/Km
Aracataca ZFT	29,20	1,50	10,00	0,65	0,52
Palomino ZFT	32,90	3,15	6,10	1,07	0,85
Aracataca AFT	19,20	2,10	4,20	1,19	0,95
Palomino AFT	26,80	3,25	16,80	0,30	0,24

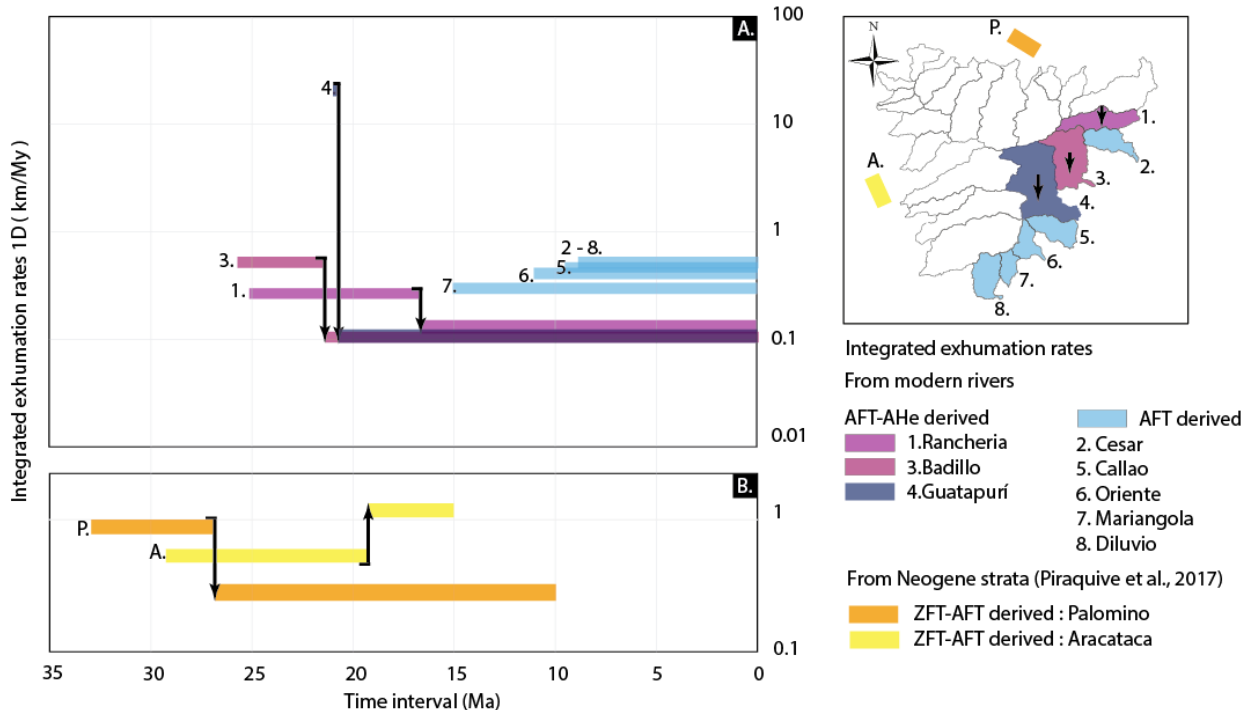


Figure 14. A: Exhumation rates calculated from the youngest age peak of detrital samples obtained in modern rivers. B. Exhumation rates .calculated from the youngest age peak of detrital samples obtained in Neogene strata of the marginal basins Aracataca and Palomino (Piraquive et al , 2017).

Exhumation rates calculated from AFT and AHe ages conjugated (Rancheria, Badillo, and Guatapurí) suggest a deceleration around the early Miocene. Particularly, the Guatapurí sample exhibits a great scale of this, explaining the so close age peaks of AFT and AHe. For these catchments, recent exhumation rates of the ~2-2.5 km uppermost portion of the crust are between 0.09-0.15 km/my. Unlike, the rest of the catchments, whose hosting minor elevations, present

higher exhumation rates for the 4-5km uppermost portion of the crust, with maximum values of 0.57km/My (Figure 14, Table4).

On the other hand, the Miocene sedimentary sequences to the north (Palomino) and to the west (Aracataca), show exhumation rates of a deeper portion of the crust (11.5-9.2 and 5-4km) around 1.07-0.85 km/my and 0.65-0.52 km/my respectively, during the early Oligocene. To the north since the late Oligocene to late Miocene such rates decreased to 0.30-0.24 km/my, values similar to the recent exhumation rates recorded in the Rancheria catchment, also located to the north. While in the Aracataca sequence at ~20Ma is recorded an increase of exhumation rates reaching values of 1.19-0.95 km/my (Figure 14, Table 4).

Such distribution of exhumation rates defines an asymmetrical pattern with lower denudation acting over northern during the Miocene and a faster erosion to the west. Modern rates in the catchments are significantly lower than pre-Miocene rates calculated for the northern and western sectors of the range in the marginal basins (Figure 14).

7. Termokinematic modeling

Detrital cooling ages of modern sediments are the result of the integrated thermal history of their multiple source areas and thus 1-D models are insufficient to describe fully the thermal evolution of the entire region. For this reason, we employ 3-D thermokinematic modeling using the numerical code PECUBE (Braun 2003). In a crustal block with topographic and a fault kinematic evolutions prescribed independently, this numerical model solves in three dimensions the heat-transfer equation (1).

$$\frac{\delta T}{\delta t} + u \frac{\delta T}{\delta x} + v \frac{\delta T}{\delta y} + w \frac{\delta T}{\delta z} = \frac{\delta}{\delta x} K \frac{\delta T}{\delta x} + \frac{\delta}{\delta y} K \frac{\delta T}{\delta y} + \frac{\delta}{\delta z} k \frac{\delta T}{\delta z} + A \quad (1)$$

where, $T(x,y,z)$ is field temperature, K is the thermal diffusivity, A is the radioactive heat production and u,v and w are components of the general velocity field described by the advection of rocks due to their displacement along a single or multiple faults (Braun et al., 2012). In doing so, this type of thermokinematic modeling is capable of translating thermal histories into thermochronometric ages using available kinetic models, thereby enabling the comparison of modeled ages with measured ages and hence the validation of plausible topographic and kinematic

scenarios. This 3-D modeling methodology allow investigating the thermal response of a portion of crust to exhumation processes involving the bulk of the Santa Marta massif.

The methodology involves the generation of multiple individual models and for each of them the evaluation of the misfit between modeled and observed ages, the latter including published bedrock AFT and AHe data, through the log-likelihood function (LLH):

$$LLH = \sum_{i=1}^N \left(\frac{\ln(2\pi)}{2} + \ln(\sigma_i) + 0.5 \left(\frac{\alpha_{i,mod} - \alpha_{i,dat}}{\sigma_i} \right)^2 \right) \quad (2)$$

where N is the number of data points (thermochronological ages), $\alpha_{i,mod}$ and $\alpha_{i,dat}$ are the modeled (i.e., predicted) and observed ages for data point i, respectively, and σ_i is the uncertainty on the data. We finally compare predicted ages of the best model found with measured detrital cooling ages for the area of each catchment, through boxplot diagrams and their statistical parameters.

Values of log-likelihood (LLH) closer to “0” reflect a better fit between them. AHeLLH and AFTLLH refer to the sum of the individual values of loglikelihood estimated for every AHe and AFT cooling age, respectively, and Total LHH refers to the sum of AHeLLH and AFTLLH.

All models are run with a series of fixed geometric thermal and elastic parameters, as described in Table 5 and were developed in a unique tectonomorphic scenario of steadily growing topography from flat to present-day conditions since 65 to 0 Ma

Table 5. Geometric, thermal and elastic parameters common to all Pecube models.

Parameter (units)	Value
Crustal density (kg/m ³)	2.700
Mantle density (kg/m ³)	3.200
Young modulus (Pa)	1
Poisson ratio	0.25
Elastic plate thickness(km)	28.8
Model thickness (km)	40
Thermal diffusivity (km ² /Myr)	25
Basal model temperature (°C)	750
Sea level temperature	25

Parameter (units)	Value
Atmospheric lapse rate ($^{\circ}\text{C}/\text{km}$)	6
Crustal heat production ($^{\circ}\text{C}/\text{Myr}$)	0

The model geometry is defined by a main fault A located at N45°E in western end of the range (Figure 15A) and striking parallel to the Agujas and Sevilla faults. Our approach attempt to reproduce the eastward tilting of the massif and the northwestward younging in thermochronometrical ages, rather than to trustworthy reproduce the kinematics of the range.

Two kinematic scenarios were designed in order to obtain a NW-SE gradient in vertical exhumation rates (figure 15A): (1) Models Group 1 are generated with fault A dipping eastwards, with either a ramp-flat, listric or circular geometry at depth; (2) Models Group 2 is defined by an arrangement of four vertical faults (A,B,C,D) separated by successive distances of 45, 30 and 25 km and with fault velocities diminishing eastwards. Both kinematic scenarios are developed for the same time interval (65 Ma to present)

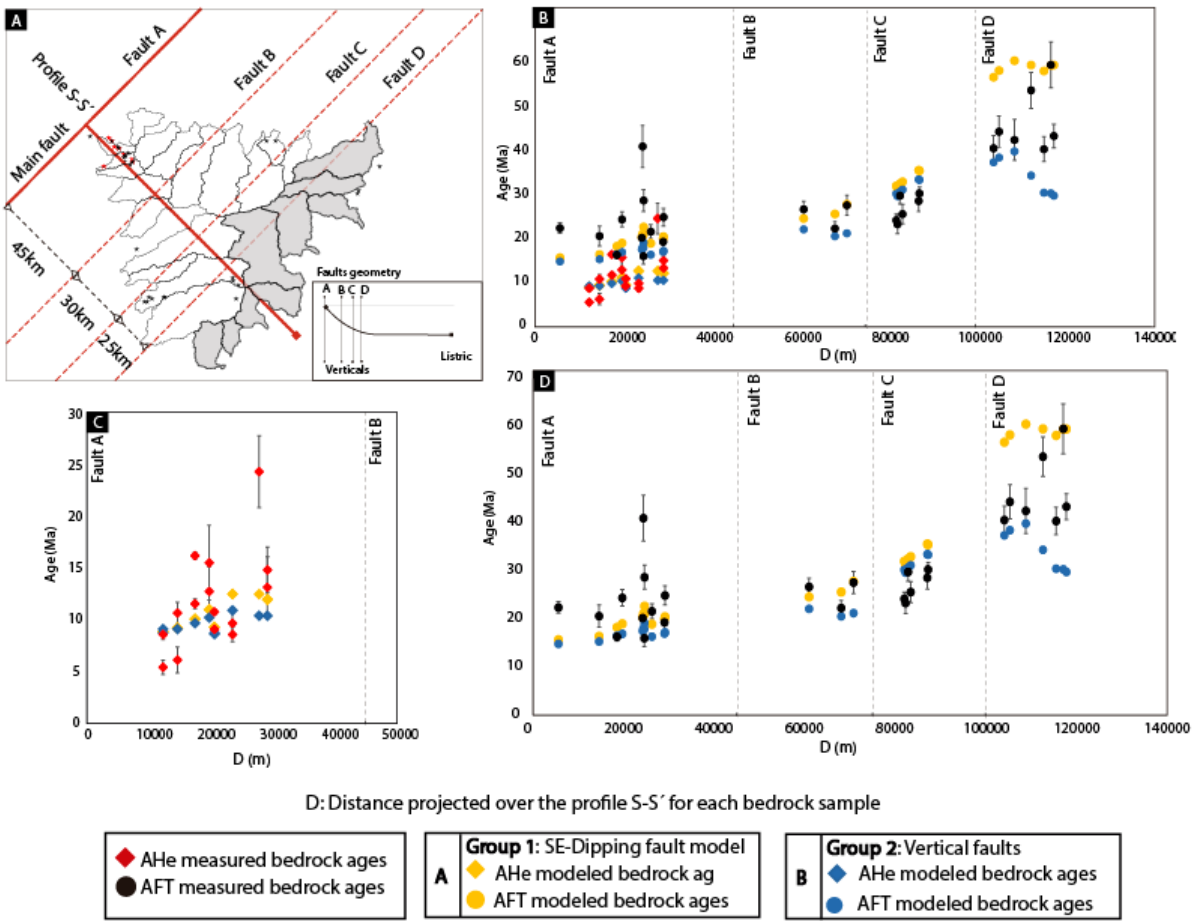


Figure 15. A. Model settings. Gray areas represent catchments with detrital thermochronological ages obtained in this study. B. comparison between bedrock ages of the best models for each group and the measured ones (Villagómez et al., 2011b, Cardona et al., 2011b).C. Detail of the AHe ages comparison. D. Detail of the AFT ages comparison.

Models group 1: Single fault with variable geometries at depth.

A first set of models were designed to test the effect of different fault geometries on the vertical exhumation rates. We run simulations using similar topographic evolutions but with different fault velocities (Figure 16). The models with higher LLH show that the fault velocities that better reproduce both the AFT and AHe thermochronometric data are 0.20-0.35 km/myr (Figure 16A). The results show that either circular or listric geometries better reproduce the data, as these geometries are those that involve a gradient in vertical displacement, being faster to the western sector of the range. A ramp geometry, which involve uniform vertical displacement along the whole hanging wall, does not reproduce adequately the data (Figure 16 A). The best model is one with a listric fault with a velocity of 0.32 km/myr. These velocities represent the integrated fault velocities

since 65 Ma. However, AFT data, representing the exhumation of the uppermost 4-5 km of exhumation are better reproduced with lower velocities, with a range of 0.10-0.20 km/yr (Figure 16 B-C), whereas AHe data, representing the erosion of the uppermost 2.0-2.5 km of crust, require faster vertical displacements, of 0.20-0.40 km/my (Figure 16 B-C). Altogether, this modeling results support fault acceleration anytime since the Miocene

Models group 2: multiple faults with vertical geometry

A second group of models was run imposing a kinematic scenario of vertical displacement only. We chose to reproduce the SE tilting by reproducing the exhumation with 4 vertical reverse faults striking also N45°E (Figure 15 A) and with westward decreasing fault velocities, all them starting to operate at 65 Ma. The location of the westernmost fault (A) was chosen at the same location of the faults using in the first group of models, the remaining 3 faults, B, C and D being located at 25, 30 and 45 km southeastwards (Figure 15 A).

Based on the results of the models with southeast-dipping faults, in which best models with 0.2-0.35 km/my along listric or circular faults set up the maximum vertical velocity, we tested models in which we assign an initial set of velocities for faults A, B, C and D, and then systematically vary the velocity of each fault, starting with fault A, until finding the best model. We depart from initial values of 0.20, 0.12, 0.09 and 0.04 km/my for faults A,B,C and D, respectively, and run a set of 65 models, initially varying only fault A and then each of the remaining faults. The best model require velocities of 0.26, 0.18, 0.13, and 0.13 km/my and imply exhumation rates of 0.05 to 0.26 km/my (Figure 18).

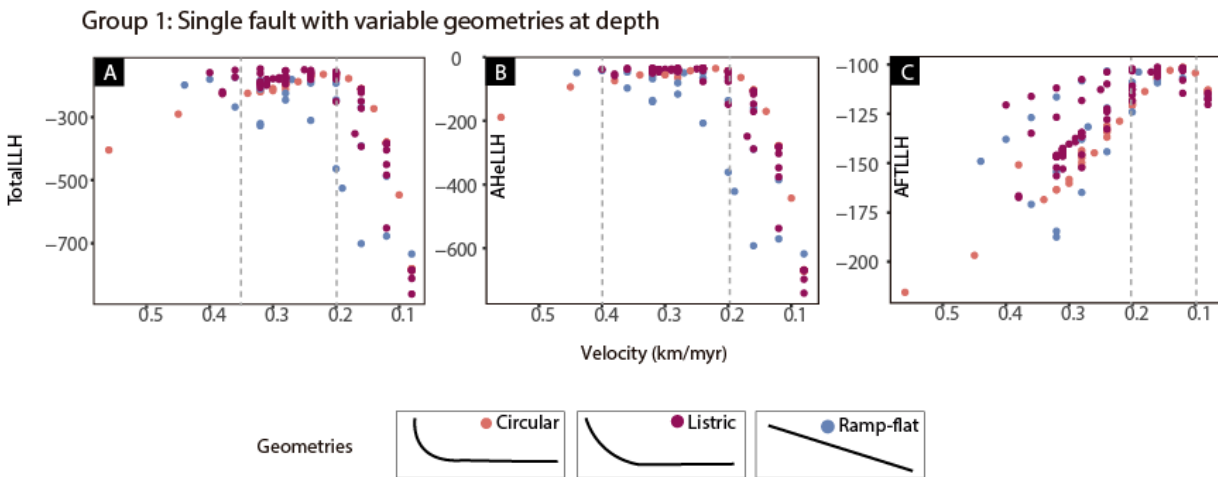


Figure 16. Relation between fault velocity and misfit (evaluated with the log-likelihood, LLH) for different fault geometries. A: Total LLH using both AFT and AHE data. B: LLH using AHe data only. C: LLH using AFT data only.

Modeled ages of the best simulation (i.e, that with the highest Total LLH) of each group of models, Model A for the Group 1 and Model B for the Group 2, are compared with measured ages along a NW-SE profile across the range (Figure 15 B). Both models yield similar cooling ages, slightly younger for the model B, except in the easternmost block, where modeled ages are significantly older than measured ages for the model A, and slightly younger yet closer to observed ages for model B. Comparison between measured and modeled bedrock ages suggest that the asymmetry in the pattern of exhumation can be respond to both , a single rigid crustal block or a multiple discrete blocks setting.

Best models for each group (models A and B) were also used for comparison with detrital ages measured in this study (Figure 17). The fit between them was tested through the central tendency derived from boxplots diagrams that refers to the median statistical parameter and reflect the values below which half of the data are concentrated. Thus, the goodness of fit between measured and predicted cooling ages are qualitatively established by comparing the 95% confidence interval obtained in each data set.

Boxplot diagrams for measured detrital cooling ages reveal some clusters of central tendencies: 45 Ma for Rancheria and Badillo, 20 Ma for Cesar, Oriente, Mariangola and Diluvio and 25-30 Ma for Guatapuri and Callao (Table 7, Figure 17). A right-lateral skew in the majority of samples

reflects condensed values of cooling ages below the median, suggesting a general tendency to find younger ages. On the other hand, the central tendency of measured AHe data are 16.5, 21.6 and 21.0 Ma for Ranchería, Badillo and Guatapurí catchments, respectively (Table 7, Figure 17).

Boxplots corresponding to modeled AFT ages of the model A have a central tendency between 55 and 62 Ma and do not reproduce ages younger than ca. 43Ma (Figure 14), evidencing a misfit with measured data. Model B exhibit a better fit, because their central tendencies and their 95% confidence intervals are closer to those of the measured cooling ages ranging between 29-36 Ma. Model B presents an even better fit in the AHe data, with central tendencies of 18.7,19.7 and 21.2 Ma for Ranchería, Badillo and Guatapurí catchments, respectively (Table 7, Figure 17).

Table 6. Descriptive statistical parameters associated to boxplot diagrams.

Type of data	Min.	1st. Qu	Medi an	3 rd .Q u	Max.	Medi a	Outliers	n	95% Conf.
AFT cooling ages									
Rancheria									
Measured	11.0	32.6	44.4	59.3	75.1	45.0	0	64	39.1-49.7
Model A	44.1	49.7	54.6	57.7	61.8	53.8	0	80	53.2-56.0
Model B	29.0	30.7	32.3	36.1	43.4	34.6	54.4,50.4,50 .0,49.0, 46.6,46.6	80	31.4-33.3
Cesar									
Measured	4.6	13.5	21.3	40.1	74.9	27.2	0	61	15.9-26.6
Model A	56.2	58.0	59.4	60.7	62.4	59.3	0	57	58.9-60.0
Model B	28.6	30.0	31.5	32.6	35.8	31.4	37.4	57	30.9-32.0
Badillo									
Measured	19.4	33.6	45.3	56.7	73.6	45.6	0	54	40.3-50.2
Model A	53.0	56.8	58.2	59.5	62.6	58.2	65.6,64.3,52 .6	12	57.8-58.6
Model B	28.5	31.4	34.6	39.2	50.7	35.9	56.3,56.1	12	33.5-35.7
Guatapuri									
Measured	7.2	16.5	25.6	36.1	64.9	29.1	73.7,72.9,70 .9,69.5	90	22.3-28.8
Model A	49.9	56.2	58.5	60.6	64.6	58.4	0	20	58.0-59.0
Model B	28.3	32.8	36.5	44.2	57.0	39.0	69.8,67.8,64 .9,64.5	20	35.2-37.7
								7	

Type of data	Min.	1st. Qu	Medi an	3 rd .Q u	Max.	Medi a	Outliers	n	95% Conf.
Callao									
Measured	3.4	20.2	28.3	44.1	73.8	32.7	0	66	23.7-32.9
Model A	61.1	61.5	61.8	62.5	63.8	62.2	66.2,64.3	64	61.6-62.0
Model B	28.1	28.3	29.2	31.9	36.3	31.0	42.3,42.3,41 6,39.9,39.3, 38.6,37.5	64	28.5-29.9
Oriente									
Measured	2.8	10.2	20.7	36.9	65.4	25.0	0	64	15.4-26.0
Model A	61.0	61.4	62.0	62.7	63.7	62.1	0	43	61.7-62.3
Model B	28.2	29.7	31.4	33.8	39.3	32.2	0	43	30.4-32.4
Marinagol									
a									
Measured	6.7	13.6	20.9	36.0	67.1	27.6	75.4	82	17.0-24.8
Model A	60.6	61.3	61.9	62.9	64.9	62.2	66.4	29	61.4-62.3
Model B	28.0	29.3	31.1	33.0	38.0	31.4	0	29	30.0-32.2
Diluvio									
Measured	2.0	12.0	22.8	32.5	60.5	25.0	68.0,64.8,64 .0	70	18.9-26.6
Model A	57.8	59.7	60.8	61.5	62.7	60.6	0	66	60.5-61.2
Model B	28.0	30.0	31.0	32.4	35.6	31.3	0	66	30.6-31.5
AHe cooling ages									
Rancheria									
Measured	8.3	14.0	16.5	18.5	25.0	16.4	31.1,6.3	27	15.2-17.9
Model A	21.1	25.0	27.9	33.7	46.6	30.3	51.4,49.5,48 .2	80	26.4-29.5
Model B	16.3	17.5	18.8	21.2	25.3	20.1	34.0,30.8,30 .3,29.7 28.9,27.3	80	18.1-19.4
Badillo									
Measured	14.0	18.0	21.6	24.6	30.7	23.0	70.8	27	19.6-23.5
Model A	25.6	31.9	35.8	40.8	53.1	37.2	61.6,58.8,56 .4,55.0	12 3	34.5-37.1
Model B	16.1	17.7	19.7	22.9	29.2	20.7	35.4,34.0,31 .2	12 3	18.9-20.4
Guatapuri									
Measured	8.8	18.4	21.0	25.2	33.6	23.8	52.8,50.7,41 .4,7.35	27	19.0-23.1
Model A	24.3	32.7	36.8	46.0	60.6	39.4	0	20 9	35.3-38.2
Model B	15.6	18.2	21.2	25.8	36.5	22.5	40.7,39.0	20 9	20.3-22.0

Our results illustrate that Model B better simulate the measured data set. However, must be improve to reproduce a wider range of younger and older cooling ages as in the measured ages' spectrum. A potential explanation for such pattern involves the difficulty of including multiple kinetic characteristics of the thermochronometers (chlorine content or grain solubility (Dpar) in AFT, and radiation damage to the AHe) in a single Pecube model.

Exhumation rates derived from the 3D thermokinematic modeling (Figure 18) are similar to those derived in the 1D assessment based on the calculated exhumation depths and the youngest age peaks of the age distributions. We consider the 3-D derived rates a reliable assessment, as they are based on plausible assumptions like curved and time-variant isotherms. In spite of this, the spatial relationships reproduce well the nonuniform exhumation rates required to explain the distribution of previous bedrock data and the new detrital ages.

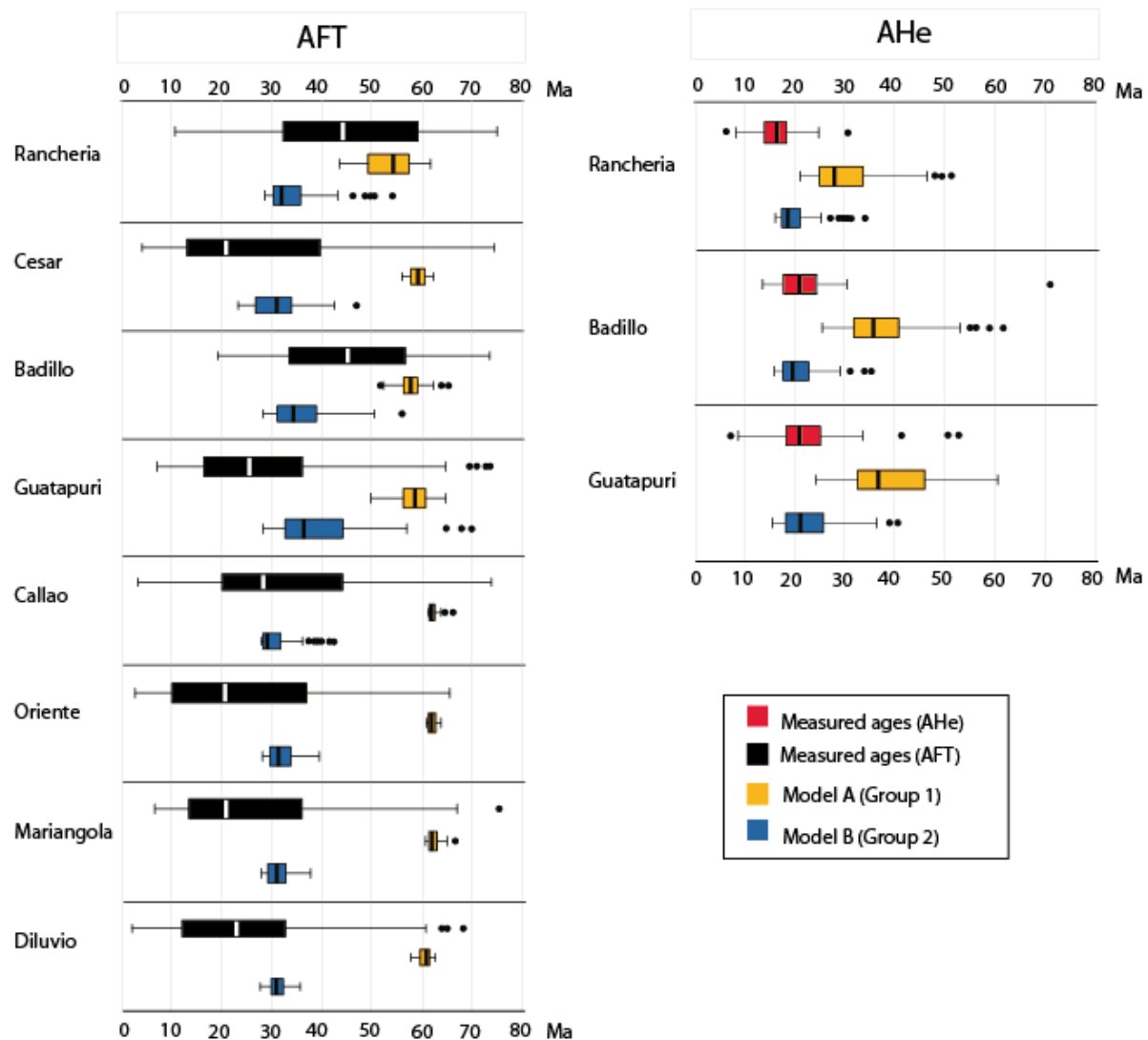


Figure 17. Comparison of boxplot diagrams corresponding to measured and modeled detrital cooling ages. Bold black lines represent the central tendency and colored boxes the interquartile range and thin black lines the 95% confidence interval of each age distribution

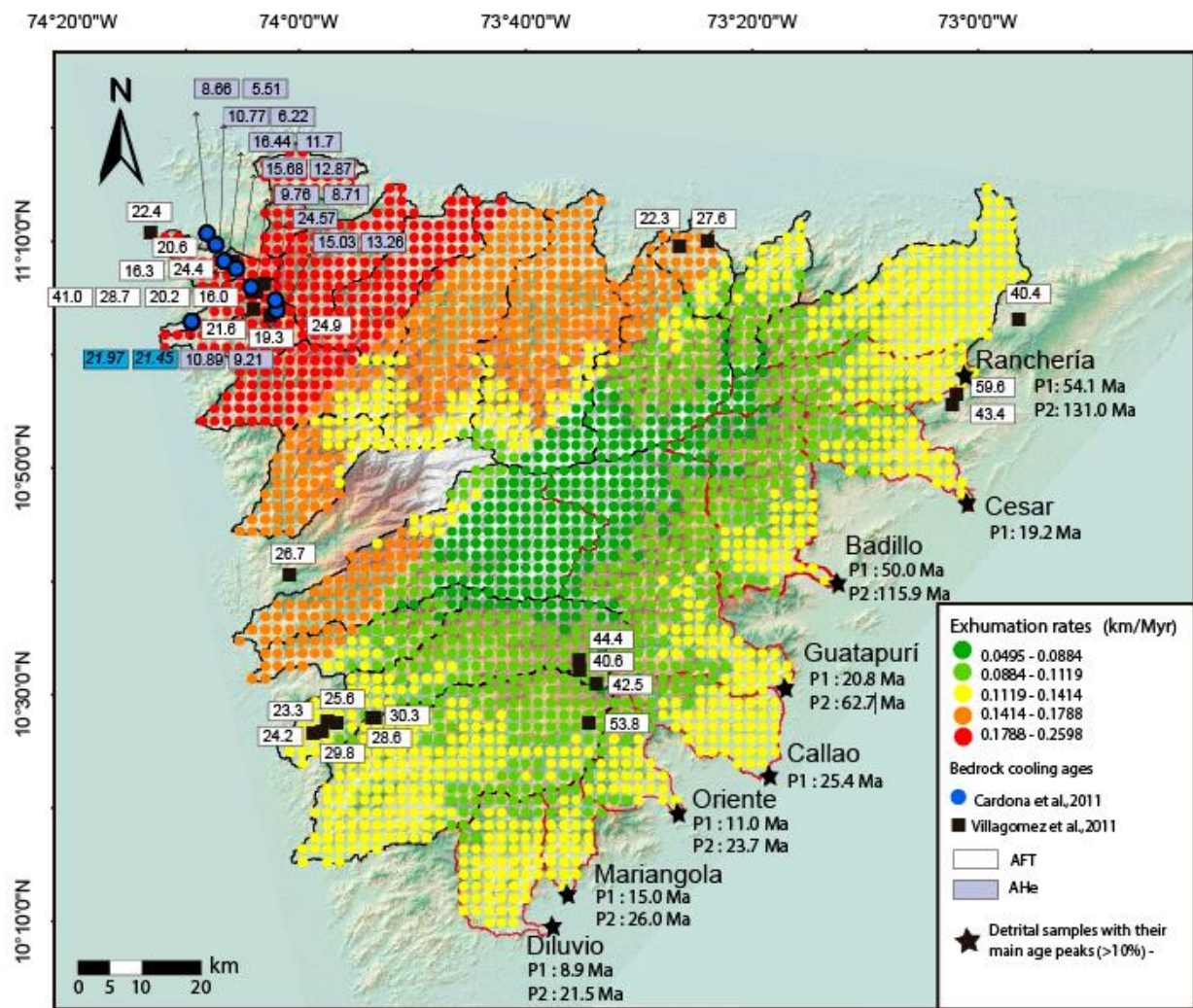


Figure 18. Exhumation rates derived from data set of the model B, corresponding to the group 2 of models conformed by a set of four vertical faults

8. Discussion

Our new detrital thermochronology data revealed three Cenozoic exhumation pulses in the eastern side of the Santa Marta massif: an early pulse during the Paleocene-Eocene (60-45 Ma), a subsequent episode in late Oligocene-Miocene (25-20 Ma), and a late pulse during the middle Miocene (16-10 Ma). Rather than a spatially homogeneous distribution of exhumation patterns, the data document an earlier Paleocene-early Eocene episode that is captured in the northern catchments and a younger middle Miocene pulse that affected the southeastern region.

Published bedrock data (Villagomez et al., 2011b, Cardona et al., 2011b) exhibit an overall asymmetric pattern of exhumation, with younger ages at the northwestern corner and older ones to eastern side. For the purpose of simulating the asymmetrical pattern of exhumation in the massif, thermokinematic models were built with a geometric arrangement that impose a gradient in the velocity field, with faster displacement in the northwest and slower to the east, during a period of tectonic activity spanning 65 My to present. The comparisons between predicted and either bedrock or detrital measured ages yield reasonable fits, particularly for the AHe data. Whilst suitable velocities to reproduce AHe ages are higher than 0.2 km/my, better fits for AFT are obtained with lower velocities. Such differences suggest nonuniform exhumation rates in shallow crustal levels (5-2 km), likely associated to an acceleration at the Miocene.

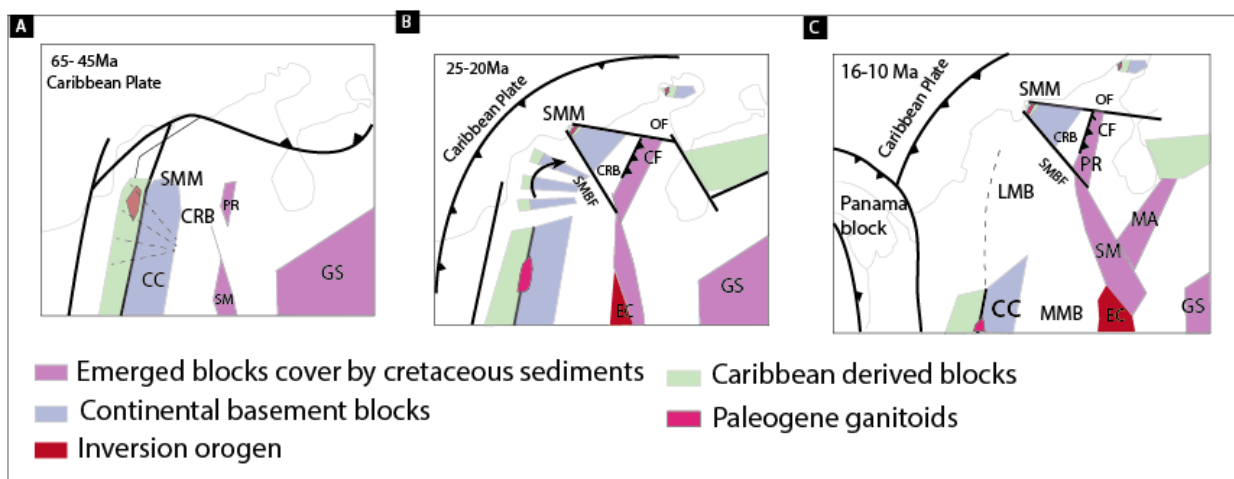


Figure 19. Oversimplified paleogeography of emerged blocks in the Cenozoic for northern Colombia. (Modified after Escalona and Mann 2012, Ayala et al., (2012))

Comparisons between predicted and measured bedrock ages support that the exhumation in the Santa Marta massif can be controlled either by rigid block or discrete blocks behavior. However, when predicted and measured detrital cooling ages of the eastern catchments are compared, the model that include four vertical faults yield better fits.

Paleocene-Eocene (65-45Ma).

A Permian-Triassic basement has been identified based on zircon U-Pb geochronology for regions in the northern Andes including the Central Cordillera, the Santa Marta massif and the basement of the Lower Magdalena basin (Montes et al., 2010; Cardona et al., 2010b; Mora et al., 2017, Vinasco, et al., 2006, Restrepo et al., 2011). Montes et al., (2010) proposed that this formerly contiguous belt was disrupted at the Late Eocene by clock-wise rotation of the Santa Marta massif, reconciling contrasting structural regimes in its boundary basins, extensional in the trailing edge along the lower Magdalena basin and compressional in leading edge at the Cesar-Ranchería basin (Figure 19A).

Our detrital cooling ages document an early pulse of exhumation at 65-45 Ma, in agreement with previous bedrock data (Villagomez et al., 2011b), which is concentrated to the northeastern side of the range. Such exhumation pulse took place when the Central Cordillera and the Santa Marta massif remained as a contiguous belt. For this period, the continental margin was subject to accretion of oceanic crustal blocks associated to the Caribbean Plate and continental magmatism.

The Sierra Nevada de Santa Marta has a geometry of a southeastwards tilted monocline with massive exhumation of up 15-19 km since Eocene (Cardona et al., 2011b) at the northwestern corner that gradually diminishes toward the Cesar-Ranchería basin (Villagomez et al., 2011b), where up to 3km of subsidence occurred in a similar timeframe. Such geometry is reminiscent to that of the Central Cordillera, where map patterns (Gómez et al., 2003) and seismic reflection data (Gómez et al., 2005, Parra et al., 2012) reveal progressive onlap of Cenozoic units from the Middle Magdalena basin onto the Central Cordillera basement. Montes et al. (2005b) proposed an eastward tilting of the crust that can explain the coeval early exhumation of the Santa Marta Massif and subsidence in the structurally continuous Cesar-Ranchería basin.

At this period, a pre-Eocene uplift of the western margin of the Cesar-Ranchería basin is recorded in the locally unconformable contact between the Paleocene strata (Cerrejón and the Eocene

Palmito formations) in the Cesar subbasin, suggesting that mild deformation took place (Montes et al., 2010). A similar pattern between the laterally equivalent Paleocene Los Cuervos and Eocene La Loma formations has been reported farther to the south in the Rancheria sub-basin (Ayala 2009). Similarly, at the Maracaibo Lake an unconformity and in the eastern flank of the Perijá range, were documented unconformities at 53 Ma and 45 Ma respectively (Kellogg et al., 1984).

Oligocene-Miocene (25-20)

Contrary to the pattern of post-Eocene denudation focused in areas close to the Santa Marta Bucaramanga fault described by Villagomez et al., (2011b), we observed that post-Eocene cooling ages are widely distributed along the range's eastern flank. At this time, it has been inferred that the emplacement of the Cerrejón thrust took place as result of the shortening imposed by the Santa Marta massif, which is correlated with synorogenic strata in the eastern flank of the Perijá range (Montes et al., 2010). Rather than a localized exhumation during the Oligocene-Miocene, the presence of this pulse in both, the Santa Marta massif and the Perijá range (Shagam et al., 1984), suggest a regional phase of exhumation. The absence of sedimentary record of this age in the Cesar-Rancheria basin attests to ongoing deformation in this area.

In this sense, the Oligocene-Miocene exhumation pulse would be a response of a collisional interaction between the basement of the already rotated Santa Marta massif and the basement of the Perijá range (Figure 19 B). The basement of the Santa Marta massif presents a higher density and lower magnetic susceptibility in comparison with the upper crust of the Perijá range and the Maracaibo basin, suggesting major crustal boundaries between them (Sanchez and Mann et al., 2015), and would have been formed in this time period.

Middle Miocene (10-16Ma)

Previous bedrock thermochronological data from the northwestern corner of the massif show the youngest AFT age of 16Ma (Villagomez et al., 2011b). In this study, we obtained similar ages, spanning 16-10 Ma in detrital data from modern sand restricted to the southwestern catchments. An AFT detrital sample analyzed in the Manaure River, located to the western flank of the Perijá range, yield an age peak of 11 Ma, suggesting a possible correlation with this same cooling event. We interpret that this pulse of exhumation should represent an episode of eastward migration of contractional deformation toward the Perijá range. Scarce Miocene stratigraphic record in the

Cesar-Rancheria basin further support a period of general uplift involving the Santa Marta massif, Cesar-Rancheria basin and Perijá range. However, the fact that the main peaks of this period are concentrated to the southeastern catchments, allow us to infer a possible influence of the Santa Marta Bucaramanga fault as the trigger of exhumation.

A pulse of exhumation promoted by displacement along this fault also explains the asymmetrical distribution of the exhumation in the marginal basins (Piraquive et al., 2017), where for the Miocene, higher rates are located in the western Aracataca region that is adjacent to the fault, whilst lower ones characterize the Palomino region to the north.

Based on this, the Santa Marta-Bucaramanga fault could be re-activated in the middle Miocene as a reverse, high-angle fault, following its former normal kinematics during the Oligocene (Villamil, 1999, Echeverri et al., 2016). Deformational features identified in subsurface mapping in the Cesar-Rancheria basin have been interpreted as imposed by the contractional reactivation of the Santa Mara Bucaramanga fault during the Neogene (Sanchez and Mann, 2015).

Our results from thermokinematic modeling support that exhumation of the Santa Marta massif at least along the eastern sector results from deformation accommodated along multiple faults.

Ingeominas., (2007) identified for the southwest corner of the range a structural trend define by ~E-W striking transcurrent faults with horstail terminations. Such faults could have accommodated the middle Miocene exhumation recorded in the southwestern catchments. However, Villagomez et al., (2011b), presented thermal models for two samples located nearby, each one from a different structural domains across such transversal faults (SN39-SN35), which yield thermal paths characterized by a rapid cooling in the Paleocene and subsequent slower rates of cooling. Such a pattern reflect that early-middle Miocene exhumation respond more likely to a more regional mechanism and not to differential uplift across such transversal faults.. Exhumation pulses recorded in the Santa Marta massif and the Perijá range until middle Miocene, together with absence of a continuous stratigraphic record in the Cesar Rancheria basin, support a regional character of the mechanism promoting the rise of both ranges. Independent mechanisms driving the differential rise of them would began to operate after middle Miocene and yielded differential responses to exhumation as is reflected in their current topography. In this sense, ongoing studies (Parra et al.,

2017) considering estimation of denudation in a more recent time framework provide valuable information about recent uplift patterns.

Conclusions

Detrital thermochronology allow establishing an episodic uplift of the Santa Marta Massif comprising the Cenozoic orogeny. A Paleocene-Eocene pulse related to the eastward tilting of a former continuous belt that included the Central Cordillera and Santa Marta massif, a Late Oligocene-Miocene related to the opening of the Lower Magdalena Basin , and the more recent pulse detected for eastern side during the Middle Miocene possibly related to a reactivation of the Santa Marta Bucaramanga fault. Thermokinematic modelling reproduce an asymmetric pattern of integrated exhumation rates since 65 Ma to present. From the modelling is suggested in northwestern corner exhumation rates of 0.26 -0.18 km/My similar to an exhumation rate derived from the geobarometry of the emplacement of the Santa Marta batholith (~ 0.3 km/My).. At the eastern side of the massif were obtained exhumation rates of 0.05-0.15 km/My that are close to the rates derived from the 1D analysis for samples with available AFT and AHe data (Ranchería, Badillo and Guatapurí). Correlations between the log-likelihood parameter for the predict ages and the velocities impose to the model suggest an inhomogeneous exhumation in the shallow crust above the 120° C isotherm. Whilst AFT system yield better fits with velocities below 2.0 km/My, the AHe require velocities 2 km /My up. Such pattern suggests and acceleration of the exhumation during the Miocene.

Further parameters as growing of topography and multiple time intervals for the tectonic scenario of the modelling would improve the fit between predicted and measured ages. However, parameters considered here provide a good baseline of the exhumation rates that have been present in the Santa Marta massif.

9. Bibliography

ANH, 2010, Mapa de Anomalia de Bouger Total de la Republica de Colombia:Agencia Nacional de Hidrocarburos

Audemard M, F.A., 2001, Quaternary tectonics and present stress tensor of the inverted northern Falcón Basin, northwestern Venezuela: *Journal of Structural Geology*, v. 23, p. 431–453.

Audemard, F.A., Romero, G., Rendon, H., and Cano, V., 2005, Quaternary fault kinematics and stress tensors along the southern Caribbean from fault-slip data and focal mechanism solutions: *Earth-Science Reviews*, v. 69, p. 181–233.

Ayala-Calvo, C., Bayona, G., Ojeda-Marulanda, C., Cardona, a, Valencia, V., Padrón, C.E., Yoris, F., Mesa, J., and Garcia, a, 2009, Estratigrafía y procedencia de las unidades comprendidas entre el Campaniano y el Paleogeno en la subcuenca de Cesar: aportes a la evolución tectónica del área: *Geología Colombiana*, v. 34, p. 3–33.

Ayala, R.C., Bayona, G., Cardona, A., Ojeda, C., Montenegro, O.C., Montes, C., Valencia, V., and Jaramillo, C., 2012, The Paleogene synorogenic succession in the northwestern Maracaibo block: Tracking intraplate uplifts and changes in sediment delivery systems: *Journal of South American Earth Sciences*, v. 39, p. 93–111, doi: 10.1016/j.jsames.2012.04.005.

Bayona, G., Lamus-Ochoa, F., Cardona, a, Jaramillo, C., Montes, C., and Tchegliakova, N., 2007, Procesos orogénicos del Paleoceno para la Cuenca Ranchería (Guajira, Colombia) y áreas adyacentes definidos por análisis de procedencia: *Geología Colombiana*, v. 32, p. 21–46. Bayona, G., Jiménez, G., Silva, C., Cardona, A., Montes, C., Roncancio, J., and Cordani, U., 2010, Paleomagnetic data and K-Ar ages from Mesozoic units of the Santa Marta massif: A preliminary interpretation for block rotation and translations: *Journal of South American Earth Sciences*, v. 29, p. 817–831, doi: 10.1016/j.jsames.2009.10.005

Bayona, G., Montes, C., Cardona, A., Jaramillo, C., Ojeda, G., Valencia, V., and Ayala-Calvo, C., 2011, Intraplate subsidence and basin filling adjacent to an oceanic arc-continent collision: A case from the southern Caribbean-South America plate margin: *Basin Research*, v. 23, p. 403–422, doi: 10.1111/j.1365-2117.2010.00495.x.

Bayona, G., Cardona, A., Jaramillo, C., Mora, A., Montes, C., Valencia, V., Ayala, C., Montenegro, O., and Ibañez-Mejia, M., 2012, Early Paleogene magmatism in the northern Andes: Insights on the effects of Oceanic Plateau-continent convergence: *Earth and Planetary Science Letters*, v. 331–332, p. 97–111, doi: 10.1016/j.epsl.2012.03.015.

Bernal-Olaza, R., Mann, P., and Vargas, C.A., 2015, Earthquake, Tomographic, Seismic Reflection, and Gravity Evidence for a Shallowly Dipping Subduction Zone beneath the Caribbean Margin of Northwestern Colombia: Memoir 108: Petroleum Geology and Potential of the Colombian Caribbean Margin, doi: 10.1306/13531939M1083642.

Bernet, M., Brandon, M., Garver, J., Balestieri, M. L., Ventura, B., & Zattin, M. (2009). Exhuming the Alps through time: Clues from detrital zircon fission-track thermochronology. *Basin Research*, 21(6), 781-798.

Bowland, C.L., and Rosencrantz, E., 1988, Upper crustal structure of the western Colombian Basin, Caribbean Sea: *Geological Society of America Bulletin*, v. 100, p. 534–546.

Braun, J. (2003). Pecube: A new finite-element code to solve the 3D heat transport equation including the effects of a time-varying, finite amplitude surface topography. *Computers & Geosciences*, 29(6), 787-794.

Braun, J., Van Der Beek, P., Valla, P., Robert, X., Herman, F., Glotzbach, C., ... & Prigent, C. (2012). Quantifying rates of landscape evolution and tectonic processes by thermochronology and numerical modeling of crustal heat transport using PECUBE. *Tectonophysics*, 524, 1-28

Burke, K., 1988, Tectonic evolution of the Caribbean: *Annual Review of Earth and Planetary Sciences*, v. 16, p. 201–230.

Bustamante, C., Cardona, A., Saldarriaga, M., Casco, A.G., Valencia, V., and Weber, M., 2009, Geología-metamorfismo de los esquistos verdes y anfibolitas pertenecientes a los Esquistos de Santa Marta, Sierra Nevada de Santa Marta (Colombia): ¿Registro de la colisión entre el Arco Caribe y la margen Suramericana? *Boletín de Ciencias de la Tierra*, p. 07–26.

Bustamante, A., Juliani, C., Hall, C.M., and Essene, E.J., 2011, $^{40}\text{Ar}/^{40}\text{Ar}$ ages from blueschists of the Jambaló region, Central Cordillera of Colombia: Implications on the styles of accretion in the Northern Andes: *Geologica Acta*, v. 9, p. 351–362, doi: 10.1344/105.000001697.

Caballero, V., Parra, M., Mora, A., López, C., Rojas, L.E., and Quintero, I., 2013, Factors controlling selective abandonment and reactivation in thick-skin orogens: a case study in the Magdalena Valley, Colombia: Geological Society, London, Special Publications, v. 377, p. 343–367, doi: 10.1144/SP377.4.

Caceres, H., Camacho, R., and Reyes, J., 1980, Guidebook to the Geology of the Ranchería Basin: Sociedad Colombiana de Geólogos y Geofísicos.

Campbell, C. J. (1965). The Santa Marta wrench fault of Colombia and its regional setting: Fourth Caribbean Geol. In Conf.(preprint), Trinidad.

Cardona-Molina, A.C., Cordani, U.G., and MacDonald, W.D., 2006, Tectonic correlations of pre-Mesozoic crust from the northern termination of the Colombian Andes, Caribbean region: Journal of South American Earth Sciences, v. 21, p. 337–354, doi: 10.1016/j.jsames.2006.07.009.

Cardona, A., Valencia, V., Bustamante, C., García-Casco, A., Ojeda, G., Ruiz, J., Saldarriaga, M., and Weber, M., 2010a, Tectonomagmatic setting and provenance of the Santa Marta Schists, northern Colombia: Insights on the growth and approach of Cretaceous Caribbean oceanic terranes to the South American continent: Journal of South American Earth Sciences, v. 29, p. 784–804, doi: 10.1016/j.jsames.2009.08.012.

Cardona, A., Valencia, V., Garzón, A., Montes, C., Ojeda, G., Ruiz, J., and Weber, M., 2010b, Permian to Triassic I to S-type magmatic switch in the northeast Sierra Nevada de Santa Marta and adjacent regions, Colombian Caribbean: Tectonic setting and implications within Pangea paleogeography: Journal of South American Earth Sciences, v. 29, p. 772–783, doi: 10.1016/j.jsames.2009.12.005.

Cardona, A., Valencia, V.A., Bayona, G., Duque, J., Ducea, M., Gehrels, G., Jaramillo, C., Montes, C., Ojeda, G., and Ruiz, J., 2011a, Early-subduction-related orogeny in the northern Andes: Turonian to Eocene magmatic and provenance record in the Santa Marta Massif and Rancheria Basin, northern Colombia: Terra Nova, v. 23, p. 26–34, doi: 10.1111/j.1365-3121.2010.00979.x.

Cardona, A., Valencia, V., Weber, M., Duque, J., Montes, C., Ojeda, G., Reiners, P., Domanik, K., Nicolescu, S., and Villagomez, D., 2011b, Transient cenozoic tectonic stages in the southern margin of the caribbean plate: U-Th/He thermochronological constraints from eocene plutonic

rocks in the Santa Marta massif and Serranía de Jarara, northern Colombia: *Geologica Acta*, v. 9, p. 445–466, doi: 10.1344/105.000001739.

Cardona, A., Montes, C., Ayala, C., Bustamante, C., Hoyos, N., Montenegro, O., Ojeda, C., Niño, H., Ramirez, V., Valencia, V., Rincón, D., Vervoort, J., and Zapata, S., 2012, From arc-continent collision to continuous convergence, clues from Paleogene conglomerates along the southern Caribbean-South America plate boundary: *Tectonophysics*, v. 580, p. 58–87, doi: 10.1016/j.tecto.2012.08.039.

Case, J., and MacDonald, W., 1973, Regional gravity anomalies and crustal structure in northern Colombia: *Geological Society of America Bulletin*, v. 84, p. 2905–2916.

Ceron-Abril, J.F., 2008, Crustal structure of the Colombian Caribbean Basin and margins.: PhD Thesis., p. 165.

Cordani, U.G., Cardona, A., Jimenez, D.M., Liu, D., and Nutman, A.P., 2005, Geochronology of Proterozoic basement inliers in the Colombian Andes: tectonic history of remnants of a fragmented Grenville belt: *Geological Society, London, Special Publications*, v. 246, p. 329–346, doi: 10.1144/GSL.SP.2005.246.01.13

Galbraith, R. F. (1988). Graphical display of estimates having differing standard errors. *Technometrics*, 30(3), 271-281.

Galbraith, R. F. (1990). The radial plot: graphical assessment of spread in ages. *International Journal of Radiation Applications and Instrumentation. Part D. Nuclear Tracks and Radiation Measurements*, 17(3), 207-214.

.Donelick, R. A., & Miller, D. S. (1991). Enhanced TINT fission track densities in low spontaneous track density apatites using ^{252}Cf -derived fission fragment tracks: A model and experimental observations. *International Journal of Radiation Applications and Instrumentation. Part D. Nuclear Tracks and Radiation Measurements*, 18(3), 301-307.

Donelick, R. A. (1993). U.S. Patent No. 5,267,274. Washington, DC: U.S. Patent and Trademark Office.

Donelick, R. A., O'Sullivan, P. B., & Ketcham, R. A. (2005). Apatite fission-track analysis. *Reviews in Mineralogy and Geochemistry*, 58(1), 49-94.

Duerto, L., Escalona, A., and Mann, P., 2006, Deep structure of the Mérida Andes and Sierra de Perijá mountain fronts, Maracaibo Basin, Venezuela: AAPG Bulletin, v. 90, p. 505–528, doi: 10.1306/10080505033.

Dumitru, T.A., 1993, A new computer-automated microscope stage system for fission-track analysis: Nuclear tracks and radiation measurements, v. 21, p. 575–580

Duncan, R.A., and Hargraves, R.B., 1984, Plate tectonic evolution of the Caribbean region in the mantle reference frame: Geological Society of America Memoirs, v. 162, p. 81–94.

Duque, J.F., 2010, Geocronología (U/Pb y 40Ar/39Ar) y geoquímica de los intrusivos paleógenos de la Sierra Nevada de Santa Marta y sus relaciones con la tectónica del Caribe y el arco magmático circun-Caribeño:

Duque-Caro, H., 1979, Major structural elements and evolution of northwestern Colombia: Geological and geophysical investigations of continental margins: AAPG Memoir, v. 29, p. 329–351.

Echeveri, S., Parra, M., 2016, Provenance and exhumation history of the Sierra Nevada de Santa Marta, Colombian Caribbean : The relationship between orogenic pulses and the Caribbean-South America tectonic during the Cenozoic. Thermo 2016: 15th international conference on thermochronology, Maresias (Brazil), September 2016.

Echeverri, S., Parra, M., Sobel, E., Pardo, A., Trejos, R., Vallejo, F., Patiño, A., 2017. Registro de exhumación Cenozoico de la Sierra Nevada de Santa Marta, Colombia : entendiendo la interacción entre tectónica y sedimentación a partir de datos de proveniencia y termocronología de baja temperatura. XVI congreso Colombiano de geología , Santa Marta (Colombia), Agosto 2017.

England, P., and Molnar, P., 1990, Surface uplift, uplift of rocks, and exhumation of rocks: Geology, v. 18, p. 1173–1177

Escalona, A., & Mann, P. (2011). Tectonics, basin subsidence mechanisms, and paleogeography of the Caribbean-South American plate boundary zone. *Marine and Petroleum Geology*, 28(1), 8–39.

Farley, K. A. (2000). Helium diffusion from apatite: General behavior as illustrated by Durango fluorapatite. *Journal of Geophysical Research: Solid Earth*, 105(B2), 2903-2914.

Farley, K. A. (2002). (U-Th)/He dating: Techniques, calibrations, and applications. *Reviews in Mineralogy and Geochemistry*, 47(1), 819-844.

Fleischer, R. L., & Price, P. B. (1964). Techniques for geological dating of minerals by chemical etching of fission fragment tracks. *Geochimica et Cosmochimica Acta*, 28(10-11), 1705-1714.

Fleischer, R.L., Price, P.B., and Walker, R.M., 1975, Nuclear tracks in solids: principles and applications: Univ of California Press

Flinch, J.F., and Castillo, V., 2015, Record and Constraints of the Eastward Advance of the Caribbean Plate in Northern South America:

Flowers, R.M., Ketcham, R.A., Shuster, D.L., and Farley, K.A., 2009, Apatite (U-Th)/He thermochronometry using a radiation damage accumulation and annealing model: *Geochimica et Cosmochimica Acta*, v. 73, p. 2347–2365, doi: 10.1016/j.gca.2009.01.015

Freymueller, J.T., Kellogg, J.N., and Vega, V., 1993, Plate Motions in the north Andean region: *Journal of Geophysical Research*, v. 98, p. 21853, doi: 10.1029/93JB00520.

Gautheron, C., Tassan-Got, L., Barbarand, J., & Pagel, M. (2009). Effect of alpha-damage annealing on apatite (U–Th)/He thermochronology. *Chemical Geology*, 266(3-4), 157-170.

Gleadow, A.J.W., 1981, Fission-track dating methods: what are the real alternatives? *Nuclear Tracks*, v. 5, p. 3–14.

Gómez, E., Jordan, T.E., Allmendinger, R.W., Hegarty, K., and Kelley, S., 2005, Syntectonic Cenozoic sedimentation in the northern middle Magdalena Valley Basin of Colombia and implications for exhumation of the Northern Andes: *Geological Society of America Bulletin*, v. 117, p. 547–569.

Gómez, E., Jordan, T.E., Allmendinger, R.W., Hegarty, K., Kelley, S., and Heizler, M., 2003, Controls on architecture of the late Cretaceous to Cenozoic southern middle Magdalena Valley basin, Colombia: *Geological Society of America Bulletin*, v. 115, p. 131–147.

Gómez, J., Nivia, Á, Montes, N.E., Almanza, M.F., Alcárcel, F.A. & Madrid, C.A. 2015. Notas explicativas: Mapa Geológico de Colombia. En: Gómez, J. & Almanza, M.F. (Editores),

Compilando la geología de Colombia: Una visión a 2015. Servicio Geológico Colombiano, Publicaciones Geológicas Especiales 33, p. 9–33. Bogotá

Green, P.F., Duddy, I.R., Gleadow, A.J.W., Tingate, P.R., and Laslett, G.M., 1986, Thermal annealing of fission tracks in apatite: 1. A qualitative description: Chemical Geology: Isotope Geoscience section, v. 59, p. 237–253.

Hasebe, N., Barbarand, J., Jarvis, K., Carter, A., & Hurford, A. J. (2004). Apatite fission-track chronometry using laser ablation ICP-MS. *Chemical Geology*, 207(3-4), 135-145.

Hernandez, O., and J. M. Jaramillo, 2009. Reconstrucción de la historia termal en los sectores de Luruaco y Cerro Cansona-Cuenca del Sinú-San Jacinto y el piedemonte occidental de la Serranía del Perijá entre Codazzi y La Jagua de Ibirico-cuenca Cesar-Ranchería ,Agencia Nacional de Hidrocarburos : Bogotá , Colombia,58 p.

Hernandez, Marina;Maldonado, Ivan;Gonzalez, Javier;Martinez, Hermes;Clavijo, Jairo;Reyes, G., 2003, Geologia de las planchas 25 Fundacion,32 Monterrubio y 39 El Difícil.Bogotá,Ingeominas.

Van der Hilst, R.P., and Mann, P., 1994, Tectonic implications of tomographic images of subducted lithosphere beneath northwestern South America: *Geology*, v. 22, p. 451–454, doi: 10.1130/0091-7613(1994)022<0451.

Horton, B.K., Anderson, V.J., Caballero, V., Saylor, J.E., Nie, J., Parra, M., and Mora, A., 2015, Application of detrital zircon U-Pb geochronology to surface and subsurface correlations of provenance, paleodrainage, and tectonics of the Middle Magdalena Valley Basin of Colombia: *Geosphere*, v. 11, p. 1790–1811, doi: 10.1130/GES01251.1.

House, M. A., Kohn, B. P., Farley, K. A., & Raza, A. (2002). Evaluating thermal history models for the Otway Basin, southeastern Australia, using (U-Th)/He and fission-track data from borehole apatites. *Tectonophysics*, 349(1-4), 277-295

Hurford, A.J., and Green, P.F., 1983, The zeta age calibration of fission-track dating: *Chemical Geology*, v. 41, p. 285–317

Jaramillo, C., Ochoa, D., Contreras, L., Pagani, M., Carvajal-Ortiz, H., Pratt, L.M., Krishnan, S., Cardona, A., Romero, M., and Quiroz, L., 2010, Effects of rapid global warming at the Paleocene-Eocene boundary on neotropical vegetation: *Science*, v. 330, p. 957–961.

Kafka, A.L., and Weidner, D.J., 1981, Earthquake focal mechanisms and tectonic processes along the southern boundary of the Caribbean plate: *Journal of Geophysical Research: Solid Earth*, v. 86, p. 2877–2888.

Kellogg, J.N., 1984, Cenozoic tectonic history of the Sierra de Perijá, Venezuela-Colombia, and adjacent basins: v. 162, p. 239–262, doi: 10.1130/MEM162-p239.

Kellogg, J.N., Vega, V., Stailings, T.C., Aiken, C.L.V. 1995, Tectonic development of Panama, Costa Rica, and the Colombian Andes: Constraints from Global Positioning System geodetic studies and gravity: v. 295, p. 75–90, doi: 10.1130/SPE295-p75.

Kennan, L., and Pindell, J.L., 2009, Dextral shear, terrane accretion and basin formation in the Northern Andes: best explained by interaction with a Pacific-derived Caribbean Plate? *Geological Society, London, Special Publications*, v. 328, p. 487–531, doi: 10.1144/SP328.20.

Kerr, A.C., and Tarney, J., 2005, Tectonic evolution of the Caribbean and northwestern South America: The case for accretion of two Late Cretaceous oceanic plateaus: *Geology*, v. 33, p. 269–272, doi: 10.1130/G21109.1.

Kerr, A.C., Tarney, J., Marriner, G.F., Nivia, A., Klaver, G.T., and Saunders, A.D., 1996, The geochemistry and tectonic setting of late Cretaceous Caribbean and Colombian volcanism: *Journal of South American Earth Sciences*, v. 9, p. 111–120, doi: 10.1016/0895-9811(96)00031-4.

Ketcham, R. A., Donelick, R. A., & Carlson, W. D. (1999). Variability of apatite fission-track annealing kinetics: III. Extrapolation to geological time scales. *American Mineralogist*, 84(9), 1235-1255.

Ketcham, R. A., Carter, A., Donelick, R. A., Barbarand, J., & Hurford, A. J. (2007). Improved modeling of fission-track annealing in apatite. *American Mineralogist*, 92(5-6), 799-810.

Lang, K.A., Huntington, K.W., Burmester, R., and Housen, B., 2016, Rapid exhumation of the eastern Himalayan syntaxis since the late Miocene: *Geological Society of America Bulletin*, v. 128, p. 1403–1422.

Lara, M., Cardona, A., Monsalve, G., Yarce, J., Montes, C., Valencia, V., Weber, M., De La Parra, F., Espitia, D., and López-Martínez, M., 2013, Middle Miocene near trench volcanism in northern Colombia: A record of slab tearing due to the simultaneous subduction of the Caribbean Plate under

South and Central America? *Journal of South American Earth Sciences*, v. 45, p. 24–41, doi: 10.1016/j.jsames.2012.12.006.

Laslett, G. M., Green, P. F., Duddy, I. R., & Gleadow, A. J. W. (1987). Thermal annealing of fission tracks in apatite 2. A quantitative analysis. *Chemical Geology: Isotope Geoscience Section*, 65(1), 1-13.

León, S., Cardona, A., Parra, M., Sobel, E. R., Jaramillo, J. S., Glodny, J., ... & Monsalve, G. (2017). Transition from collisional to subduction-related regimes: an example from Neogene Panama-Nazca-South-America interactions. *Tectonics*.

Mange, M. A., & Maurer, H. (2012). Heavy minerals in colour. Springer Science & Business Media.

Mantilla-pimiento, A., Jentzsch, G., Mantilla-pimiento, A., Jentzsch, G., Kley, J., and Alfonso-pava, C., 2009, Subduction Zone Geodynamics:, doi: 10.1007/978-3-540-87974-9.

Martinez R, J.I., and Hernandez, R., 1992, Evolution and drowning of the late cretaceous Venezuelan carbonate platform: *Journal of South American Earth Sciences*, v. 5, p. 197–210, doi: 10.1016/0895-9811(92)90038-Z.

Mauffret, A., and Leroy, S., 1997, Seismic stratigraphy and structure of the Caribbean igneous province: *Tectonophysics*, v. 283, p. 61–104, doi: 10.1016/S0040-1951(97)00103-0.

Miller, J.B., 1962, Tectonic trends in Sierra de Perija and adjacent parts of Venezuela and Colombia: *AAPG Bulletin*, v. 46, p. 1565–1595.

Montes, C., Hatcher Jr, R. D., & Restrepo-Pace, P. A. (2005a). Tectonic reconstruction of the northern Andean blocks: Oblique convergence and rotations derived from the kinematics of the Piedras–Girardot area, Colombia. *Tectonophysics*, 399(1-4), 221-250.

Montes, C., Bayona, G., Jaramillo, C., Ojeda, C., Molina, M., and Herrera, F., 2005b, Uplift of the Sierra Nevada de Santa Marta and subsidence in the Cesar- Rancheria valley : Rigid-beam pivot model: 6th International Symposium on Andean Geodynamics, p. 520–523.

Montes, C., Guzman, G., Bayona, G., Cardona, A., Valencia, V., and Jaramillo, C., 2010, Clockwise rotation of the Santa Marta massif and simultaneous Paleogene to Neogene deformation

of the Plato-San Jorge and Cesar-Ranchería basins: *Journal of South American Earth Sciences*, v. 29, p. 832–848, doi: 10.1016/j.jsames.2009.07.010.

Montes, C., Cardona, A., Jaramillo, C., Pardo, A., Silva, J.C., Valencia, V., Ayala, C., Pérez-Angel, L.C., Rodriguez-Parra, L.A., and Ramirez, V., 2015, Middle Miocene closure of the Central American seaway: *Science*, v. 348, p. 226–229.

Mora-Bohórquez, J.A., Ibáñez-Mejía, M., Oncken, O., de Freitas, M., Vélez, V., Mesa, A., and Serna, L., 2017, Structure and age of the Lower Magdalena Valley basin basement, northern Colombia: New reflection-seismic and U-Pb-Hf insights into the termination of the central andes against the Caribbean basin: *Journal of South American Earth Sciences*, v. 74, p. 1–26, doi: 10.1016/j.jsames.2017.01.001.

Mora, A., Parra, M., Strecker, M.R., Kammer, A., Dimaté, C., and Rodríguez, F., 2006, Cenozoic contractional reactivation of Mesozoic extensional structures in the Eastern Cordillera of Colombia: *Tectonics*, v. 25, p. 1–19, doi: 10.1029/2005TC001854.

Mora, A., Parra, M., Strecker, M.R., Sobel, E.R., Zeilinger, G., Jaramillo, C., Da Silva, S.F., and Blanco, M., 2010, The eastern foothills of the eastern cordillera of colombia: An example of multiple factors controlling structural styles and active tectonics: *Bulletin of the Geological Society of America*, v. 122, p. 1846–1864, doi: 10.1130/B30033.1.

Mora, A., Casallas, W., Ketcham, R. A., Gomez, D., Parra, M., Namson, J., ... & Ghorbal, B. (2015). Kinematic restoration of contractional basement structures using thermokinematic models: A key tool for petroleum system modeling. *AAPG Bulletin*, 99(8), 1575-1598.

Morton, A. C. (1984). Stability of detrital heavy tertiary sandstones from sea basin. *Clay minerals*, 19, 287-308.

Müller, R. D., Royer, J. Y., Cande, S. C., Roest, W. R., & Maschenkov, S. (1999). New constraints on the Late Cretaceous/Tertiary plate tectonic evolution of the Caribbean. In *Sedimentary basins of the world* (Vol. 4, pp. 33-59). Elsevier

Nie, J., Horton, B.K., Saylor, J.E., Mora, A., Mange, M., Garzione, C.N., Basu, A., Moreno, C.J., Caballero, V., and Parra, M., 2012, Integrated provenance analysis of a convergent retroarc foreland system: U-Pb ages, heavy minerals, Nd isotopes, and sandstone compositions of the

Middle Magdalena Valley basin, northern Andes, Colombia: *Earth-Science Reviews*, v. 110, p. 111–126, doi: 10.1016/j.earscirev.2011.11.002.

Pardo-Casas, F., & Molnar, P. (1987). Relative motion of the Nazca (Farallon) and South American plates since Late Cretaceous time. *Tectonics*, 6(3), 233-248.

Parra, M., Mora, A., Lopez, C., Rojas, L.E., and Horton, B.K., 2012, Detecting earliest shortening and deformation advance in thrust belt hinterlands: Example from the Colombian Andes: *Geology*, v. 40, p. 175–178, doi: 10.1130/G32519.1.

Parra, M., Mora, A., Sobel, E.R., Strecker, M.R., and González, R., 2009, Episodic orogenic front migration in the northern Andes: Constraints from low-temperature thermochronology in the Eastern Cordillera, Colombia: *Tectonics*, v. 28, doi: 10.1029/2008TC002423.

Parra, M., J.S. Echeverri, N. Perez-Consuegra, E.R. Sobel, 2016, Episodic uplift patterns of the Sierra Nevada de Santa Marta in northern Colombia, X South American Symposium on Isotope Geology (SSAGI), Puerto Vallarta (Mexico), May 20.

Parra, M., K. Gallagher, J.S. Echeverri, A.M. Patiño, 2017, Cenozoic exhumation patterns of the Sierra Nevada de Santa Marta, northern Colombia, through bayesian modeling of detrital thermochronometric data, EGU General Assembly Vienna (Austria), April 2017.

Pennington, W.D., 1981, the proposed Andes: v. 86, p. 10753–10770.

Pilger, R. H. (1984). Cenozoic plate kinematics, subduction and magmatism: South American Andes. *Journal of the Geological Society*, 141(5), 793-802

Pindell, J. L. BArrett, sF (1990). Geological evolution of the Caribbean region; a plate tectonic perspective. *The Geology of North America, Volume H, The Caribbean Region: The Geological Society of America*, 405-432.

Pindell, J., Kennan, L., Maresch, W. V, Stanek, K.-P., Draper, G., and Higgs, R., 2005, Plate-kinematics and crustal dynamics of circum-Caribbean arc-continent interactions: Tectonic controls on basin development in Proto-Caribbean margins: *Geological Society of America Special Papers*, v. 394, p. 7–52.

Piraquive, A., Pinzón, E., Kammer, A., Bernet, M., and Von Quadt, A., 2017, Early Neogene unroofing of the Sierra Nevada de Santa Marta, as determined from detrital geothermochronology and the petrology of clastic basin sediments: , p. 1–26, doi: 10.1130/B31676.1.

Price, P.B., and Walker, R.M., 1963, Fossil tracks of charged particles in mica and the age of minerals: *Journal of Geophysical Research*, v. 68, p. 4847–4862

Reiners, P.W., and Brandon, M.T., 2006, Using thermochronology to understand orogenic erosion: *Annu. Rev. Earth Planet. Sci.*, v. 34, p. 419–466.

Restrepo, J.J., Ordóñez-Carmona, O., Armstrong, R., and Pimentel, M.M., 2011, Triassic metamorphism in the northern part of the Tahamí Terrane of the central cordillera of Colombia: *Journal of South American Earth Sciences*, v. 32, p. 497–507, doi: 10.1016/j.jsames.2011.04.009.

Restrepo-Moreno, S. A., Foster, D. A., Stockli, D. F., & Parra-Sánchez, L. N. (2009). Long-term erosion and exhumation of the “Altiplano Antioqueño”, Northern Andes (Colombia) from apatite (U-Th)/He thermochronology. *Earth and Planetary Science Letters*, 278(1-2), 1-12.

Rincón, D.A., Arenas, J.E., Cuartas, C.H., Cárdenas, A.L., Molinares, C.E., Caicedo, C., and Jaramillo, C., 2007, Eocene-Pliocene planktonic foraminifera biostratigraphy from the continental margin of the southwest Caribbean:

Rosencrantz, E., Ross, M.I., and Sclater, J.G., 1988, Age and spreading history of the Cayman Trough as determined from depth, heat flow, and magnetic anomalies: *Journal of Geophysical Research: Solid Earth*, v. 93, p. 2141–2157.

Salazar, C.A., Bustamante, C., and Archanjo, C.J., 2016, Magnetic fabric (AMS, AAR) of the Santa Marta batholith (northern Colombia) and the shear deformation along the Caribbean Plate margin: *Journal of South American Earth Sciences*, v. 70, p. 55–68, doi: 10.1016/j.jsames.2016.04.011.

Sanchez, J., and Mann, P., 2015, Integrated Structural and Basinal Analysis of the Cesar–Rancheria Basin, Colombia: Implications for its Tectonic History and Petroleum Systems: Memoir 108: Petroleum Geology and Potential of the Colombian Caribbean Margin, doi: 10.1306/13531945M1083648.

Sarmiento-Rojas, L. F., Van Wess, J. D., & Cloetingh, S. (2006). Mesozoic transtensional basin history of the Eastern Cordillera, Colombian Andes: Inferences from tectonic models. *Journal of South American Earth Sciences*, 21(4), 383-411.

Saylor, J.E., Stockli, D.F., Horton, B.K., Nie, J., and Mora, A., 2012, Discriminating rapid exhumation from syndepositional volcanism using detrital zircon double dating: Implications for the tectonic history of the Eastern Cordillera, Colombia: *Bulletin of the Geological Society of America*, v. 124, p. 762–779, doi: 10.1130/B30534.1.

Shagam, R., Kohn, B. P., Banks, P. O., Dasch, L. E., Vargas, R., Rodriguez, G. I., & Pimentel, N. (1984). Tectonic implications of Cretaceous-Pliocene fission-track ages from rocks of the circum-Maracaibo Basin region of western Venezuela and eastern Colombia. *Geological Society of America Memoirs*, 162, 385-412.

Shuster, D.L., Flowers, R.M., and Farley, K.A., 2006, The influence of natural radiation damage on helium diffusion kinetics in apatite: *Earth and Planetary Science Letters*, v. 249, p. 148–161, doi: 10.1016/j.epsl.2006.07.028

Silva, A., Mora, A., Caballero, V., Rodriguez, G., Ruiz, C., Moreno, N., ... & Quintero, I. (2013). Basin compartmentalization and drainage evolution during rift inversion: Evidence from the Eastern Cordillera of Colombia. *Geological Society, London, Special Publications*, 377, SP377-15.

Sinton, C.W., Duncan, R. a., Storey, M., Lewis, J., and Estrada, J.J., 1998, An oceanic flood basalt province within the Caribbean plate: *Earth and Planetary Science Letters*, v. 155, p. 221–235, doi: 10.1016/S0012-821X(97)00214-8.

Spikings, R.A., Winkler, W., Hughes, R.A., and Handler, R., 2005, Thermochronology of allochthonous terranes in Ecuador: Unravelling the accretionary and post-accretionary history of the Northern Andes: *Tectonophysics*, v. 399, p. 195–220.

Spikings, R. A., Crowhurst, P. V., Winkler, W., & Villagomez, D. (2010). Syn-and post-accretionary cooling history of the Ecuadorian Andes constrained by their in-situ and detrital thermochronometric record. *Journal of South American Earth Sciences*, 30(3), 121-133

Stockli, D.F., 2005, Application of low-temperature thermochronometry to extensional tectonic settings: *Reviews in Mineralogy and Geochemistry*, v. 58, p. 411–448

Taboada, A., and Rivera, L.A., 2000, Geodynamics of the northern Andes': *Tectonics*, v. 19, p. 787–813.

Tagami, T., & O'Sullivan, P. B. (2005). Fundamentals of fission-track thermochronology. *Reviews in Mineralogy and Geochemistry*, 58(1), 19-47.

Thompson, P.M.E., Kempton, P.D., White, R. V., Kerr, A.C., Tarney, J., Saunders, A.D., Fitton, J.G., and McBirney, A., 2004, Hf-Nd isotope constraints on the origin of the Cretaceous Caribbean plateau and its relationship to the Galápagos plume: *Earth and Planetary Science Letters*, v. 217, p. 59–75, doi: 10.1016/S0012-821X(03)00542-9.

Trenkamp, R., Kellogg, J.N., Freymueller, J.T., and Mora, H.P., 2002, Wide plate margin deformation, southern Central America and northwestern South America, CASA GPS observations: *Journal of South American Earth Sciences*, v. 15, p. 157–171, doi: 10.1016/S0895-9811(02)00018-4.

Tschanz, Charles M., Jimeno, Andres, Cruz, J., 1969, Geology of the Sierra Nevada de Santa Marta Area, Colombia.:

Tschanz, C.M., Marvin, R.F., Cruz, J., Mehnert, H., and Cebulla, G., 1974, Geologic Evolution of the Sierra Nevada de Santa Marta, Northeastern Colombia: *Geological Society of America Bulletin*, v. 85, p. 273–284.

Vallejo, C., Spikings, R.A., Luzieux, L., Winkler, W., Chew, D., and Page, L., 2006, The early interaction between the Caribbean Plateau and the NW South American Plate: *Terra Nova*, v. 18, p. 264–269, doi: 10.1111/j.1365-3121.2006.00688.x.

Vermeesch, P. (2012). On the visualisation of detrital age distributions. *Chemical Geology*, 312, 190-194.

Villagómez, D., Spikings, R., Magna, T., Kammer, A., Winkler, W., and Beltrán, A., 2011a, Geochronology, geochemistry and tectonic evolution of the Western and Central cordilleras of Colombia: *Lithos*, v. 125, p. 875–896, doi: 10.1016/j.lithos.2011.05.003.

Villagómez, D., Spikings, R., Mora, A., Guzmán, G., Ojeda, G., Cortés, E., and Van Der Lelij, R., 2011b, Vertical tectonics at a continental crust-oceanic plateau plate boundary zone: Fission track thermochronology of the Sierra Nevada de Santa Marta, Colombia: *Tectonics*, v. 30, doi: 10.1029/2010TC002835.

Villagómez, D., and Spikings, R., 2013, Thermochronology and tectonics of the Central and Western Cordilleras of Colombia: Early Cretaceous-Tertiary evolution of the Northern Andes: *Lithos*, v. 160–161, p. 228–249, doi: 10.1016/j.lithos.2012.12.008.

Villamil, T., and Pindell, J.L., 1998, Mesozoic paleogeographic evolution of northern South America: Foundations for sequence stratigraphic studies in passive margin strata deposited during non-glacial times:

Vinasco, C.J., Cordani, U.G., González, H., Weber, M., and Pelaez, C., 2006, Geochronological, isotopic, and geochemical data from Permo-Triassic granitic gneisses and granitoids of the Colombian Central Andes: *Journal of South American Earth Sciences*, v. 21, p. 355–371, doi: 10.1016/j.jsames.2006.07.007.

Wagner, L.S., Jaramillo, J.S., Ramírez-Hoyos, L.F., Monsalve, G., Cardona, A., and Becker, T.W., 2017, Transient slab flattening beneath Colombia: *Geophysical Research Letters*, v. 44, p. 6616–6623, doi: 10.1002/2017GL073981.

Weber, M.B.I., Cardona, A., Paniagua, F., Cordani, U., Sepúlveda, L., and Wilson, R., 2009, The Cabo de la Vela Mafic-Ultramafic Complex, Northeastern Colombian Caribbean region: a record of multistage evolution of a Late Cretaceous intra-oceanic arc: *Geological Society, London, Special Publications*, v. 328, p. 549–568, doi: 10.1144/SP328.22.

Weber, M., Cardona, A., Valencia, V., García-Casco, A., Tobón, M., and Zapata, S., 2010, U/Pb detrital zircon provenance from late cretaceous metamorphic units of the Guajira Peninsula, Colombia: Tectonic implications on the collision between the Caribbean arc and the South American margin: *Journal of South American Earth Sciences*, v. 29, p. 805–816, doi: 10.1016/j.jsames.2009.10.004.

Wolf, R.A., Farley, K.A., and Silver, L.T., 1996, Helium diffusion and low-temperature thermochronometry of apatite: *Geochimica et Cosmochimica Acta*, v. 60, p. 4231–4240, doi: 10.1016/S0016-7037(96)00192-

Wright, J.E., and Wyld, S.J., 2011, Late Cretaceous subduction initiation on the eastern margin of the Caribbean-Colombian Oceanic Plateau: One Great Arc of the Caribbean (?): *Geosphere*, v. 7, p. 468–493, doi: 10.1130/GES00577.1.

Zapata, S., Cardona, A., Montes, C., Valencia, V., Vervoort, J., and Reiners, P., 2014, Provenance of the Eocene Soebi Blanco formation, Bonaire, Leeward Antilles: Correlations with post-Eocene tectonic evolution of northern South America: *Journal of South American Earth Sciences*, v. 52, p. 179–193, doi: 10.1016/j.jsames.2014.02.009.

Zeitler, P.K., Herczeg, A.L., McDougall, I., and Honda, M., 1987, U-Th-He dating of apatite: A potential thermochronometer: *Geochimica et Cosmochimica Acta*, v. 51, p. 2865–2868

Zuluaga, C., and Stowell, H., 2012, Late Cretaceous-Paleocene metamorphic evolution of the Sierra Nevada de Santa Marta: Implications for Caribbean geodynamic evolution: *Journal of South American Earth Sciences*, v. 34, p. 1–9, doi: 10.1016/j.jsames.2011.10.001.

Appendix I.

Results of apatite fission track dating

Rancheria

RhoD 997794,20

ND 14679

Zeta 335,7±6,6

Grain	Ns	RhoS (cm ²)	Ni	RhoI (cm ²)	Dpar	U ppm	FT age	1s
1	11	122959,98	39	435949,03	1,83	5,02	47,07	16,10
2	4	104329,68	13	339071,47	1,61	3,91	51,33	29,37
3	12	156494,52	44	573813,25	1,88	6,61	45,52	14,85
4	10	156494,52	24	375586,85	1,68	4,33	69,41	26,17
5	26	484387,81	29	540278,71	1,69	6,23	148,43	40,21
6	17	295600,77	33	573813,25	1,24	6,61	85,71	25,65
7	31	242566,51	51	399061,03	1,83	4,60	101,01	23,10
8	13	107075,20	42	345935,26	1,48	3,99	51,63	16,42
9	37	321683,19	143	1243262,04	1,22	14,33	43,19	8,02
10	9	156494,52	26	452095,29	1,50	5,21	57,71	22,35
11	17	380058,13	17	380058,13	1,31	4,38	165,34	56,82
12	14	273865,41	21	410798,12	1,65	4,73	110,70	38,27
13	15	213401,62	18	256081,95	1,45	2,95	138,08	48,36
14	17	295600,77	27	469483,57	1,65	5,41	104,60	32,46
15	59	512954,27	157	1364980,00	1,66	15,73	62,63	9,66
16	15	205913,85	28	384372,51	1,39	4,43	89,10	28,57
17	21	410798,12	78	1525821,60	1,55	17,59	44,93	11,09
18	12	98838,65	55	453010,46	1,72	5,22	36,44	11,64
19	16	250391,24	26	406885,76	1,43	4,69	102,25	32,56
20	45	704225,35	240	3755868,54	1,52	43,29	31,33	5,13
21	45	704225,35	170	2660406,89	1,58	30,66	44,18	7,47
22	68	760116,25	43	480661,75	1,24	5,54	259,56	50,87
23	21	469483,57	26	581265,37	1,39	6,70	133,87	39,38
24	35	608589,81	40	695531,21	1,20	8,02	144,90	33,68
25	16	250391,24	27	422535,21	1,11	4,87	98,49	31,14
26	16	357701,77	22	491839,93	1,72	5,67	120,67	39,73
27	10	223563,60	22	491839,93	1,05	5,67	75,68	28,91
28	8	125195,62	120	1877934,27	1,75	21,65	11,16	4,08
29	12	208659,36	44	765084,33	1,83	8,82	45,52	14,85
30	16	125195,62	58	453834,12	1,54	5,23	46,04	13,04
31	16	238467,84	22	327893,29	1,51	3,78	120,67	39,73
32	5	97809,08	25	489045,38	1,99	5,64	33,41	16,38
33	12	187793,43	30	469483,57	1,61	5,41	66,65	22,81
34	6	187793,43	14	438184,66	1,56	5,05	71,38	34,86
35	10	173882,80	26	452095,29	1,47	5,21	64,10	23,89
36	7	156494,52	11	245919,96	1,59	2,83	105,71	51,16
37	35	782472,61	35	782472,61	1,40	9,02	165,34	39,68

Grain	Ns	RhoS (cm²)	Ni	RhoI (cm²)	Dpar	U ppm	FT age	1s
38	6	117370,89	25	489045,38	1,19	5,64	40,07	18,24
39	13	169535,73	35	456442,36	1,25	5,26	61,91	20,15
40	21	328638,50	45	704225,35	1,36	8,12	77,69	20,60
41	25	391236,31	37	579029,73	0,93	6,67	112,18	29,14
42	5	111781,80	17	380058,13	1,51	4,38	49,07	24,99
43	13	290632,68	51	1140174,38	1,06	13,14	42,55	13,25
44	8	125195,62	41	641627,54	1,33	7,40	32,60	12,62
45	5	86941,40	26	452095,29	1,43	5,21	32,13	15,70
46	10	111781,80	25	279454,50	1,56	3,22	66,65	24,98
47	6	93896,71	42	657277,00	1,05	7,58	23,88	10,44
48	4	69553,12	30	521648,41	1,65	6,01	22,29	11,88
49	5	78247,26	26	406885,76	1,27	4,69	32,13	15,70
50	8	208659,36	25	652060,51	1,27	7,52	53,37	21,71
51	14	243435,92	34	591201,53	1,51	6,81	68,60	21,83
52	18	281690,14	25	391236,31	1,34	4,51	119,47	37,02
53	12	234741,78	21	410798,12	1,10	4,73	95,00	34,44
54	6	104329,68	73	1269344,46	1,57	14,63	13,75	5,85
55	34	295600,77	126	1095461,66	1,82	12,63	45,04	8,76
56	32	556424,97	70	1217179,62	1,63	14,03	76,11	16,32
57	24	536552,65	28	625978,09	1,58	7,22	141,98	39,61
58	23	449921,75	27	528169,01	1,31	6,09	141,11	40,15
59	10	223563,60	20	447127,21	1,17	5,15	83,20	32,27
60	13	203442,88	32	500782,47	1,48	5,77	67,68	22,31
61	6	97809,08	24	391236,31	1,52	4,51	41,73	19,07
62	5	69863,63	33	461099,93	1,29	5,31	25,33	12,17
63	30	469483,57	37	579029,73	1,35	6,67	134,38	33,14
64	34	591201,53	106	1843157,71	1,60	21,24	53,50	10,61
65	6	104329,68	24	417318,73	1,67	4,81	41,73	19,07
66	14	391236,31	50	1397272,52	2,15	16,11	46,72	14,16
67	11	191271,08	64	1112849,94	2,09	12,83	28,72	9,39
68	13	203442,88	23	359937,40	1,78	4,15	93,97	32,67
69	16	250391,24	39	610328,64	1,25	7,03	68,35	20,34
70	5	111781,80	18	402414,49	1,51	4,64	46,36	23,45
71	11	172143,97	30	469483,57	1,81	5,41	61,12	21,58
72	9	201207,24	26	581265,37	1,46	6,70	57,71	22,35
73	6	134138,16	19	424770,85	1,51	4,90	52,67	24,69
74	40	782472,61	91	1780125,20	1,21	20,52	73,20	13,97
75	6	93896,71	30	469483,57	1,27	5,41	33,41	14,96
76	39	610328,64	86	1345852,90	1,74	15,51	75,51	14,67
77	22	245919,96	62	693047,17	1,76	7,99	59,16	14,73
78	33	567507,61	35	601902,01	1,25	6,94	156,01	38,00
79	6	117370,89	12	234741,78	1,39	2,71	83,20	41,64
80	15	391236,31	17	443401,15	1,15	5,11	146,11	51,85
81	10	156494,52	38	594679,19	1,28	6,85	43,92	15,64
82	36	433369,45	48	577825,93	1,41	6,66	124,40	27,56

Grain	Ns	RhoS (cm²)	Ni	RhoI (cm²)	Dpar	U ppm	FT age	1s
83	19	424770,85	72	1609657,95	1,59	18,55	44,05	11,40
84	5	86941,40	25	434707,01	1,55	5,01	33,41	16,38
85	11	240664,41	14	306300,16	1,75	3,53	130,27	52,56
86	9	94515,48	38	399065,35	1,76	4,60	39,54	14,68
87	9	621812,35	11	759992,87	1,66	8,76	135,59	61,01
88	4	33024,28	43	355010,96	1,66	4,09	15,56	8,14
89	8	131271,50	12	196907,24	2,28	2,27	110,70	50,58
90	9	168777,64	18	337555,27	1,71	3,89	83,20	34,01
91	15	196907,24	40	525085,98	1,74	6,05	62,50	18,97
92	2	37506,14	25	468826,77	1,93	5,40	13,38	9,84
93	2	37506,14	19	356308,35	2,02	4,11	17,61	13,09
94	9	118144,35	36	472577,38	1,79	5,45	41,73	15,58
95	8	262542,99	10	328178,74	1,54	3,78	132,61	62,97
96	3	56259,21	16	300049,13	1,71	3,46	31,33	19,72
97	7	218785,83	12	375061,42	1,56	4,32	96,96	46,16
98	9	118144,35	43	564467,43	1,53	6,51	34,96	12,84
99	3	49226,81	18	295360,87	1,94	3,40	27,85	17,38
100	2	32817,87	18	295360,87	1,75	3,40	18,58	13,86

Cesar

ND 2796
RhoD 598793,86
Zeta 335,7±6,6

Grain	Ns	RhoS (cm^2)	Ni	RhoI (cm^2)	Dpar	U ppm	FT age	1s
1	1	20511,17	16	328178,74	2,56	6,30	6,28	6,47
2	4	75012,28	46	862641,26	2,46	16,57	8,73	4,56
3	2	41673,49	26	541755,38	1,93	10,41	7,73	5,67
4	11	180498,31	32	525085,98	3,13	10,08	34,46	12,08
5	18	147680,43	26	213316,18	2,08	4,10	69,21	21,30
6	11	72199,32	54	354433,04	1,81	6,81	20,44	6,78
7	9	393814,49	11	481328,82	1,94	9,24	81,71	36,80
8	2	29171,44	16	233371,55	1,78	4,48	12,55	9,42
9	5	93765,35	22	412567,56	2,38	7,92	22,80	11,31
10	5	72928,61	11	160442,94	1,67	3,08	45,52	24,59
11	6	98453,62	10	164089,37	2,83	3,15	60,02	31,04
12	8	291714,43	10	364643,04	2,83	7,00	79,91	37,97
13	6	98453,62	43	705584,29	2,44	13,55	14,01	6,12
14	8	116685,77	38	554257,43	2,44	10,65	21,12	8,24
15	13	170652,94	51	669484,63	1,93	12,86	25,57	7,97
16	26	426632,36	300	4922681,09	1,74	94,55	8,70	1,80
17	12	262542,99	43	940779,05	1,68	18,07	27,99	9,17
18	4	65635,75	48	787628,97	1,68	15,13	8,37	4,36
19	7	91890,05	39	511958,83	2,54	9,83	18,01	7,41
20	15	156275,59	60	625102,36	3,21	12,01	25,08	7,27
21	15	196907,24	85	1115807,71	2,30	21,43	17,71	4,98
22	8	116685,77	31	452157,37	2,42	8,68	25,89	10,29
23	13	243789,92	30	562592,12	1,98	10,81	43,41	14,46
24	35	459450,23	162	2126598,23	2,27	40,84	21,68	4,08
25	2	52508,60	16	420068,79	2,12	8,07	12,55	9,42
26	1	18232,15	8	145857,22	2,30	2,80	12,55	13,32
27	3	78762,90	10	262542,99	2,39	5,04	30,08	19,82
28	8	210034,39	20	525085,98	2,65	10,08	40,08	16,80
29	1	16408,94	22	360996,61	4,62	6,93	4,57	4,67
30	10	164089,37	73	1197852,40	1,63	23,01	13,75	4,65
31	7	153150,08	152	3325544,56	1,18	63,87	4,63	1,79
32	6	157525,79	34	892646,17	2,15	17,14	17,71	7,86
33	9	89503,29	12	119337,72	1,74	2,29	74,94	33,11
34	5	117206,69	18	421944,09	2,38	8,10	27,86	14,10
35	18	168777,64	138	1293961,89	2,09	24,85	13,10	3,30
36	15	328178,74	119	2603551,33	2,08	50,00	12,66	3,48
37	3	78762,90	6	157525,79	2,13	3,03	50,06	35,42
38	8	61774,82	46	355205,22	3,23	6,82	17,46	6,70
39	7	87514,33	33	412567,56	1,98	7,92	21,28	8,88
40	4	65635,75	41	672766,42	2,07	12,92	9,80	5,14

Grain	Ns	RhoS (cm^2)	Ni	RhoI (cm^2)	Dpar	U ppm	FT age	1s
41	4	125020,47	8	250040,94	2,31	4,80	50,06	30,69
42	17	185967,95	77	842325,43	2,51	16,18	22,15	5,97
43	25	364643,04	129	1881558,11	1,59	36,14	19,45	4,28
44	12	281296,06	43	1007977,56	1,80	19,36	27,99	9,17
45	2	65635,75	4	131271,50	3,10	2,52	50,06	43,37
46	11	277689,70	70	1767116,29	1,99	33,94	15,77	5,13
47	11	144398,65	60	787628,97	1,64	15,13	18,40	6,06
48	12	157525,79	89	1168316,31	2,22	22,44	13,54	4,18
49	6	46060,17	41	314744,52	1,91	6,05	14,69	6,43
50	6	145857,22	11	267404,90	1,94	5,14	54,59	27,75
51	9	246134,05	15	410223,42	2,05	7,88	60,02	25,36
52	10	172725,65	25	431814,13	2,29	8,29	40,08	15,04
53	8	131271,50	16	262542,99	2,17	5,04	50,06	21,72
54	16	300049,13	75	1406480,31	2,29	27,01	21,41	5,92
55	9	168777,64	21	393814,49	1,84	7,56	42,93	17,14
56	5	102555,86	7	143578,20	1,12	2,76	71,39	41,85
57	17	619893,17	143	5214395,52	2,02	100,15	11,94	3,08
58	11	229204,20	19	395898,16	1,75	7,60	57,93	22,00
59	19	155884,90	71	582517,26	2,41	11,19	26,84	6,97
60	6	112518,42	49	918900,47	2,40	17,65	12,30	5,33
61	12	315051,59	35	918900,47	2,09	17,65	34,37	11,53
62	4	61774,82	20	308874,11	1,76	5,93	20,07	11,01
63	5	218785,83	32	1400229,29	1,76	26,89	15,69	7,55

Badillo

ND 14679
RhoD 1005862,80
Zeta 335,7±6,6

Grain	Ns	RhoS (cm^2)	Ni	RhoI (cm^2)	Dpar	U ppm	FT age	1s
1	8	105017,20	22	288797,29	1,25	3,30	61,10	25,26
2	49	643230,33	66	866391,87	1,07	9,91	124,14	23,56
3	11	144398,65	36	472577,38	1,08	5,40	51,38	17,74
4	9	118144,35	33	433195,94	1,07	4,95	45,88	17,28
5	22	288797,29	73	958281,92	1,25	10,96	50,68	12,37
6	13	170652,94	25	328178,74	1,25	3,75	87,20	29,88
7	45	590721,73	70	918900,47	1,30	10,51	107,63	20,69
8	26	170652,94	75	492268,11	1,12	5,63	58,27	13,32
9	11	144398,65	39	511958,83	1,65	5,85	47,44	16,23
10	31	406941,64	36	472577,38	1,32	5,40	143,77	35,36
11	11	144398,65	16	210034,39	1,15	2,40	115,04	45,13
12	8	105017,20	31	406941,64	1,28	4,65	43,42	17,24
13	48	630103,18	74	971409,07	1,31	11,11	108,59	20,26
14	16	105017,20	79	518522,41	1,13	5,93	34,10	9,38
15	19	124707,92	88	577594,58	1,12	6,60	36,35	9,23
16	6	48026,16	15	120065,39	1,63	1,37	67,18	32,48
17	10	131271,50	43	564467,43	1,30	6,45	39,14	13,77
18	41	538213,13	48	630103,18	1,26	7,20	142,62	30,48
19	12	192104,63	22	352191,82	0,94	4,03	91,44	32,87
20	25	193046,32	30	231655,58	1,32	2,65	139,18	37,81
21	81	1063299,12	89	1168316,31	1,09	13,36	151,86	23,54
22	18	236288,69	33	433195,94	1,34	4,95	91,44	26,86
23	25	328178,74	75	984536,22	1,15	11,26	56,03	13,00
24	21	275670,14	71	932027,62	1,24	10,66	49,74	12,40
25	20	262542,99	28	367560,19	0,96	4,20	119,48	35,07
26	21	275670,14	26	341305,89	0,86	3,90	134,94	39,70
27	23	301924,44	37	485704,53	1,22	5,55	104,11	27,73
28	12	78762,90	58	380687,34	1,17	4,35	34,84	11,07
29	25	328178,74	51	669484,63	1,03	7,65	82,24	20,15
30	33	433195,94	55	721993,23	0,91	8,25	100,51	22,24
31	10	131271,50	44	577594,58	1,39	6,60	38,26	13,43
32	3	39381,45	6	78762,90	1,60	0,90	83,87	59,33
33	10	131271,50	61	800756,12	1,18	9,16	27,62	9,44
34	57	748247,53	105	1378350,70	1,26	15,76	91,01	15,10
35	28	367560,19	48	630103,18	1,42	7,20	97,74	23,34
36	92	635630,40	97	670175,53	0,91	7,66	158,17	23,26
37	22	481328,82	23	503207,40	1,13	5,75	159,50	47,69
38	28	367560,19	37	485704,53	1,06	5,55	126,52	31,80
39	3	39381,45	23	301924,44	1,56	3,45	21,98	13,50
40	86	1128934,86	114	1496495,05	0,97	17,11	126,12	18,21

Grain	Ns	RhoS (cm²)	Ni	RhoI (cm²)	Dpar	U ppm	FT age	1s
41	15	196907,24	44	577594,58	1,09	6,60	57,30	17,18
42	23	301924,44	71	932027,62	0,85	10,66	54,46	13,12
43	17	371935,90	37	809507,56	1,04	9,26	77,11	22,65
44	26	379228,77	33	481328,82	1,02	5,50	131,67	34,64
45	23	419339,50	63	1148625,59	1,26	13,13	61,35	15,00
46	47	616976,03	56	735120,38	0,85	8,41	140,17	27,89
47	35	567222,51	65	1053413,24	1,06	12,04	90,28	19,02
48	22	288797,29	26	341305,89	1,20	3,90	141,30	41,04
49	21	275670,14	52	682611,78	0,92	7,80	67,82	17,60
50	16	210034,39	64	840137,57	1,25	9,61	42,07	11,79
51	25	386092,63	30	463311,16	1,05	5,30	139,18	37,81
52	27	354433,04	80	1050171,97	0,89	12,01	56,73	12,68
53	7	91890,05	52	682611,78	1,05	7,80	22,69	9,15
54	25	187530,71	81	607599,49	0,96	6,95	51,90	11,93
55	12	132374,62	29	319905,33	1,31	3,66	69,49	23,90
56	9	118144,35	46	603848,88	1,09	6,90	32,95	12,03
57	27	354433,04	28	367560,19	1,33	4,20	160,78	43,50
58	48	692421,08	88	1269438,64	0,90	14,51	91,44	16,52
59	13	203158,27	31	484454,33	1,11	5,54	70,42	23,32
60	26	341305,89	28	367560,19	0,84	4,20	154,90	42,32
61	7	158431,12	42	950586,69	1,24	10,87	28,08	11,48
62	7	91890,05	19	249415,84	1,41	2,85	61,90	27,40
63	20	262542,99	140	1837800,94	0,85	21,01	24,07	5,78
64	11	144398,65	42	551340,28	1,27	6,30	44,07	14,96
65	12	157525,79	44	577594,58	1,11	6,60	45,88	14,97
66	10	145857,22	25	364643,04	1,17	4,17	67,18	25,18
67	8	105017,20	57	748247,53	1,31	8,56	23,65	8,94
68	5	65635,75	30	393814,49	1,45	4,50	28,08	13,58
69	16	210034,39	82	1076426,26	1,66	12,31	32,86	9,01
70	46	805131,84	144	2520412,72	1,13	28,82	53,71	9,17
71	7	91890,05	60	787628,97	0,89	9,01	19,67	7,87
72	48	630103,18	69	905773,32	0,79	10,36	116,39	22,02
73	3	281296,06	11	1031418,89	1,27	11,79	45,88	29,90
74	5	65635,75	29	380687,34	1,77	4,35	29,04	14,08
75	10	187530,71	17	318802,20	1,51	3,65	98,56	39,33
76	44	288797,29	324	2126598,23	1,16	24,31	22,89	3,71
77	20	262542,99	45	590721,73	1,23	6,75	74,60	20,11
78	36	472577,38	71	932027,62	1,38	10,66	85,04	17,49
79	22	412567,56	41	768875,90	0,90	8,79	89,96	23,85
80	8	164089,37	22	451245,77	1,19	5,16	61,10	25,26
81	36	675110,55	144	2700442,20	1,16	30,88	42,07	7,89
82	13	170652,94	38	498831,68	1,32	5,70	57,50	18,52
83	16	262542,99	19	311769,80	1,12	3,56	140,63	47,81
84	11	144398,65	35	459450,23	1,32	5,25	52,84	18,30
85	43	564467,43	48	630103,18	1,39	7,20	149,50	31,55

Grain	Ns	RhoS (cm^2)	Ni	RhoI (cm^2)	Dpar	U ppm	FT age	1s
86	9	187530,71	15	312551,18	1,34	3,57	100,51	42,43
87	18	236288,69	77	1010790,52	1,41	11,56	39,35	10,34
88	12	157525,79	97	1273333,51	1,39	14,56	20,85	6,40
89	26	853264,72	40	1312714,96	1,30	15,01	108,82	27,51
90	18	342447,38	35	665869,91	1,34	7,61	86,25	25,08
91	13	213316,18	14	229725,12	1,17	2,63	154,90	59,75
92	32	420068,79	35	459450,23	1,48	5,25	152,54	37,45
93	11	144398,65	17	223161,54	1,20	2,55	108,33	41,98
94	6	78762,90	24	315051,59	1,25	3,60	42,07	19,22
95	22	320885,88	25	364643,04	1,16	4,17	146,89	43,05
96	3	78762,90	14	367560,19	1,34	4,20	36,08	22,97
97	11	156955,05	23	328178,74	1,34	3,75	80,25	29,47
98	3	164089,37	7	382875,20	1,01	4,38	71,95	49,68
99	21	393814,49	49	918900,47	1,38	10,51	71,95	18,83
100	5	65635,75	18	236288,69	1,65	2,70	46,73	23,64

Guatapuri

ND 14679
RhoD 984346,53
Zeta 335,7±6,6

Grain	Ns	RhoS (cm^2)	Ni	RhoI (cm^2)	Dpar	U ppm	FT age	1s
1	3	56259,21	17	318802,20	1,67	3,72	29,09	18,23
2	18	393814,49	144	3150515,90	1,56	36,81	20,62	5,17
3	4	87514,33	26	568843,15	1,57	6,65	25,37	13,64
4	7	91890,05	16	210034,39	1,70	2,45	71,88	32,61
5	8	132933,16	40	664665,80	1,50	7,77	32,96	12,78
6	2	37506,14	6	112518,42	1,03	1,31	54,84	44,79
7	9	562592,12	71	4438226,76	1,57	51,85	20,91	7,41
8	11	253330,96	64	1473925,57	1,47	17,22	28,34	9,27
9	14	510500,26	50	1823215,22	2,03	21,30	46,10	13,97
10	12	262542,99	131	2866094,32	1,75	33,49	15,12	4,57
11	7	122520,06	9	157525,79	1,63	1,84	127,24	64,18
12	2	27066,29	21	284196,02	1,26	3,32	15,72	11,64
13	5	91160,76	40	729286,09	0,85	8,52	20,62	9,79
14	5	88696,96	29	514442,35	1,53	6,01	28,42	13,78
15	5	93765,35	27	5063329,91	1,07	5,92	30,52	14,88
16	6	328178,74	28	1531500,78	1,08	17,89	35,31	15,90
17	19	319763,90	202	3399595,15	1,37	39,72	15,52	3,74
18	3	56259,21	5	93765,35	1,20	1,10	98,38	71,88
19	6	157525,79	15	393814,49	1,97	4,60	65,75	31,79
20	10	218785,83	30	656357,48	1,51	7,67	54,84	20,06
21	10	267901,01	123	3295182,44	1,51	38,50	13,42	4,42
22	7	187530,71	13	348271,32	1,11	4,07	88,36	41,47
23	13	89817,34	72	497449,88	0,95	5,81	29,76	8,99
24	18	236288,69	52	682611,78	1,09	7,98	56,94	15,62
25	8	218785,83	11	300830,51	1,11	3,51	119,06	55,38
26	7	382875,20	10	546964,57	1,68	6,39	114,63	56,54
27	11	180498,31	42	689175,35	1,32	8,05	43,13	14,64
28	9	118144,35	20	262542,99	1,44	3,07	73,92	29,71
29	3	65635,75	20	437571,65	1,18	5,11	24,74	15,32
30	7	104420,51	66	984536,22	1,16	11,50	17,50	6,97
31	11	257854,72	21	492268,11	1,32	5,75	85,97	32,05
32	6	89503,29	136	2028741,30	1,26	23,70	7,29	3,04
33	7	153150,08	19	415693,07	1,15	4,86	60,59	26,82
34	6	262542,99	37	1619015,11	1,49	18,92	26,74	11,78
35	1	17502,87	4	70011,46	1,14	0,82	41,17	46,04
36	2	37506,14	34	637604,41	1,81	7,45	9,71	7,07
37	2	175028,66	12	1050171,97	1,41	12,27	27,48	21,00
38	18	299099,61	20	332332,90	2,13	3,88	147,01	47,87
39	11	180498,31	154	2526976,29	1,26	29,52	11,79	3,69
40	6	160740,61	20	535802,02	1,07	6,26	49,38	23,01

Grain	Ns	RhoS (cm^2)	Ni	RhoI (cm^2)	Dpar	U ppm	FT age	1s
41	6	100978,07	35	589038,76	1,57	6,88	28,26	12,50
42	29	543839,05	173	3244281,25	1,59	37,90	27,64	5,58
43	11	300830,51	109	2980956,88	1,43	34,83	16,65	5,28
44	16	656357,48	193	7917312,08	1,56	92,50	13,68	3,57
45	9	196907,24	116	2537915,58	1,13	29,65	12,81	4,44
46	23	301924,44	172	2257869,73	1,23	26,38	22,06	4,92
47	2	26254,30	20	262542,99	1,23	3,07	16,50	12,24
48	15	246134,05	157	2576203,10	1,43	30,10	15,77	4,27
49	12	262542,99	53	1159564,88	1,55	13,55	37,30	11,95
50	5	187530,71	11	412567,56	1,30	4,82	74,67	40,30
51	15	196907,24	48	630103,18	1,56	7,36	51,43	15,25
52	1	26254,30	3	78762,90	1,51	0,92	54,84	63,33
53	8	175028,66	79	1728408,03	1,62	20,19	16,71	6,21
54	3	39381,45	27	354433,04	1,38	4,14	18,33	11,16
55	8	116685,77	53	773043,25	1,51	9,03	24,89	9,46
56	4	125020,47	14	437571,65	1,66	5,11	47,03	26,68
57	24	370648,93	139	2146675,05	1,25	25,08	28,46	6,32
58	8	105017,20	70	918900,47	1,58	10,74	18,85	7,05
59	7	102100,05	11	160442,94	1,17	1,87	104,29	50,47
60	13	224543,35	72	1243624,70	1,21	14,53	29,76	8,99
61	8	105017,20	48	630103,18	1,32	7,36	27,48	10,51
62	47	964025,05	281	5763639,11	1,53	67,34	27,58	4,39
63	13	370984,66	115	3281787,39	1,58	38,34	18,65	5,47
64	4	75012,28	46	862641,26	1,57	10,08	14,35	7,49
65	1	13127,15	9	118144,35	0,94	1,38	18,33	19,33
66	19	249415,84	67	879519,02	1,22	10,28	46,68	12,17
67	20	364643,04	138	2516037,00	1,29	29,40	23,90	5,74
68	8	105017,20	67	879519,02	0,99	10,28	19,70	7,38
69	2	43757,17	8	175028,66	1,34	2,04	41,17	32,56
70	7	131271,50	12	225036,85	1,47	2,63	95,67	45,54
71	2	72928,61	14	510500,26	0,96	5,96	23,56	17,82
72	2	31255,12	20	312551,18	1,38	3,65	16,50	12,24
73	34	743871,81	334	7307446,59	1,34	85,38	16,80	3,04
74	7	306300,16	20	875143,30	1,79	10,22	57,57	25,31
75	16	840137,57	104	5460894,22	1,20	63,80	25,37	6,83
76	6	562592,12	10	937653,54	1,08	10,96	98,38	50,85
77	25	328178,74	127	1667148,00	1,25	19,48	32,44	7,13
78	1	36464,30	16	583428,87	0,95	6,82	10,32	10,64
79	13	170652,94	81	1063299,12	1,40	12,42	26,46	7,93
80	13	170652,94	112	1470240,75	1,39	17,18	19,15	5,63
81	3	57074,56	7	133173,98	2,06	1,56	70,42	48,62
82	4	150024,57	53	1987825,51	1,50	23,22	12,46	6,47
83	2	65635,75	16	525085,98	1,51	6,13	20,62	15,47
84	2	43757,17	6	131271,50	1,07	1,53	54,84	44,79
85	2	1312714,96	41	26910656,62	1,40	314,41	8,05	5,84

Grain	Ns	RhoS (cm^2)	Ni	RhoI (cm^2)	Dpar	U ppm	FT age	1s
86	2	1312714,96	10	6563574,79	1,29	76,69	32,96	25,54
87	22	1312714,96	192	11456421,44	1,36	133,85	18,90	4,27
88	6	1312714,96	58	12689577,92	1,57	148,26	17,07	7,33
89	2	1312714,96	9	5907217,31	2,01	69,02	36,61	28,63
90	3	1312714,96	4	1750286,61	1,38	20,45	122,74	93,78
91	4	1312714,96	22	7219932,26	1,78	84,35	29,97	16,30
92	13	1312714,96	77	7775311,67	1,42	90,84	27,83	8,37
93	3	1312714,96	47	20565867,66	1,51	240,28	10,54	6,28
94	8	1312714,96	127	20839349,94	1,49	243,48	10,40	3,80
95	3	1312714,96	12	5250859,83	1,78	61,35	41,17	26,59
96	4	1312714,96	18	5907217,31	1,14	69,02	36,61	20,25
97	10	1312714,96	48	6301031,79	1,57	73,62	34,33	11,96
98	1	1312714,96	11	14439864,53	1,89	168,71	15,00	15,67
99	5	1312714,96	60	15752579,48	1,56	184,05	13,75	6,41
100	6	1312714,96	64	14002292,88	1,52	163,60	15,47	6,61
101	6	1312714,96	42	9189004,70	1,12	107,36	23,56	10,29

Callao

ND 2796
RhoD 580217
Zeta 335,7±6,6

Grain	Ns	RhoS (cm ²)	Ni	RhoI (cm ²)	Dpar	U ppm	FT age	1s
1	8	218785,83	30	820446,85	2,75	16,26	25,92	10,34
2	1	32817,87	3	98453,62	1,98	1,95	32,38	37,40
3	8	214320,81	11	294691,11	1,94	5,84	70,44	32,79
4	12	157525,79	31	406941,64	1,80	8,07	37,59	12,82
5	8	262542,99	10	328178,74	2,15	6,50	77,44	36,80
6	8	164089,37	29	594823,96	2,18	11,79	26,81	10,73
7	4	291714,43	15	1093929,13	2,06	21,68	25,92	14,60
8	6	187530,71	11	343806,30	1,54	6,81	52,90	26,89
9	3	93765,35	14	437571,65	1,83	8,67	20,84	13,27
10	10	164089,37	22	360996,61	1,86	7,16	44,12	16,87
11	7	102100,05	21	306300,16	2,22	6,07	32,38	14,16
12	16	350057,32	21	459450,23	2,27	9,11	73,78	24,57
13	19	315716,26	28	465266,06	2,06	9,22	65,75	19,62
14	8	116685,77	10	145857,22	1,94	2,89	77,44	36,80
15	1	36464,30	2	72928,61	2,38	1,45	48,51	59,43
16	3	157525,79	14	735120,38	2,15	14,57	20,84	13,27
17	10	187530,71	50	937653,54	2,16	18,59	19,45	6,76
18	7	183780,09	21	551340,28	1,89	10,93	32,38	14,16
19	1	14585,72	5	72928,61	2,01	1,45	19,45	21,31
20	10	262542,99	50	1312714,96	2,39	26,02	19,45	6,76
21	4	58342,89	15	218785,83	2,63	4,34	25,92	14,60
22	1	21878,58	2	43757,17	2,08	0,87	48,51	59,43
23	2	75012,28	3	112518,42	2,01	2,23	64,60	59,00
24	4	131271,50	16	525085,98	2,38	10,41	24,30	13,60
25	9	118144,35	25	328178,74	1,90	6,50	34,97	13,63
26	8	88249,75	49	540529,69	2,60	10,71	15,88	6,07
27	7	127625,07	18	328178,74	2,27	6,50	37,76	16,85
28	7	306300,16	19	831386,14	2,47	16,48	35,78	15,85
29	1	54696,46	3	164089,37	2,08	3,25	32,38	37,40
30	4	87514,33	6	131271,50	2,41	2,60	64,60	41,74
31	2	38609,26	14	270264,84	2,48	5,36	13,90	10,51
32	13	170652,94	34	446323,09	2,30	8,85	37,13	12,15
33	8	119337,72	26	387847,60	2,05	7,69	29,90	12,11
34	5	119337,72	32	763761,43	2,02	15,14	15,20	7,32
35	4	65635,75	49	804037,91	2,69	15,94	7,95	4,14
36	5	262542,99	15	787628,97	2,24	15,61	32,38	16,75
37	2	32817,87	9	147680,43	2,13	2,93	21,61	16,90
38	5	273482,28	7	382875,20	2,14	7,59	69,19	40,56
39	3	145857,22	5	243095,36	3,17	4,82	58,17	42,51
40	1	26254,30	11	288797,29	2,73	5,72	8,85	9,24

Grain	Ns	RhoS (cm²)	Ni	RhoI (cm²)	Dpar	U ppm	FT age	1s
41	11	515709,45	22	1031418,89	1,86	20,44	48,51	17,96
42	1	26790,10	27	723332,73	2,33	14,34	3,61	3,67
43	1	36464,30	5	182321,52	2,04	3,61	19,45	21,31
44	5	328178,74	7	459450,23	2,24	9,11	69,19	40,56
45	4	69090,26	8	138180,52	2,27	2,74	48,51	29,74
46	2	32817,87	5	82044,68	1,99	1,63	38,84	32,51
47	33	433195,94	138	1811546,64	2,00	35,91	23,25	4,55
48	1	18753,07	13	243789,92	3,00	4,83	7,49	7,77
49	9	118144,35	15	196907,24	3,33	3,90	58,17	24,58
50	4	58342,89	11	160442,94	2,57	3,18	35,32	20,64
51	35	459450,23	107	1404605,00	2,24	27,84	31,78	6,25
52	59	774501,82	248	3255533,09	2,43	64,53	23,13	3,41
53	25	410223,42	104	1706529,44	2,62	33,83	23,37	5,24
54	2	32817,87	3	49226,81	1,77	0,98	64,60	59,00
55	5	82044,68	13	213316,18	2,86	4,23	37,35	19,68
56	1	26254,30	28	735120,38	2,35	14,57	3,48	3,54
57	9	295360,87	87	2855155,03	1,90	56,59	10,07	3,54
58	5	133950,51	24	642962,43	2,22	12,74	20,26	9,97
59	11	160442,94	40	583428,87	2,16	11,56	26,73	9,13
60	4	145857,22	18	656357,48	2,42	13,01	21,61	11,96
61	5	82044,68	24	393814,49	2,31	7,81	20,26	9,97
62	11	412567,56	59	2212862,36	2,23	43,86	18,13	5,98
63	6	87514,33	24	350057,32	2,44	6,94	24,30	11,11
64	1	21519,92	18	387358,51	2,03	7,68	5,41	5,56
65	5	136741,14	16	437571,65	2,38	8,67	30,36	15,58
66	13	170652,94	18	236288,69	2,35	4,68	69,96	25,53
67	9	168777,64	43	806382,05	2,24	15,98	20,35	7,48
68	2	32817,87	25	410223,42	2,14	8,13	7,79	5,73

Oriente

ND 2796
RhoD 587647,95
Zeta 335,7±6,6

Grain	Ns	RhoS (cm^2)	Ni	RhoI (cm^2)	Dpar	U ppm	FT age	1s
1	2	26254,30	45	590721,73	1,34	11,56	4,38	3,17
2	4	52508,60	44	577594,58	2,05	11,30	8,96	4,69
3	3	49226,81	40	656357,48	1,37	12,85	7,39	4,43
4	1	16408,94	35	574312,79	1,98	11,24	2,82	2,86
5	14	183780,09	58	761374,68	2,05	14,90	23,77	7,11
6	3	43757,17	8	116685,77	1,37	2,28	36,88	24,99
7	2	75012,28	12	450073,70	1,98	8,81	16,42	12,55
8	1	32817,87	3	98453,62	2,05	1,93	32,80	37,88
9	1	20836,75	13	270877,69	1,37	5,30	7,58	7,87
10	1	18232,15	11	200553,67	1,98	3,92	8,96	9,36
11	10	131271,50	80	1050171,97	2,05	20,55	12,32	4,15
12	7	170166,75	27	656357,48	1,37	12,85	25,52	10,85
13	8	164089,37	79	1620382,53	1,98	31,71	9,98	3,71
14	29	380687,34	153	2008453,88	2,05	39,31	18,67	3,82
15	4	52508,60	6	78762,90	1,37	1,54	65,42	42,27
16	7	102100,05	21	306300,16	1,98	5,99	32,80	14,34
17	2	32412,71	6	97238,14	2,42	1,90	32,80	26,79
18	3	39381,45	29	380687,34	1,75	7,45	10,20	6,19
19	1	32817,87	5	164089,37	2,16	3,21	19,70	21,58
20	8	175028,66	22	481328,82	2,28	9,42	35,77	14,80
21	2	32817,87	26	426632,36	2,33	8,35	7,58	5,57
22	3	82044,68	14	382875,20	1,97	7,49	21,10	13,44
23	6	131271,50	12	262542,99	2,09	5,14	49,13	24,60
24	18	337555,27	58	1087678,11	2,03	21,29	30,54	8,28
25	5	262542,99	9	472577,38	1,74	9,25	54,57	30,47
26	27	177216,52	69	452886,66	2,21	8,86	38,48	8,80
27	1	37506,14	9	337555,27	1,82	6,61	10,95	11,55
28	3	48619,07	7	113444,50	1,66	2,22	42,13	29,10
29	1	14585,72	13	189614,38	2,05	3,71	7,58	7,87
30	7	91890,05	63	827010,42	1,86	16,19	10,95	4,37
31	1	13127,15	20	262542,99	1,78	5,14	4,93	5,05
32	24	393814,49	88	1443986,45	1,65	28,26	26,84	6,23
33	8	105017,20	51	669484,63	2,36	13,10	15,45	5,89
34	3	39381,45	6	78762,90	2,16	1,54	49,13	34,77
35	9	147680,43	87	1427577,52	2,00	27,94	10,20	3,58
36	18	262542,99	76	1108514,85	1,89	21,69	23,32	6,15
37	7	91890,05	15	196907,24	2,13	3,85	45,87	21,03
38	2	26254,30	50	656357,48	2,36	12,85	3,94	2,85
39	3	39381,45	8	105017,20	2,16	2,06	36,88	24,99
40	5	82044,68	29	475859,17	2,12	9,31	16,98	8,24

Grain	Ns	RhoS (cm^2)	Ni	RhoI (cm^2)	Dpar	U ppm	FT age	1s
41	4	52508,60	9	118144,35	1,97	2,31	43,69	26,28
42	2	32817,87	4	65635,75	1,84	1,28	49,13	42,57
43	1	37506,14	14	525085,98	2,03	10,28	7,04	7,29
44	14	437571,65	49	1531500,78	1,88	29,97	28,12	8,56
45	4	82044,68	45	923002,70	1,97	18,06	8,76	4,58
46	6	78762,90	39	511958,83	2,35	10,02	15,16	6,66
47	13	189614,38	98	1429400,73	1,98	27,97	13,07	3,87
48	15	153833,78	75	769168,92	2,17	15,05	19,70	5,60
49	7	102100,05	73	1064757,69	2,10	20,84	9,45	3,75
50	9	118144,35	15	196907,24	1,87	3,85	58,91	24,89
51	2	26254,30	23	301924,44	2,25	5,91	8,57	6,32
52	4	32817,87	27	221520,65	2,34	4,34	14,60	7,83
53	5	81031,79	11	178269,93	2,38	3,49	44,68	24,13
54	6	60586,84	17	171662,73	1,99	3,36	34,72	16,51
55	13	142210,79	63	689175,35	1,96	13,49	20,32	6,22
56	3	98453,62	5	164089,37	2,23	3,21	58,91	43,05
57	9	328178,74	41	1495036,48	2,33	29,26	21,62	7,98
58	10	772185,27	25	1930463,17	2,17	37,78	39,33	14,76
59	3	51144,74	16	272771,94	2,14	5,34	18,47	11,63
60	3	67899,05	10	226330,17	1,84	4,43	29,52	19,45
61	16	161564,92	18	181760,53	1,87	3,56	87,09	30,02
62	2	52508,60	9	236288,69	2,70	4,62	21,88	17,12
63	6	78762,90	43	564467,43	2,43	11,05	13,75	6,00
64	6	160740,61	11	294691,11	2,22	5,77	53,58	27,23
65	2	131271,50	4	262542,99	2,94	5,14	49,13	42,57

Mariangola

ND 2796
RhoD 602509,17
Zeta 335,7±6,6

Grain	Ns	RhoS (cm^2)	Ni	RhoI (cm^2)	Dpar	U ppm	FT age	1s
1	20	262542,99	150	1969072,44	2,47	37,59	13,47	3,23
2	46	754811,10	191	3134106,96	2,22	59,82	24,31	4,05
3	1	13127,15	9	118144,35	2,06	2,26	11,23	11,84
4	15	196907,24	20	262542,99	2,40	5,01	75,41	25,84
5	7	91890,05	15	196907,24	2,49	3,76	47,02	21,56
6	5	65635,75	8	105017,20	2,84	2,00	62,90	35,90
7	2	52508,60	7	183780,09	3,09	3,51	28,83	23,13
8	6	98453,62	87	1427577,52	2,17	27,25	6,97	2,95
9	59	595770,63	73	737139,94	2,65	14,07	81,22	14,39
10	12	157525,79	93	1220824,91	2,42	23,30	13,04	4,01
11	5	65635,75	9	118144,35	2,23	2,26	55,94	31,24
12	11	144398,65	29	380687,34	2,33	7,27	38,25	13,58
13	4	52508,60	7	91890,05	3,28	1,75	57,53	36,09
14	16	150024,57	36	337555,27	2,25	6,44	44,79	13,51
15	3	56259,21	26	487579,84	2,34	9,31	11,66	7,12
16	2	52508,60	6	157525,79	2,35	3,01	33,62	27,47
17	14	255250,13	90	1640893,70	2,00	31,32	15,71	4,53
18	1	26254,30	13	341305,89	2,25	6,51	7,77	8,07
19	29	380687,34	103	1352096,41	2,23	25,81	28,41	6,02
20	22	288797,29	129	1693402,29	2,01	32,32	17,22	4,00
21	14	367560,19	30	787628,97	2,18	15,03	47,02	15,27
22	7	131271,50	37	693863,62	2,09	13,24	19,10	7,89
23	11	240664,41	69	1509622,20	1,86	28,82	16,10	5,25
24	2	65635,75	3	98453,62	1,68	1,88	67,07	61,25
25	31	406941,64	231	3032371,55	2,88	57,88	13,56	2,62
26	4	75012,28	38	712616,69	1,86	13,60	10,64	5,60
27	14	229725,12	114	1870618,81	2,30	35,71	12,41	3,53
28	40	525085,98	222	2914227,20	2,15	55,63	18,20	3,16
29	10	145857,22	36	525085,98	2,76	10,02	28,03	10,05
30	32	420068,79	162	2126598,23	2,11	40,59	19,95	3,90
31	18	262542,99	187	2727529,97	1,92	52,06	9,73	2,42
32	21	275670,14	141	1850928,09	2,13	35,33	15,04	3,54
33	20	291714,43	47	685528,92	2,11	13,09	42,89	11,51
34	6	78762,90	10	131271,50	2,15	2,51	60,39	31,23
35	1	21878,58	15	328178,74	2,08	6,26	6,74	6,96
36	15	120065,39	30	240130,78	1,73	4,58	50,37	15,99
37	14	183780,09	24	315051,59	2,26	6,01	58,72	19,81
38	6	66187,31	34	375061,42	2,24	7,16	17,82	7,91
39	5	93765,35	21	393814,49	1,71	7,52	24,03	11,98
40	1	23441,34	5	117206,69	2,41	2,24	20,19	22,13

Grain	Ns	RhoS (cm^2)	Ni	RhoI (cm^2)	Dpar	U ppm	FT age	1s
41	8	116685,77	10	145857,22	1,94	2,78	80,40	38,20
42	33	433195,94	136	1785292,34	1,82	34,08	24,49	4,80
43	5	65635,75	14	183780,09	2,09	3,51	36,02	18,79
44	7	131271,50	50	937653,54	1,98	17,90	14,14	5,72
45	14	183780,09	51	669484,63	2,14	12,78	27,70	8,39
46	20	291714,43	43	627186,04	2,32	11,97	46,87	12,75
47	33	270747,46	200	1640893,70	2,22	31,32	16,67	3,16
48	15	393814,49	55	1443986,45	2,30	27,56	27,52	8,05
49	6	97238,14	18	291714,43	2,72	5,57	33,62	15,88
50	8	150024,57	23	431320,63	2,34	8,23	35,08	14,43
51	49	357350,18	301	2195151,12	2,22	41,90	16,44	2,57
52	21	275670,14	35	459450,23	1,91	8,77	60,39	16,75
53	19	249415,84	100	1312714,96	2,28	25,06	19,19	4,83
54	10	164089,37	49	804037,91	2,43	15,35	20,61	7,17
55	50	328178,74	407	2671374,94	2,17	50,99	12,41	1,89
56	1	16408,94	12	196907,24	2,03	3,76	8,42	8,77
57	23	377405,55	250	4102234,24	2,12	78,30	9,30	2,04
58	2	26254,30	13	170652,94	2,07	3,26	15,54	11,81
59	5	32817,87	19	124707,92	2,21	2,38	26,56	13,37
60	4	187530,71	6	281296,06	2,07	5,37	67,07	43,33
61	6	30293,42	45	227200,67	1,91	4,34	13,47	5,87
62	33	309425,67	203	1903436,69	2,17	36,33	16,42	3,11
63	3	19690,72	24	157525,79	2,18	3,01	12,63	7,74
64	16	210034,39	67	879519,02	2,02	16,79	24,11	6,74
65	6	78762,90	58	761374,68	1,95	14,53	10,45	4,49
66	5	72928,61	26	379228,77	1,62	7,24	19,42	9,50
67	13	170652,94	47	616976,03	2,35	11,78	27,91	8,78
68	26	487579,84	112	2100343,93	2,39	40,09	23,43	5,14
69	14	183780,09	16	210034,39	2,04	4,01	87,89	32,25
70	4	75012,28	6	112518,42	1,83	2,15	67,07	43,33
71	12	225036,85	57	1068925,04	2,09	20,40	21,26	6,78
72	20	375061,42	153	2869219,83	2,36	54,77	13,21	3,16
73	6	218785,83	19	692821,78	1,87	13,22	31,86	14,94
74	7	153150,08	21	459450,23	1,99	8,77	33,62	14,70
75	3	49226,81	12	196907,24	2,21	3,76	25,23	16,30
76	26	341305,89	72	945154,77	1,98	18,04	36,42	8,39
77	21	137835,07	36	236288,69	2,24	4,51	58,72	16,20
78	5	131271,50	11	288797,29	2,50	5,51	45,81	24,74
79	14	183780,09	53	695738,93	2,39	13,28	26,66	8,04
80	35	459450,23	189	2481031,27	2,35	47,36	18,70	3,48
81	3	39381,45	25	328178,74	2,03	6,26	12,12	7,42
82	3	140648,03	24	1125184,25	2,07	21,48	12,63	7,74
83	26	284421,57	202	2209736,84	2,19	42,18	13,00	2,73
84	33	433195,94	205	2691065,66	1,87	51,37	16,26	3,08
85	20	328178,74	148	2428522,67	1,84	46,36	13,65	3,27

Diluvio

ND 2594
RhoD 543329,29
Zeta 335,7±6,6

Grain	Ns	RhoS (cm^2)	Ni	RhoI (cm^2)	Dpar	U ppm	FT age	1s
1	30	246134,05	127	1041967,50	2,92	22,06	21,51	4,41
2	16	350057,32	9	196907,24	2,22	4,17	160,12	66,87
3	6	100978,07	4	67318,72	2,49	1,42	135,37	87,46
4	1	16408,94	3	49226,81	3,56	1,04	30,33	35,03
5	10	267901,01	26	696542,63	2,95	14,74	34,98	13,05
6	9	337555,27	44	1650270,23	2,46	34,93	18,63	6,83
7	10	218785,83	3	65635,75	2,66	1,39	297,04	195,71
8	10	205111,71	28	574312,79	1,91	12,16	32,49	12,00
9	1	21878,58	21	459450,23	3,42	9,73	4,34	4,45
10	2	26254,30	2	26254,30	2,81	0,56	90,56	90,59
11	4	52508,60	24	315051,59	2,40	6,67	15,18	8,21
12	6	112518,42	13	243789,92	2,03	5,16	41,95	20,74
13	5	65635,75	4	52508,60	3,28	1,11	113,00	75,87
14	12	225036,85	17	318802,20	3,62	6,75	64,06	24,22
15	9	168777,64	8	150024,57	2,16	3,18	101,79	49,54
16	1	18753,07	8	150024,57	3,18	3,18	11,39	12,08
17	1	20511,17	3	61533,51	3,60	1,30	30,33	35,03
18	10	312551,18	8	250040,94	3,14	5,29	113,00	53,69
19	8	150024,57	7	131271,50	3,26	2,78	103,39	53,59
20	6	98453,62	9	147680,43	3,74	3,13	60,51	31,94
21	17	348689,91	129	2645941,09	2,56	56,01	12,01	3,12
22	6	98453,62	67	1099398,78	2,52	23,27	8,16	3,49
23	2	43757,17	24	525085,98	3,97	11,11	7,60	5,59
24	6	109392,91	21	382875,20	2,39	8,10	26,00	12,06
25	20	375061,42	36	675110,55	3,03	14,29	50,47	14,14
26	7	91890,05	19	249415,84	3,02	5,28	33,51	14,85
27	4	105017,20	8	210034,39	3,66	4,45	45,44	27,85
28	2	52508,60	7	183780,09	2,31	3,89	26,00	20,86
29	10	131271,50	71	932027,62	2,26	19,73	12,83	4,35
30	1	13127,15	15	196907,24	2,44	4,17	6,08	6,28
31	1	18753,07	19	356308,35	2,87	7,54	4,80	4,92
32	6	97238,14	16	259301,72	3,79	5,49	34,11	16,36
33	3	131271,50	5	218785,83	2,70	4,63	54,49	39,82
34	4	52508,60	12	157525,79	3,33	3,33	30,33	17,53
35	3	56259,21	8	150024,57	3,91	3,18	34,11	23,11
36	19	249415,84	90	1181443,46	1,93	25,01	19,22	4,88
37	3	39381,45	11	144398,65	2,49	3,06	24,82	16,18
38	16	428641,62	107	2866540,82	2,85	60,68	13,62	3,67
39	2	26254,30	6	78762,90	2,56	1,67	30,33	24,78
40	7	153150,08	7	153150,08	2,38	3,24	90,56	48,47

Grain	Ns	RhoS (cm²)	Ni	RhoI (cm²)	Dpar	U ppm	FT age	1s
41	7	153150,08	38	831386,14	2,35	17,60	16,78	6,92
42	29	380687,34	272	3570584,68	2,65	75,58	9,72	1,92
43	3	65635,75	15	328178,74	2,65	6,95	18,21	11,53
44	3	43757,17	8	116685,77	2,45	2,47	34,11	23,11
45	5	131271,50	9	236288,69	2,47	5,00	50,47	28,18
46	3	39381,45	12	157525,79	3,02	3,33	22,76	14,70
47	1	18753,07	8	150024,57	3,13	3,18	11,39	12,08
48	7	91890,05	23	301924,44	2,68	6,39	27,70	11,98
49	12	225036,85	13	243789,92	3,38	5,16	83,64	33,56
50	5	93765,35	18	337555,27	2,86	7,15	25,28	12,80
51	6	78762,90	29	380687,34	2,90	8,06	18,84	8,47
52	2	32817,87	30	492268,11	3,22	10,42	6,08	4,44
53	4	52508,60	51	669484,63	4,51	14,17	7,15	3,72
54	3	43757,17	12	175028,66	2,39	3,70	22,76	14,70
55	7	91890,05	65	853264,72	3,11	18,06	9,81	3,91
56	5	109392,91	7	153150,08	2,67	3,24	64,81	37,99
57	3	78762,90	21	551340,28	2,63	11,67	13,02	8,04
58	3	82044,68	6	164089,37	2,91	3,47	45,44	32,15
59	8	52508,60	44	288797,29	2,66	6,11	16,56	6,38
60	6	98453,62	34	557903,86	2,55	11,81	16,07	7,13
61	8	210034,39	3	78762,90	2,09	1,67	238,72	161,75
62	5	126222,59	7	176711,63	2,68	3,74	64,81	37,99
63	3	39381,45	12	157525,79	2,59	3,33	22,76	14,70
64	10	72928,61	30	218785,83	3,45	4,63	30,33	11,11
65	4	105017,20	36	945154,77	3,53	20,01	10,13	5,34
66	10	164089,37	57	935309,41	3,06	19,80	15,98	5,50
67	3	56259,21	25	468826,77	2,87	9,92	10,93	6,69
68	2	32817,87	93	1526031,14	2,94	32,30	1,96	1,40
69	3	39381,45	4	52508,60	2,41	1,11	68,04	52,00
70	2	26254,30	22	288797,29	2,82	6,11	8,29	6,12
71	9	118144,35	31	406941,64	2,70	8,61	26,42	10,03
72	3	78762,90	11	288797,29	3,02	6,11	24,82	16,18
73	5	93765,35	21	393814,49	2,60	8,34	21,68	10,80
74	6	87514,33	127	1852386,66	3,04	39,21	4,31	1,80
75	2	32817,87	10	164089,37	2,53	3,47	18,21	14,12
76	2	29171,44	7	102100,05	2,61	2,16	26,00	20,86
77	1	18753,07	4	75012,28	2,56	1,59	22,76	25,45
78	7	153150,08	103	2253494,01	2,74	47,70	6,19	2,43
79	7	91890,05	27	354433,04	3,08	7,50	23,60	10,03
80	10	131271,50	21	275670,14	2,99	5,84	43,28	16,67
81	5	102555,86	20	410223,42	2,28	8,68	22,76	11,40
82	2	29171,44	1	14585,72	2,85	0,31	179,86	220,34

Manaure**ND** 2885**RhoD** 3780065,55**Zeta** 335,7±6,6

Grain	Ns	RhoS (cm^2)	Ni	RhoI (cm^2)	Dpar	U ppm	FT age	1s
1	3	39381,45	85	1115807,71	-	3,39	22,35	13,15
2	4	175028,66	164	7176175,10	-	21,83	15,46	7,83
3	5	109392,91	306	6694846,28	-	20,37	10,36	4,68
4	7	170166,75	403	9796743,11	-	29,81	11,01	4,21
5	2	32817,87	92	1509622,20	-	4,59	13,78	9,86
6	3	164089,37	32	1750286,61	-	5,33	59,21	35,79
7	2	26254,30	100	1312714,96	-	3,99	12,68	9,06
8	4	125020,47	262	8188840,92	-	24,91	9,68	4,88
9	4	72928,61	82	1495036,48	-	4,55	30,88	15,83
10	1	29171,44	111	3238030,23	-	9,85	5,71	5,74
11	4	58342,89	253	3690187,60	-	11,23	10,02	5,06
12	5	82044,68	67	1099398,78	-	3,34	47,18	21,91
13	1	26790,10	35	937653,54	-	2,85	18,10	18,37
14	1	13127,15	73	958281,92	-	2,92	8,69	8,75
15	2	52508,60	170	4463230,85	1,53	13,58	7,46	5,31
16	1	43757,17	141	6169760,30	1,78	18,77	4,50	4,52
17	2	32817,87	81	1329123,89	2,64	4,04	15,65	11,21
18	1	13127,15	128	1680275,15	2,10	5,11	4,96	4,98
19	3	72928,61	184	4472954,67	2,03	13,61	10,34	6,02
20	2	32817,87	45	738402,16	1,13	2,25	28,14	20,35
21	8	131271,50	122	2001890,31	2,55	6,09	41,47	15,18
22	3	39381,45	105	1378350,70	1,96	4,19	18,10	10,61
23	1	24309,54	59	1434262,64	1,57	4,36	10,75	10,84
24	8	350057,32	134	5863460,14	1,25	17,84	37,77	13,78
25	4	131271,50	47	1542440,07	2,31	4,69	53,77	28,05
26	1	21878,58	80	1750286,61	2,07	5,33	7,93	7,98
27	3	72928,61	60	1458572,17	2,30	4,44	31,65	18,74
28	4	52508,60	108	1417732,15	1,92	4,31	23,46	11,96
29	2	32817,87	303	4971907,90	2,23	15,13	4,19	2,97
30	1	13127,15	105	1378350,70	2,33	4,19	6,04	6,07
31	2	29171,44	70	1021000,52	2,30	3,11	18,10	12,99
32	3	157525,79	23	1207697,76	2,33	3,67	82,23	50,53

Results of (U-Th)/He dating

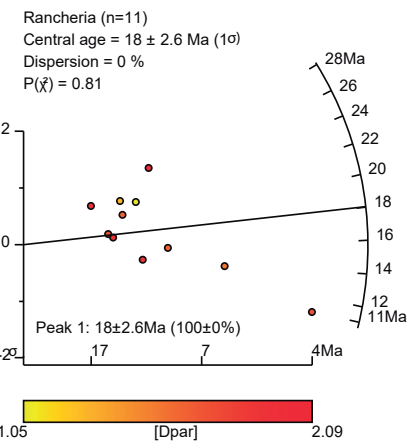
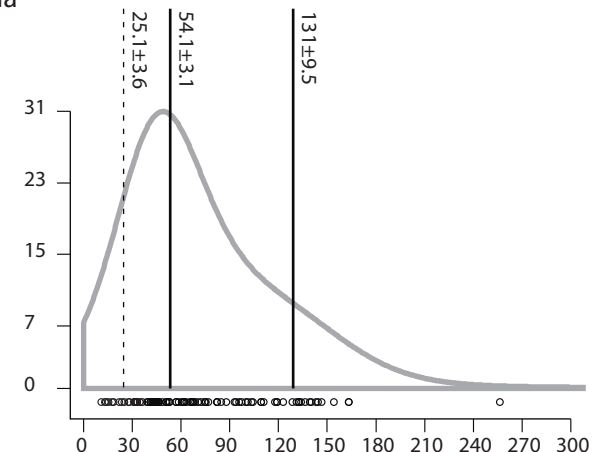
Sample	Mass (ug)	U (ppm)	Th(ppm)	Sm(ppm)	eU(ppm)	He(nmol/g)	ESR	Ft	Raw age (Ma)	Corr.age(Ma)	2s (Ma)
Guatapuri-1	1,56	2,11	8,91	30,46	4,21	0,20	42,1	0,64	8,20	12,73	2,54
Guatapuri-2	3,40	1,81	14,77	63,62	5,28	0,17	54,0	0,72	5,31	7,35	1,13
Guatapuri-3	2,03	3,42	13,49	29,31	6,60	0,40	42,6	0,65	10,74	16,57	1,59
Guatapuri-4	6,67	3,97	6,98	23,46	5,61	0,53	69,3	0,78	16,92	21,59	1,02
Guatapuri-5	2,00	5,62	12,27	8,75	8,51	0,57	45,8	0,67	12,24	18,20	1,66
Guatapuri-6	3,84	9,25	18,84	5,39	13,68	1,11	56,2	0,73	14,92	20,35	0,86
Guatapuri-7	1,65	4,51	5,15	14,80	5,72	0,41	43,6	0,66	12,84	19,56	2,20
Guatapuri 8	1,18	2,02	10,93	12,89	4,59	0,51	37,4	0,60	20,15	33,63	4,46
Guatapuri 9	0,95	10,66	1,65	43,67	11,05	0,66	35,4	0,58	10,70	18,56	2,36
Guatapuri 11	2,06	4,27	2,18	21,48	4,78	0,92	46,6	0,68	34,43	50,76	2,72
Guatapurí 13	1,84	5,72	6,10	12,84	7,15	0,51	45,2	0,67	12,96	19,40	1,66
Guatapurí 14	0,65	1,97	0,93	22,10	2,19	0,15	31,2	0,52	11,56	22,30	18,01
Guatapurí 15	1,11	18,36	0,25	29,20	18,42	1,42	37,3	0,60	14,07	23,56	1,48
Guatapurí 16	2,53	10,52	26,71	57,51	16,80	1,20	46,6	0,68	12,88	18,99	1,03
Guatapurí 17	0,88	17,92	26,34	5,21	24,11	1,78	35,0	0,57	13,65	23,89	1,24
Guatapurí 18	1,11	1,31	1,52	20,32	1,67	0,32	38,0	0,61	31,96	52,80	11,76
Guatapurí 19	1,48	1,21	0,49	24,29	1,33	0,13	40,6	0,63	15,93	25,26	9,02
Guatapurí 20	0,75	7,11	10,52	21,26	9,58	0,25	33,2	0,55	4,81	8,79	3,50
Guatapurí 21	2,87	1,68	2,71	25,47	2,32	0,28	52,1	0,71	20,73	29,11	3,65
Guatapurí 22	0,72	1,07	4,89	36,64	2,22	0,29	30,2	0,50	20,89	41,45	13,41
Guatapurí 23	1,30	5,46	10,00	8,15	7,81	0,54	38,1	0,61	12,77	21,04	2,34
Guatapurí 24	0,80	3,92	2,14	21,60	4,43	1,10	31,3	0,52	44,24	85,05	7,34
Guatapurí 25	1,57	53,33	6,80	50,19	54,93	3,47	43,0	0,65	11,64	17,88	0,65
Guatapurí 26	3,01	15,97	26,17	39,37	22,12	2,13	52,8	0,72	17,50	24,45	0,54
Guatapurí 27	2,17	3,23	8,82	56,51	5,31	0,52	45,3	0,67	16,58	24,77	2,16
Guatapurí 28	2,26	2,32	9,59	21,85	4,57	0,36	46,1	0,67	14,14	20,97	2,15
Guatapurí 29	0,81	1,23	6,05	32,43	2,65	0,27	33,6	0,55	16,92	30,54	8,82
Guatapurí 30	1,57	1,66	2,92	22,81	2,35	0,13	43,0	0,65	9,83	15,11	4,87

Sample	Mass (ug)	U (ppm)	Th(ppm)	Sm(ppm)	eU(ppm)	He(nmol/g)	ESR	Ft	Raw age (Ma)	Corr.age(Ma)	2s (Ma)
Badillo 2	4,37	8,64	24,17	45,19	14,32	1,44	56,8	0,74	18,13	24,63	0,60
Badillo 3	1,39	23,48	31,95	66,71	30,99	2,34	35,5	0,58	13,72	23,76	1,11
Badillo 4	1,90	13,84	13,57	23,89	17,03	1,33	44,7	0,66	14,32	21,57	1,35
Badillo 5	2,77	4,24	12,70	29,08	7,23	0,39	46,3	0,68	9,57	14,16	1,30
Badillo 6	5,97	11,04	32,30	53,70	18,63	1,97	59,8	0,75	19,03	25,40	0,96
Badillo 7	3,53	8,89	17,38	34,30	12,98	0,84	55,2	0,73	11,65	16,00	0,76
Badillo 8	2,53	6,49	20,98	48,94	11,42	0,76	42,1	0,64	11,95	18,56	1,35
Badillo 9	2,60	4,85	18,57	29,11	9,22	0,62	50,7	0,70	12,09	17,17	1,23
Badillo 10	2,40	12,25	27,98	33,08	18,82	1,47	44,3	0,66	14,23	21,53	1,35
Badillo 11	2,77	11,65	26,57	53,57	17,89	1,37	46,3	0,68	13,83	20,46	0,57
Badillo 12	6,95	2,54	11,61	29,85	5,27	0,42	68,8	0,78	14,19	18,15	0,98
Badillo 13	0,69	17,30	28,31	53,28	23,95	2,08	30,9	0,52	15,80	30,66	1,72
Badillo 14	4,99	4,74	17,29	32,39	8,81	0,67	63,0	0,76	13,66	17,93	0,82
Badillo 15	1,98	14,74	35,10	34,81	22,99	1,88	42,9	0,65	14,96	22,99	0,87
Badillo 16	1,34	4,97	14,49	25,81	8,38	0,42	35,4	0,58	9,08	15,77	2,05
Badillo 17	2,93	16,08	19,52	36,25	20,66	1,82	50,0	0,70	16,07	22,95	0,70
Badillo 18	2,64	6,93	24,30	26,55	12,64	1,08	47,6	0,68	15,47	22,59	1,21
Badillo 19	5,02	1,05	4,22	21,15	2,04	0,28	62,6	0,76	22,95	30,18	2,26
Badillo 20	2,02	6,68	12,23	28,73	9,56	0,54	46,5	0,68	10,22	15,09	1,31
Badillo 21	1,48	9,76	26,01	44,60	15,87	1,04	40,6	0,63	11,81	18,73	1,30
Badillo 22	1,84	7,26	18,56	34,34	11,62	3,01	43,8	0,66	46,59	70,85	2,65
Badillo 23	2,25	3,59	13,08	15,81	6,66	0,72	47,9	0,69	19,56	28,47	2,21
Badillo 24	1,45	11,75	35,26	41,58	20,04	1,64	36,9	0,59	14,89	25,09	1,26
Badillo 25	1,44	5,49	20,48	30,64	10,30	0,48	38,0	0,60	8,45	13,97	1,31
Badillo 27	1,01	4,03	13,74	25,05	7,26	0,52	34,9	0,57	12,81	22,49	3,97
Badillo 28	0,86	12,00	24,54	58,34	17,76	5,31	34,3	0,56	53,62	95,33	5,25
Badillo 29	1,22	7,38	23,14	36,58	12,82	1,04	37,2	0,60	14,61	24,51	2,19
Badillo 30	0,92	6,97	19,38	24,77	11,53	0,68	35,6	0,58	10,71	18,51	1,69

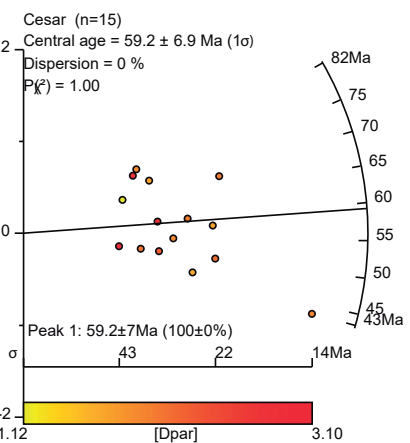
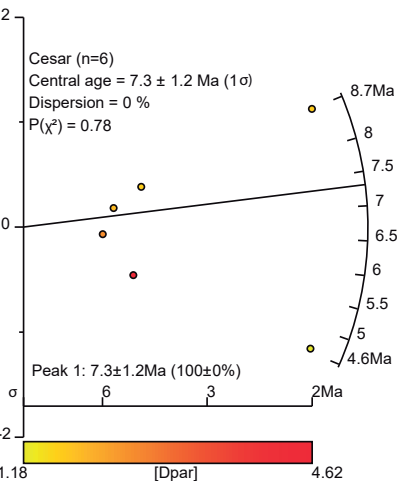
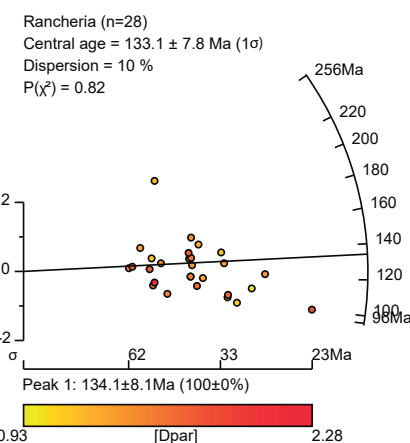
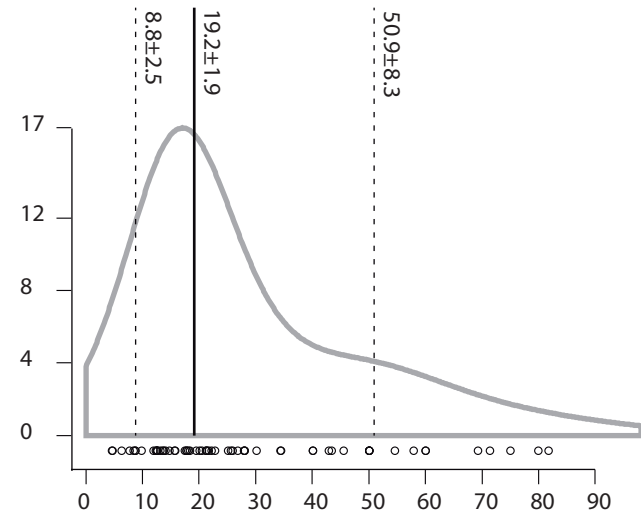
Sample	Mass (ug)	U (ppm)	Th(ppm)	Sm(ppm)	eU(ppm)	He(nmol/g)	ESR	Ft	Raw age (Ma)	Corr.age(Ma)	2s (Ma)
Rancheria 1	2,53	3,91	17,42	31,72	8,00	0,54	44,4	0,66	12,10	18,28	1,59
Rancheria 2	1,98	3,15	13,35	28,82	6,29	0,38	42,0	0,64	10,83	16,86	1,79
Rancheria 3	1,93	3,87	15,60	27,33	7,54	0,51	41,5	0,64	12,03	18,84	1,47
Rancheria 4	0,75	3,69	7,93	3,13	5,55	0,14	31,7	0,53	4,49	8,53	6,43
Rancheria 5	2,82	4,19	14,22	27,04	7,53	0,34	50,7	0,70	8,11	11,51	1,05
Rancheria 6	2,31	3,04	16,27	32,96	6,86	0,52	47,0	0,68	13,45	19,75	1,48
Rancheria 7	1,30	6,31	14,31	30,20	9,68	0,27	37,6	0,60	4,98	8,28	1,84
Rancheria 8	1,73	3,91	15,65	28,38	7,58	0,43	42,2	0,64	10,14	15,74	1,64
Rancheria 9	0,93	4,91	15,48	28,79	8,54	0,31	32,5	0,54	6,46	11,98	3,09
Rancheria 10	2,44	3,74	14,85	26,34	7,23	0,46	47,6	0,69	11,36	16,58	1,20
Rancheria 11	2,56	3,58	14,57	24,33	7,00	0,43	48,6	0,69	10,96	15,85	1,16
Rancheria 12	1,99	1,57	9,06	21,10	3,70	0,43	43,7	0,66	20,40	31,07	3,31
Rancheria 13	1,97	1,52	6,35	16,50	3,01	0,07	39,8	0,62	3,92	6,29	3,25
Rancheria 14	2,67	1,91	6,60	13,62	3,46	0,17	50,3	0,70	8,93	12,73	1,80
Rancheria 15	1,51	3,43	12,77	33,06	6,43	0,34	37,7	0,60	9,44	15,68	2,01
Rancheria 16	0,79	1,87	9,59	19,69	4,13	0,16	31,6	0,53	6,99	13,28	7,21
Rancheria 17	4,08	3,06	12,39	27,50	5,97	0,48	54,4	0,72	14,38	19,86	1,25
Rancheria 18	0,68	3,41	11,31	31,16	6,07	0,27	31,0	0,52	7,95	15,42	5,97
Rancheria 19	2,27	4,91	12,74	18,88	7,91	0,34	46,4	0,68	7,82	11,55	1,23
Rancheria 20	1,41	3,60	16,47	34,61	7,47	0,49	39,4	0,62	11,62	18,76	2,49
Rancheria 21	1,20	3,49	17,29	34,54	7,55	0,45	38,7	0,61	10,66	17,41	3,13
Rancheria 22	2,71	4,67	16,34	30,97	8,51	0,47	46,1	0,67	9,94	14,73	1,10
Rancheria 23	5,21	2,80	12,87	27,75	5,82	0,60	56,4	0,73	18,34	24,98	1,33
Rancheria 26	2,20	3,59	25,55	28,16	9,59	0,61	47,3	0,68	11,41	16,72	1,68
Rancheria 27	1,18	3,95	17,75	31,45	8,12	0,43	34,9	0,57	9,43	16,53	2,62
Rancheria 28	1,56	3,50	17,10	23,67	7,52	0,50	39,3	0,62	11,86	19,19	1,73
Rancheria 29	1,51	2,90	14,18	29,88	6,24	0,35	39,2	0,62	10,08	16,32	2,84
Rancheria 30	4,40	4,67	15,64	22,73	8,34	0,62	57,4	0,74	13,49	18,26	0,66

Appendix II. Validity of age peaks

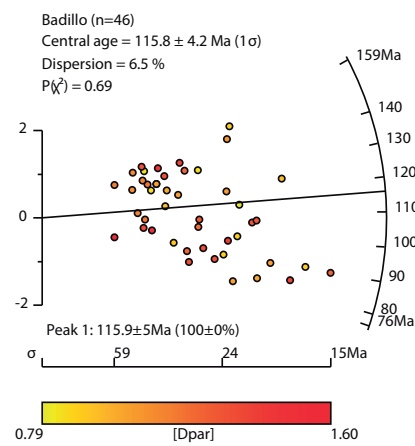
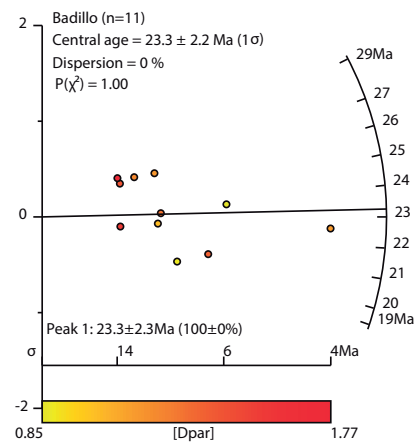
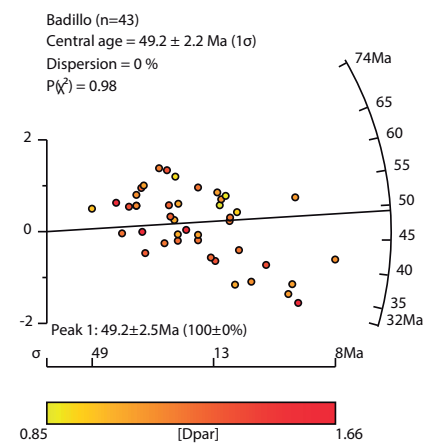
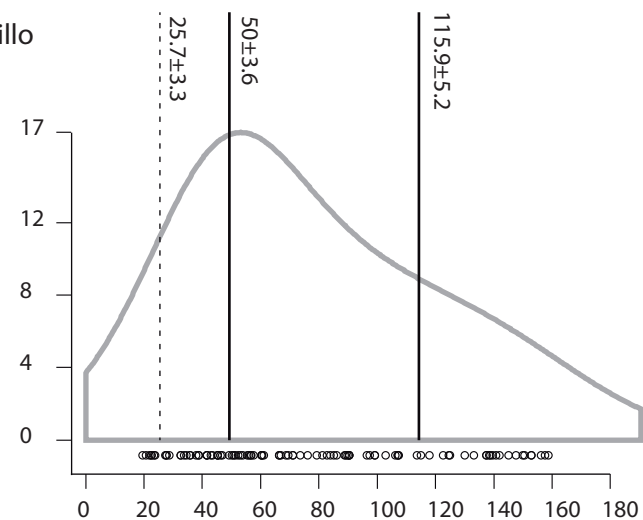
Rancheria



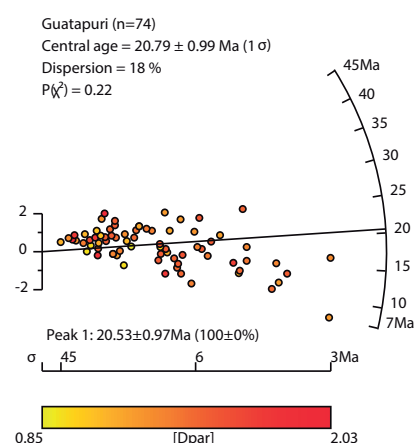
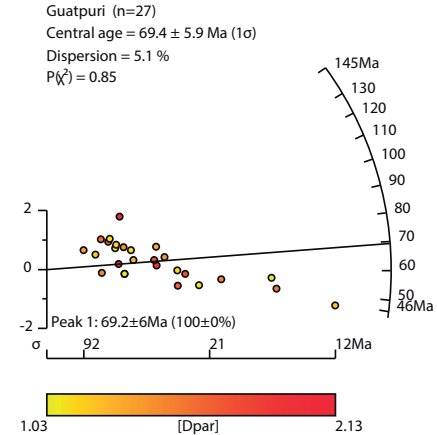
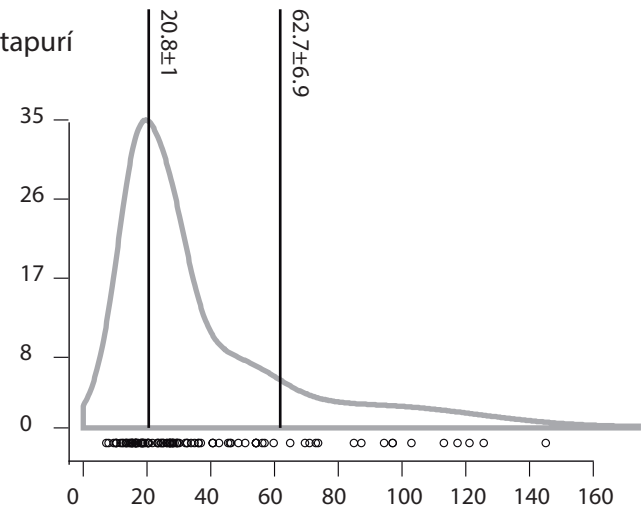
Cesar



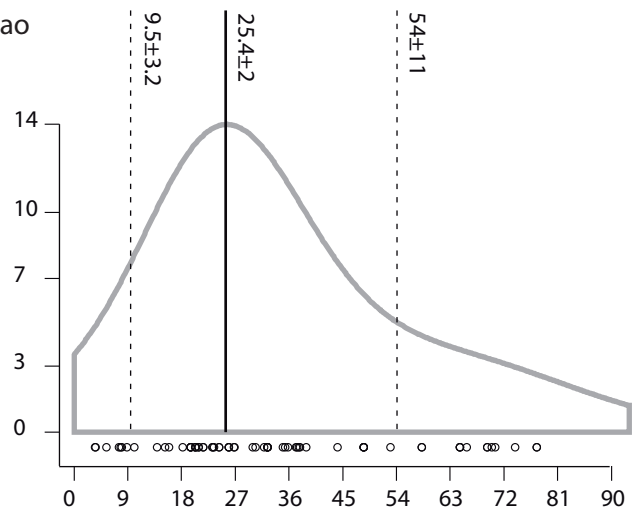
Badillo



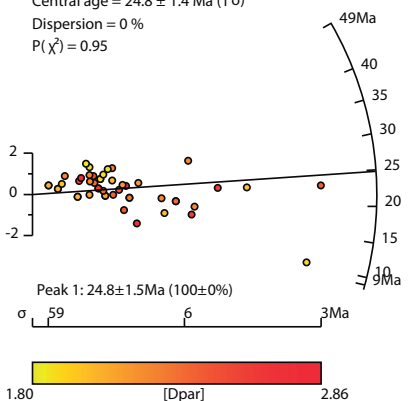
Guatapuri



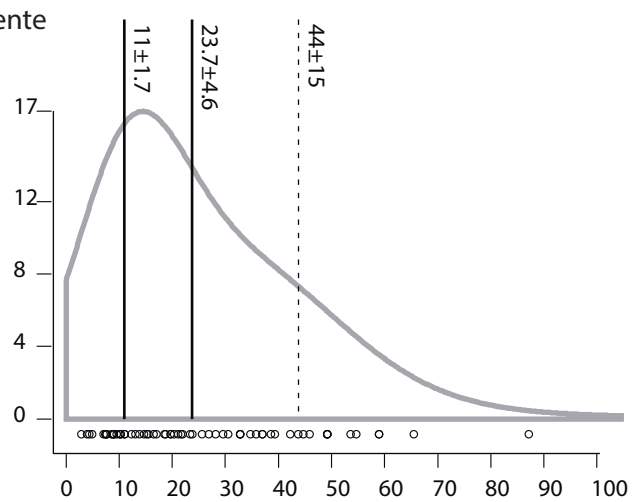
Callao



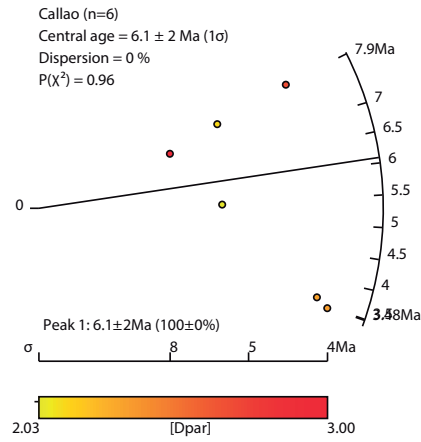
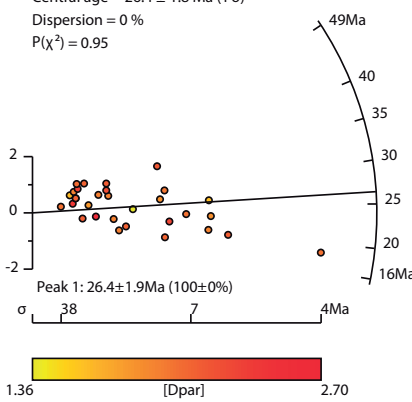
Callao (n=48)
 Central age = 24.8 ± 1.4 Ma (1σ)
 Dispersion = 0 %
 $P(\chi^2) = 0.95$



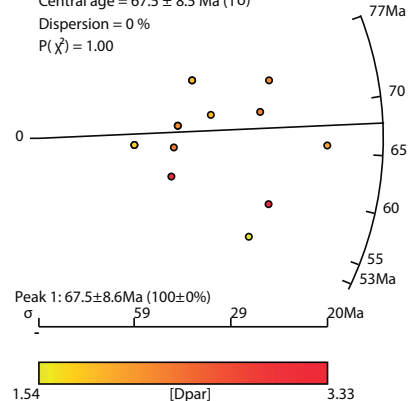
Oriente



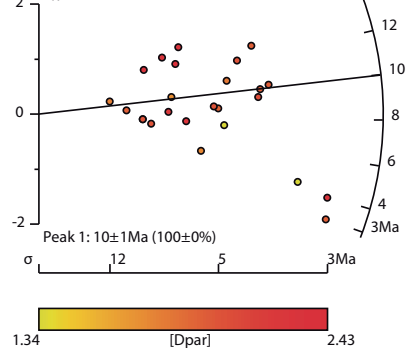
Oriente (n=31)
 Central age = 26.4 ± 1.8 Ma (1σ)
 Dispersion = 0 %
 $P(\chi^2) = 0.95$



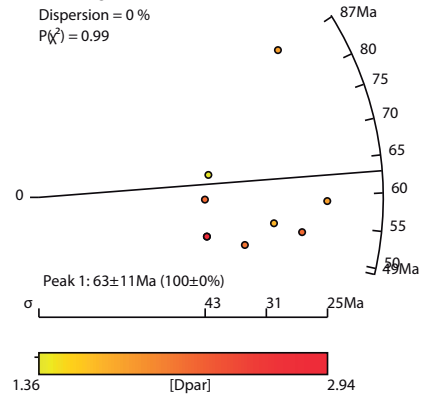
Callao (n=14)
 Central age = 67.5 ± 8.5 Ma (1σ)
 Dispersion = 0 %
 $P(\chi^2) = 1.00$



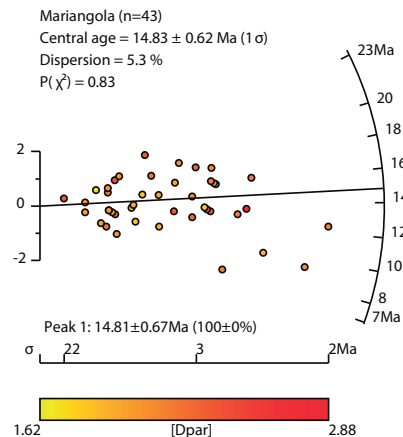
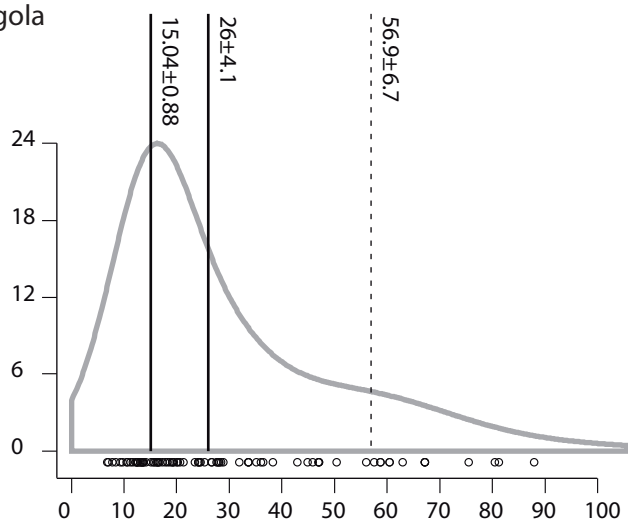
Oriente ($n=25$)
 Central age = 10 ± 1 Ma (1σ)
 Dispersion = 0 %
 $P(\chi^2) = 0.99$



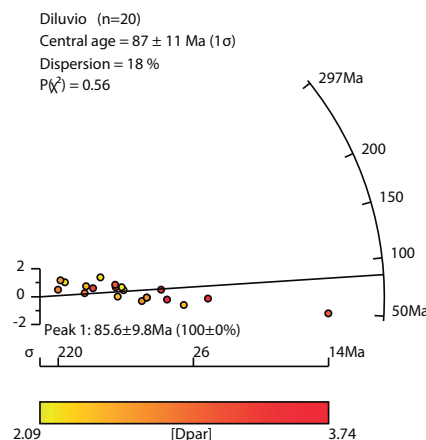
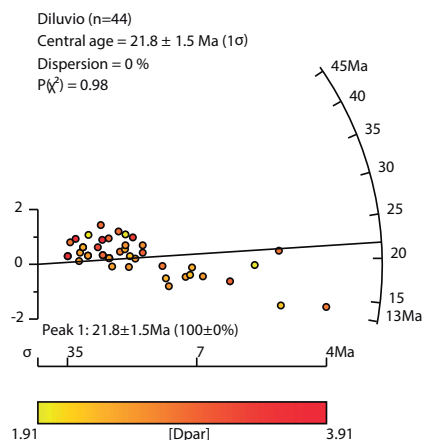
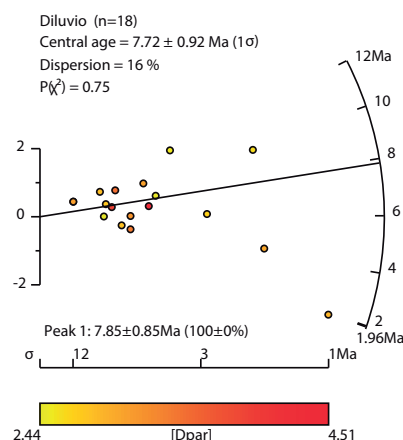
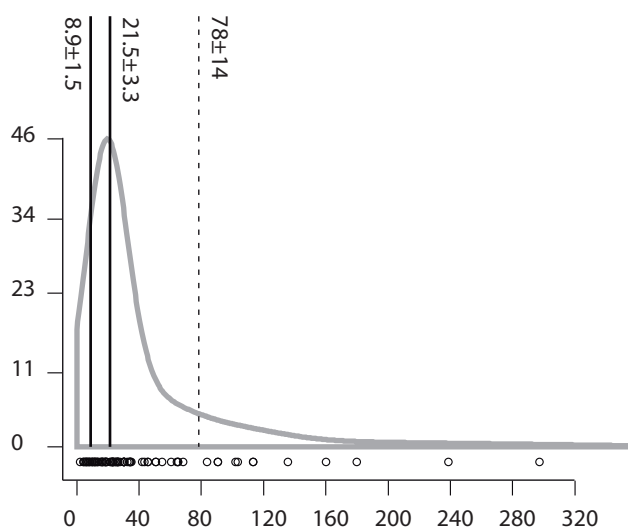
Orienete (n=9)
 Central age = 63 ± 11 Ma (1σ)
 Dispersion = 0 %
 $P(\chi^2) = 0.99$



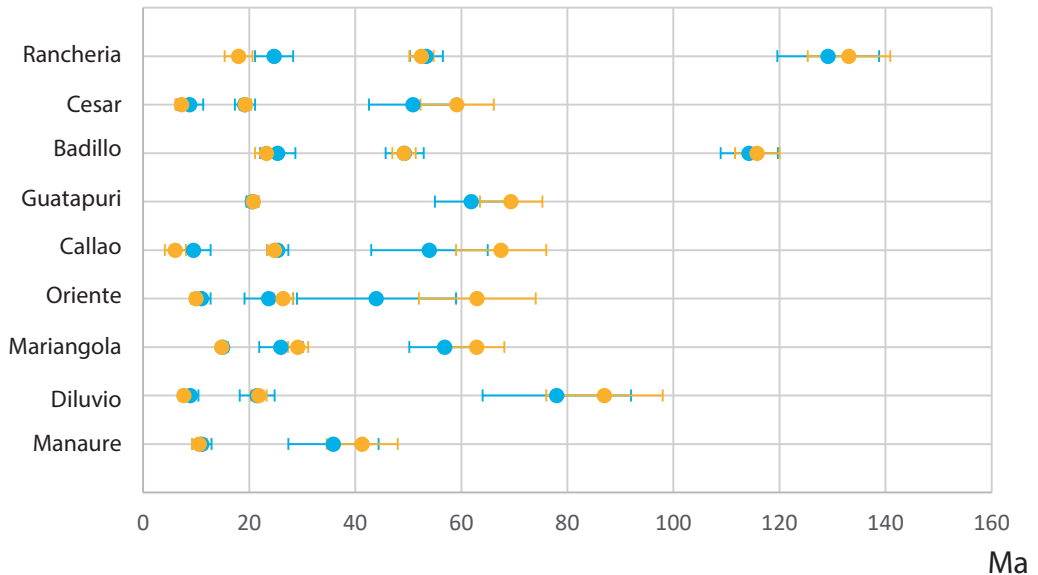
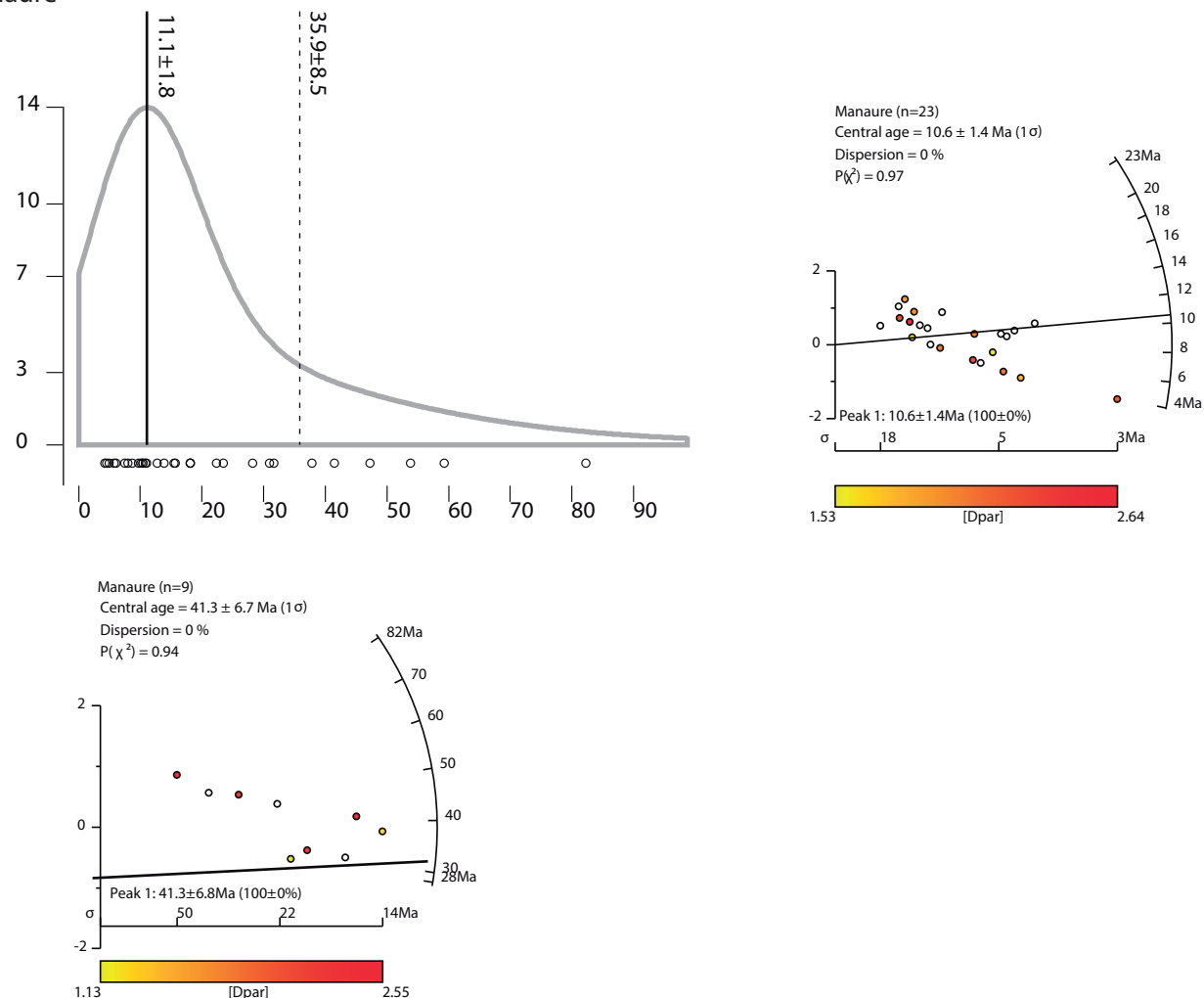
Mariangola



Diluvio



Manaure



- Age peaks found from age distributions show in KDE plots
- Central age from each age peak yield by their respective radial plot.